Generating Brilliant X–ray Pulses from Particle–driven Plasma Wakefields

James Alex Holloway
University College London

Submitted to University College London in fulfilment
of the requirements for the award of the
degree of **Doctor of Philosophy**

January 21th, 2014

Declaration

I, James Alex Holloway, confirm that the work presented in this thesis is my own. Where information has been derived from other sources, I confirm that this has been indicated in the thesis.

James Alex Holloway _____

Abstract

This thesis presents a simulation campaign that demonstrates for the first time, that by micro–bunching the Diamond Light Source electron beam, X-ray pulses with peak brightnesses of $\hat{B} = 3.2 \times 10^{28}$ photons^{-1}s^{-1}mm^{-2}mrad^{-2}0.1%BW^{-1} at $E = 50$ keV are produced. The production mechanism ensures the pulses are radially polarized on creation. These properties allow for a smaller focal spot, overcoming the limit due to diffraction, providing a unique new probe for individual atomic excitations by the utilisation of the longitudinal component of the electric field. We also demonstrate that the micro–bunched electron beam is an effective wakefield driver in itself, able to accelerate a witness electron beam to higher energies, providing a potential new route to reliable X–ray free electron laser generation.

An experiment was performed using the $E = 600$ mJ, $\tau = 40$ fs Astra laser at the Central Laser Facility testing a novel single–shot parasitic plasma diagnostic. The photon acceleration effect on the driving laser pulse was utilised to determine the plasma density. Strong modulation to the long laser pulse's intensity profile were measured at the plasma wavelength, capturing the self–modulation effect on the long laser pulse. The results show a linear relationship between the diagnosed plasma density and the known pressure within the gas target and are supported by numerical simulations. The diagnostic requires no dedicated probe pulse but instead simply requires the driving laser pulse to be several plasma periods long, allowing for a cost effective, simple to implement diagnostic.

Acknowledgements

For my parents, Julie and Aidan,
you were there every step of the way.

To my supervisors, Matthew Wing and Peter Norreys,
for your guidance, council and friendship.

Because my friends, Rebecca Falla and Rebecca Chislett,
I'd be somewhere else without you.

Contents

List of Figures

List of Tables

Chapter 1.

Introduction

1.1. Particle Acceleration

1.1.1. Conventional Acceleration

Since the 1930s, particle accelerators have been used to further understand the fundamentals of particle physics. Colliders at the energy frontier are able to explore the predictions of the standard model, and by proving or disproving them they advance the field of particle physics. New discoveries come as particle accelerators are able to reach higher energy regimes, but as the energies increase so does the size and cost of the accelerators.

Constructing and running modern high energy particle accelerators is an expensive and demanding task. Large laboratories such as CERN, SLAC, DESY and FNAL have particle accelerators many kilometres long. These machines consist of metal cavities wherein particles are accelerated using an alternating electric field. Electric field gradients greater than $E = 100$ MV^{-1} ionise the metal itself, destroying the accelerator, so to reach higher particle energies one has to increase the length over which the particles are accelerated. The Livingston plot, figure 1.1, summarises the centre–of–mass energy of colliders over the past 50 years. Until recently the centre–of–mass energies increased by about an order of magnitude every ten years. The slowing down of this rate is attributed in part to the saturation of conventional radio frequency accelerator technology. The LHC is already the largest machine in

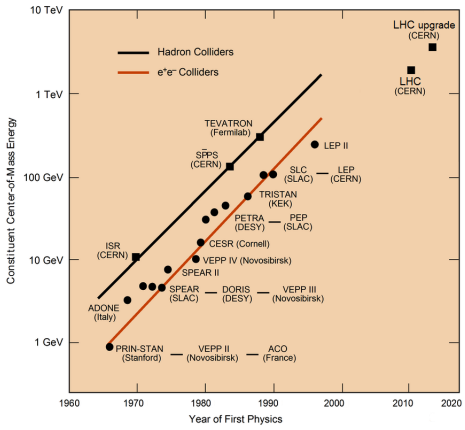

Figure 1.1.: The Livingston plot [3] shows the centre–of–mass energy for both lepton and hadron colliers as a function of time. The Next Linear Collider (NLC) is a proposed lepton collider and as of 2015 there is no such project under construction. Note the hadron colliders show the centre–of–mass energy for the individual partons.

the world, with a circumference of 27 km, and with a budget of £6.19 Billion as of 2010 [2] it is one of the most expensive scientific instruments ever built.

The consensus in the high energy physics community is that the discovery of the Higgs boson by the LHC will have to be complemented by a collider that can study the properties of the Higgs in greater detail. The most likely candidates are the Compact Linear Collider (CLIC) and the International Linear Collider (ILC), both of which plan to collide electron and positron beams generated within linear accelerators that are tens of kilometres long. To keep ever increasing the length of accelerators is not economically viable. Plasmas offer a solution to this problem as they can support far greater electric fields achieving the same energy gains over much shorter distances and, being already ionised, are resistant to further destruction.

1.1.2. Acceleration within a Plasma

A plasma can be defined as a quasi neutral gas of charged and neutral particles which exhibit collective behaviour [4]. A key quantity that characterises a plasma is the plasma frequency. Consider displacing a sheet of electrons in a cold plasma. An electric field between the sheet and the background ions is produced and acts as a restoring force. The sheet of electrons accelerate back towards the region of

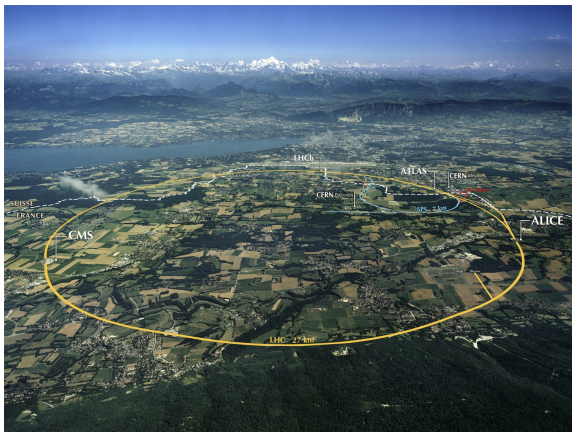

Figure 1.2.: Arial view highlighting the underground Large Hadron Collider (LHC), at CERN, near Geneva. This is the highest energy collider in the world, reaching the TeV regime. Image © CERN.

unmoved ions, gaining kinetic energy. Having reached their original equilibrium position, they overshoot, due to the kinetic energy gained from the electric field, and an oscillation is set up. This is called a Langmuir oscillation [4] and the frequency of this oscillation is the electron plasma frequency.

Now consider a short relativistic electron beam impacting on a plasma, as in figure 1.3. The beam enters the plasma, repelling the plasma electrons away from the axis of beam propagation, leaving the heavier ions behind. The electrons then experience the restoring force of the ion region, which first slows their expulsion and then attracts them back to their equilibrium positions. As they move back on axis they gain kinetic energy and overshoot their equilibrium positions, setting up an oscillation about the axis of beam propagation. The plasma electrons' trajectory traces a figure of eight in the average co–moving frame of the electrons. Alternating regions of high ion density and high electron density trail the driving beam, providing regions of strong accelerating and focusing electrics fields. It is this structure that is called the wakefield, and is used to accelerate charged particles.

It is the electric field resulting from charge separation within a plasma that is used to accelerate particles in plasma wakefield acceleration (PWA). The maximum sustainable electric field in a cold, one dimensional plasma, is given by the relativistic wave breaking limit:

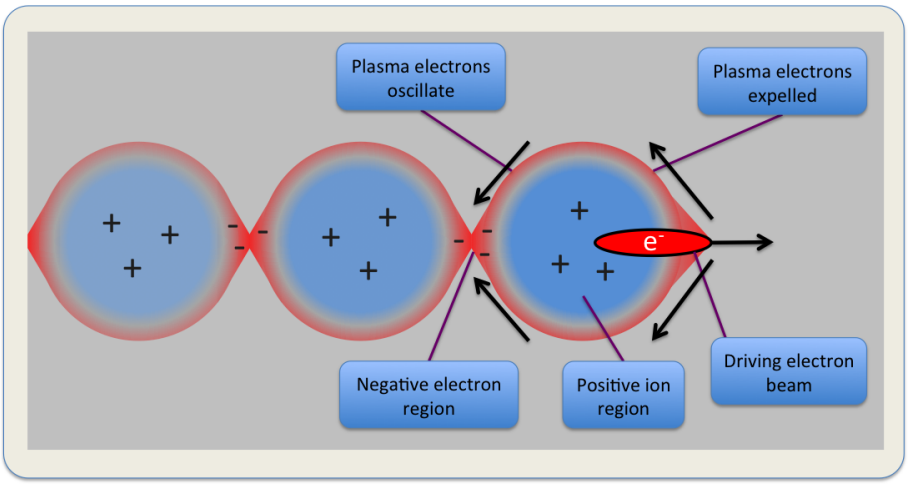

Figure 1.3.: A graphic of a short relativistic electron beam driving a plasma wakefield. The perturbed plasma electrons form a wakefield that co-propagates with the driving beam. An electron between an electron region and ion region will experience a strong longitudinal electric field.

$$E_{zmax} = \frac{\omega_p m_e c}{e} \tag{1.1}$$

where ω_p is the plasma frequency and m_e, c and e have their usual meanings. Beyond this maximum electric field, the oscillating electrons escape the restoring force of the ions and become a collection of fast travelling electrons. This is known as wave breaking and, under the right conditions, can be harnessed to inject electrons into the wakefield. Note this limit is proportional to the square root of the plasma density. Plasmas in the density region of $n_e = 10^{25}$ m^{-3} are common to plasma wakefield experiments and there are many examples of experiments achieving electric fields of $E_{max} > 100$ GVm^{-1} [5–16], which is one thousand times greater than the maximum fields found in conventional accelerators. A plasma wakefield accelerator is a device whereby a high amplitude wakefield is driven by either a relativistic beam of charged particles or an intense laser pulse to accelerate a witness beam to high energies.

The hard limit of electric fields achievable in PWA is reached when collisional effects within the plasma dominate. For a thermally ionised[1] hydrogen plasma ($T = 1$

[1]The number of electrons populating a Debye sphere is proportional to $T_e^{1/2}$. A hotter plasma can therefore have sufficient electrons populating a Debye sphere such that binary collisions do not dominate.

eV) collisional effects become significant at a plasma density of 1.9×10^{24} m^{-3} when the number of electrons populating a Debye sphere approaches unity, as discussed in section 2.1.1. Such a plasma could support a maximum electric field of $E_z \approx 100$ GVm^{-1} before succumbing to wave breaking.

Any electrons injected into the rear of this structure will be accelerated by the longitudinal electric field. Both relativistic beams of charged particles [17] and intense laser pulses [8,18] have successfully been used to accelerate electron witness beams to high energies of $E = 84$ GeV [10] and $E = 1$ GeV [9,19] respectively, which is below the $E \approx 100$ GeV relevant to high energy physics. Staging wakefield accelerators, however, could reach higher energies at the expense of beam luminosity [5]. It is crucial for the phase velocity of the driving beam to be close to the speed of light, c, so that the accelerated electrons do not immediately outrun the driving beam and escape the accelerating structure.

1.2. Radiation Generation

Electron accelerators are no longer just used for fundamental research. The short, brilliant, X–ray pulses emitted by electron accelerators are useful in a wide range of applications; including medical imaging [20], molecular crystallography [21], radiotherapy [22], X–ray biomicroscopy [23] and EUV lithography [24]. Initially, X–rays were obtained parasitically from accelerators by adding windows to the beam line, where samples were imaged. These machines were known as the first generation light sources. The first purpose–built light source was the Synchrotron Radiation Source at Daresbury in 1981 and was classified as a second generation light source. Today facilities such as the Diamond Light Source and the Linac Coherent Light Source (LCLS) improve significantly upon key qualities of the X–ray pulse, such as pulse length, wavelength and number of photons with brilliance increased by many orders of magnitude. To continue to improve the quality of these X–ray pulses, and the medical, industrial and technological impact they have, new facilities and techniques are needed.

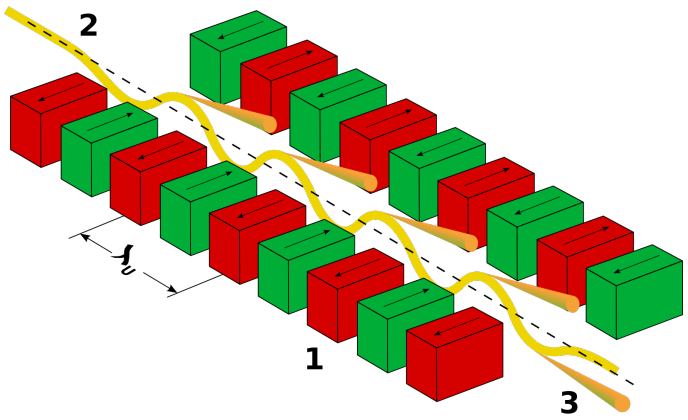

Figure 1.4.: A graphic of an undulator [25]. Alternating polarity dipole magnets (1) cause a propagating beam (2) to undulate, radiating bright, coherent synchrotron radiation (3).

1.2.1. Third Generation Light Sources

Electrons emit synchrotron radiation when following a curved trajectory, i.e. pass through a bending magnet. Third generation light sources maximise this by passing electron beams through insertion devices known as undulators and wigglers. These devices are composed of a series of adjacent alternating bending magnets. The electrons follow a sinusoidal path, emitting radiation at each turn. In the case of an undulator, the radiation coherently adds resulting in an intense coherent X–ray pulse as seen in figure 1.4.

Third generation light sources produce a low emittance electron bunch typically within a synchrotron. Due to the nature of synchrotrons however, the horizontal emittance is hundreds of times larger than the vertical emittance [26]. This is undesirable as the brilliance of an X–ray pulse, a key quantity, diminishes with increased emittance. The advantage of this scheme however, is that a beam can pass through a synchrotron many times, achieving a higher energy before passing through the insertion device. This yields higher energy X–rays as the radiated photons have energy proportional to the square of the emitting electron's energy.

Undulators and wigglers have defining characteristics that allow for the tuning of the spectral range of the emitted radiation. The magnetic period, λ_μ, and the electron's Lorentz factor, $\gamma_e = E/m_e c^2$ (where E is the electron energy and m_e is the

effective mass[2] of the electron), determine the photon energy, E_β, of the radiation produced in the undulator to be,

$$E_\beta = \frac{2\hbar c \gamma_e^2}{\lambda_\mu}, \tag{1.2}$$

where $\hbar$ and c have their usual meaning. To image the atomic scale, photons of wavelength $\simeq 10^{-10}$ m are needed. The Diamond Light Source's Cryogenic Hybrid undulator [29] having an undulator period of $\lambda_\mu = 0.017$ m with an electron gamma factor of $\gamma_e = 5871$ gives a central wavelength of $\lambda = 16.5 \times 10^{-10}$ m, allowing the production of soft X–rays to probe the upper end of the atomic scale.

1.2.2. Fourth Generation Light Sources

To be qualified as a fourth generation light source, an important parameter such as brilliance, coherence or pulse duration is typically improved upon by an order of magnitude or more. The European XFEL and the LCLS fourth generation light sources accelerate electron beams with linear accelerators, so must accelerate the beam to the required energy in a single pass through the machine. As such these accelerators are long, 3.6 km and 3.2 km respectively. Linear accelerators however, are able to achieve pulse lengths far shorter than synchrotrons at higher energies. The European XFEL for example has a pulse length of $\sigma_t \leq 100$ fs [30], compared to the Diamond Light Source pulse length of $\sigma_t = 87$ ps . This, combined with harnessing the micro–bunching effect of undulators on short electron beams, leads to over eight orders of magnitude enhancement to the brilliance of the X–ray pulses when compared to third generation light sources.

Both third and fourth generation light sources are expensive. With the Diamond Light Source costing £260 million to construct with an extra £120 million [31] being invested to provide additional beam lines, any reduction in cost would have a significant impact on future facilities. This thesis demonstrates how plasma wakefield acceleration can drastically boost the qualities of X–rays produced at such facilities

[2]The effective electron mass is the mass it has when responding to a force. The effective mass can differ from m_e due to self-inductance in thin wires [27] for example. The effective mass in semi-conductors has been measured to depend on the number of charge carriers [28].

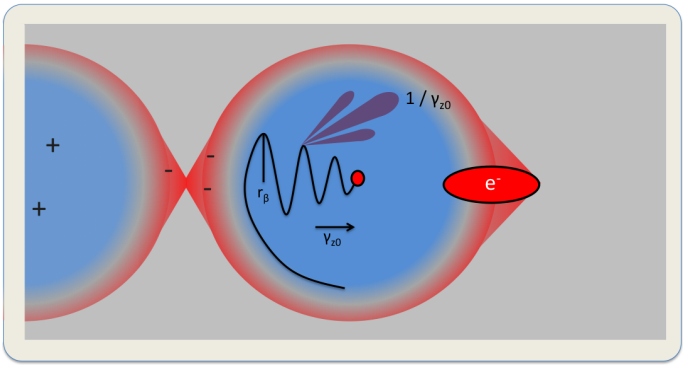

Figure 1.5.: A graphic of a self injected electron's trajectory within a wake (black line) and the resulting cones of radiation emission (purple cone). Here, r_β is the amplitude of the betatron oscillation, γ_{z_0} is the electron's gamma factor in the forward direction and $1/\gamma_{z_0}$ denotes the angle of emission of the radiation.

for a relatively small sum, potentially allowing next generation X–ray pulses to be produced at existing facilities.

1.2.3. Radiation Generation Within a Plasma

An electron beam in the correct phase of a high amplitude wakefield experiences tremendous focusing electric fields ($E_r < 100$ GVm^{-1}) [6]. These fields provoke undulations of an electron beam in a similar way that an undulator or a wiggler would [32], as seen in figure 1.5. The electrons undergo violent undulations generating short, brilliant, X–ray pulses.

Laser-driven wakefields have been used to induce undulations in a witness electron beam generating short, brilliant, linearly coherent X–ray pulses [7, 33, 33–38]. These have been used to image fine structures via phase contrast imaging [7], as seen in figure 1.6. These X–ray pulses, achieving peak brightnesses of 1×10^{22} photons s^{-1} mrad^{-2} mm^{-2} 0.1% BW^{-1} [33], are comparable to third generation light sources whilst being produced over mere centimetres of plasma. If the length over which these beams undulate within the wakefield could be maintained for metres or longer then the brightness would increase by many orders of magnitude.

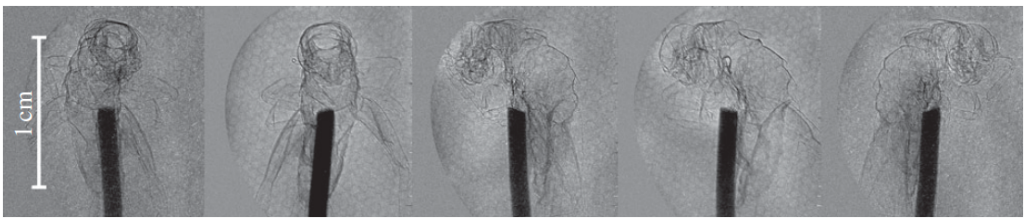

Figure 1.6.: Phase contrast image of a cricket taken with the Astra Gemini betatron source. Images show minimal absorption, indicative of high flux of photons at energies greater than 20 keV, for which the phase-shift cross section greatly exceeds that of absorption by more than 100 times [7].

1.3. Thesis Outline

The work presented in this thesis focuses on numerical simulations of beam–plasma interactions using existing conventional beams and combines experimental results with simulations to investigate ultra-high intensity laser–plasma interactions.

Chapter two contains an overview of relevant theoretical background whilst chapter three details the simulation codes used and contains technical parameter scans and benchmarks ensuring the main codes do not produce spurious results.

Chapter four presents the Diamond beam simulation campaign where the $E = 3$ GeV $Q = 2$ nC electron beam's suitability as a wakefield driver is investigated. The investigation leads to a novel beam line design that achieves longitudinal micro-bunching of the Diamond beam at the micro–bunch length and spacing required to drive a high amplitude wakefield and efficiently couple energy from the beam to the plasma.

Chapter five investigates the Diamond beam's utility as a bright X–ray light source by simulating the treated Diamond beam's micro-bunches oscillating within a wakefield. The strong electric fields within a wakefield are found to trigger copious X–ray emission comparable to current fourth generation light sources.

Chapter six details the experimental set up of the Astra experiment in Target Area 2 while chapter seven presents the results of the photon acceleration single-shot plasma diagnostic on the Astra Target Area 2 experiment.

Chapter eight states the main conclusions of the thesis and outlines avenues of future research.

Chapter 2.

Theory and Techniques

In this chapter, the physics of laser–plasma interactions, particle beam–plasma interactions, photon acceleration and betatron radiation within a plasma will be outlined. The modulation effects of wakefields on particle beams and the radiation emitted from these accelerating particles will be examined.

2.1. Plasma Properties

This section defines plasma parameters relevant to plasma wakefield acceleration that characterise a plasma.

2.1.1. Debye Length

A key quantity for a plasma is the Debye length. The Debye length, λ_D, expresses the distance over which electrostatic fields persist through a plasma. In the presence of an electrostatic field plasma electrons move, acting to shield external charge from the electrostatic potential. It is stated here for simplicity and derived in appendix A.1.1.

$$\lambda_D = \left(\frac{\epsilon_0 k_B T_e}{n_0 e^2} \right)^{1/2}. \tag{2.1}$$

Here k_B is the Boltzmann constant, ϵ_0 is the permittivity of free space, e is the charge of the electron, n_0 is the plasma number density and T_e is the plasma electron temperature. The Debye sphere is then trivially the sphere with the Debye length as the sphere's radius:

$$\Lambda_D = \frac{4\pi}{3}\left(\frac{\epsilon_0 k_B T_e}{n_0 e^2}\right)^{3/2}. \tag{2.2}$$

The Debye number is the average number of electrons populating a Debye sphere and is given by,

$$N_D = \Lambda_D n_0. \tag{2.3}$$

When the Debye number exceeds unity, each particle affects many nearby particles and collective electrostatic interactions dominate over binary collisions and the ideal plasma approximation holds.

2.1.2. Plasma Frequency

A plasma is defined as a quasi neutral gas of charged and neutral particles which exhibit collective behaviour [39]. At equilibrium, an unperturbed plasma has equal numbers of electrons and ions in any region. Consider displacing all the electrons some small amount, δx, from their equilibrium positions whilst keeping the ions fixed as in figure 2.1. Displacing the electrons to the right leaves an excess of positive charge on the left and negative charge on the right of the plasma slab. This produces an electric field acting to move the displaced electrons back to their equilibrium position. However, as they do they gain kinetic energy and overshoot their starting position, resulting in simple harmonic motion about the equilibrium position. The frequency of this oscillation is the plasma frequency, ω_p. By calculating the force acting on each electron and using this with Newton's second law the plasma frequency can be calculated. The slab of ions on the left side and the slab of electrons on the right can be thought of as two parallel charged planes, with cross sectional area, A,

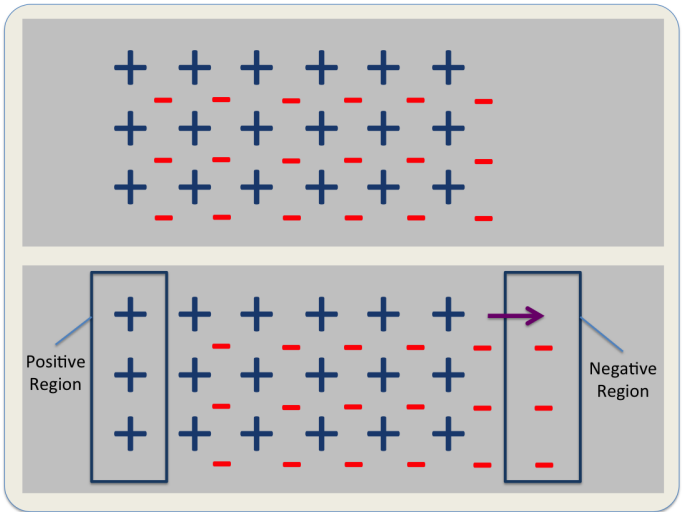

Figure 2.1.: A cold homogeneous plasma (top pane) and a displaced electron slab in a cold plasma (bottom pane). The displaced slab of electrons results in an electric field that acts to restore the slab to its equilibrium position.

and width, x. Using Gauss's law, the electric field between two such planes is given by

$$E = \frac{Q}{\epsilon_0 A}, \tag{2.4}$$

where Q is the total charge of the slab. Writing this in terms of charge density, ρ, and the volume of the plane, V, it is found that $Q = \rho V = en_e Ax$. Equation 2.4 then becomes

$$E = \frac{en_e x}{\epsilon_0}. \tag{2.5}$$

The force experienced by an electron is $F = -eE = -e\frac{en_e x}{\epsilon_0}$. Using this as the force term in Newton's second law,

$$m_e \frac{d^2x}{dt^2} = -\frac{e^2 n_e}{\epsilon_0} x, \tag{2.6}$$

where m_e is the electron mass. Putting equation 2.6 in the standard form of a simple harmonic oscillator,

$$\frac{d^2x}{dt^2} + \frac{e^2 n_e}{\epsilon_0 m_e} x = 0. \tag{2.7}$$

The equation for a simple harmonic oscillator is of the form $\ddot{x} + \omega^2 x = 0$, where ω is the angular frequency of oscillation. Then, the frequency of electron plasma oscillations is:

$$\omega_p = \left(\frac{n_e e^2}{m_e \epsilon_0} \right)^{1/2}. \tag{2.8}$$

This relation holds for small perturbations in the electron number density ($\delta n_e / n_e \ll 1$) and for non-relativistic electron motion ($\gamma_e - 1 < 1$). The ions' inertias are too large to respond to the short period of the oscillation and are considered static. For high amplitude waves in the two–dimensional case, n_e's local variation becomes large enough to become significant and the problem becomes non-linear and analytically insoluble. Typically, laser-driven schemes operate in this non-linear regime, however in the laser/particle-driven hybrid simulations presented here, the amplitude of the wakefield is small ($\delta n_e / n_e \ll 1$) and is considered to be in the linear regime.

2.2. Wakefield Acceleration

Wakefields are driven by relativistic beams that provide a 'kick' to the plasma electrons. This can be from the ponderomotive force of an intense laser pulse, or the space-charge force of charged particles beams. Equation 2.9 expresses the electron plasma number density perturbation of an initially uniform plasma as a driven harmonic oscillation [40] with the drive term of both an electron beam (n_b term) and a laser pulse (a^2 term) included,

$$\left(\frac{\partial^2}{\partial^2 t} + \omega_p^2 \right) \frac{\Delta n_e}{n_0} = -\omega_p^2 \frac{n_b}{n_0} + c^2 \nabla^2 \frac{a^2}{2}, \tag{2.9}$$

where n_0 is the average non-perturbed electron plasma density, Δn_e is the electron plasma density perturbation ($\Delta n_e = n_e - n_0$), ω_p is the plasma frequency (equation 2.8), n_b is the beam density and $a = e|\mathbf{A}|/mc^2$ is the normalised vector potential of the laser.

Laser pulses and electron beams kick the plasma electrons off–axis whilst proton beams pull them onto the axis. The resulting wakefields in the linear regime are essentially the same except they are π out of phase. This section discusses the requirements of such beams to drive an effective wakefield, and contrasts their various advantages and limitations.

2.2.1. Driving a Wakefield

The total energy gain of a witness electron beam experiencing the accelerating phase of a wakefield is trivially the product of the electric field and the distance over which that field is experienced. Maximising both these values is critical to producing high energy electron beams. Efficiently coupling the energy of a drive beam to the plasma is necessary to drive a high amplitude wakefield. This puts strict requirements on the length of the drive beam. Laser drivers tend to be short and are able to efficiently drive wakefields. However, their total energy is orders of magnitude lower than that of the longer electron beams, which in turn are lower still than that of proton beams. In the hybrid simulations presented, the advantages of both particle and laser driven schemes are utilised to maximise the energy coupled to the plasma and ultimately to the witness electron beam.

2.2.2. Dephasing Length

The dephasing length is the length over which a witness electron will remain in the accelerating phase of the wakefield, before outrunning it and encountering the decelerating phase. Trapped electrons remain in the accelerating phase of the wakefield for an extended time because both the electron's velocity and the phase velocity of the wakefield are close to c. Laser driven wakefields tend to have a lower phase velocity than those of particle–beam driven wakefields due to the reduced group velocity of light in a medium, beam head erosion and beam head defocusing effects. The point at which the decelerating region is encountered is the point at

which the witness electron has achieved its maximum energy. As such we define the dephasing time to be the time taken for an electron to travel $\lambda_p/2$ in the wakefield frame, $\xi = x - ct$, and the dephasing length to be the dephasing time multiplied by c. We assume the phase velocity of the wakefield to be the group velocity of the laser pulse and the velocity of the electron to be c.

$$v_e \approx c \qquad (2.10) \qquad\qquad v_{ph} = v_g \qquad (2.11)$$

For $\omega_p^2/\omega_0^2 \ll 1$ we approximate,

$$v_{ph} = c\sqrt{1 - \frac{\omega_p^2}{\omega_0^2}} \approx c\left(1 - \frac{\omega_p^2}{2\omega_0^2}\right), \qquad (2.12)$$

where ω_0 is the frequency of the laser. The difference between the wakefield and electron beam's velocity is then,

$$\delta v = v_e - v_{ph} = c - c\left(1 - \frac{\omega_p^2}{2\omega_0^2}\right) = c\frac{\omega_p^2}{2\omega_0^2}. \qquad (2.13)$$

Given that the accelerating phase spans half of the plasma wavelength, $L_{acc} = \lambda_p/2 = \pi c/\omega_p$, then the time taken for an electron to dephase is,

$$\tau_{dephase} = \frac{L_{acc}}{\delta v} = \frac{2\pi\omega_0^2}{\omega_p^3}. \qquad (2.14)$$

The dephasing length, then, is simply $L_D = c\tau_{dephase}$,

$$L_D = c\frac{L_{acc}}{\delta v} = \frac{2\pi c\omega_0^2}{\omega_p^3} = \lambda_p\frac{\omega_0^2}{\omega_p^2}. \qquad (2.15)$$

Using $\gamma = 1/\sqrt{1 - v_{ph}^2/c^2}$ with equation 2.12 it can be shown that,

$$\gamma_{wake} = \frac{\omega_0}{\omega_p}. \tag{2.16}$$

This gives a simple expression for the dephasing length,

$$L_D = \lambda_p \gamma_{wake}^2. \tag{2.17}$$

For a plasma density of $n_e = 1 \times 10^{25}$ m^{-3} and a laser of wavelength $\lambda_0 = 1.064$ µm, parameters common to experiments [7], the dephasing length is $L_D = 1$ mm. A plasma of such a density supports a maximum electric field of $E_{zmax} = 96$ GVm^{-1}, given by equation 1.1. The maximum energy gain of a witness beam is then trivially $W_{max} = E_{zmax} \times L_D = 96$ MeV.

Dephasing occurs in particle–driven plasma wakefield acceleration over larger lengths, due to the higher γ factor of the driving beam. Equation 2.18 gives the dephasing length for the particle–driven case under the same assumptions as the laser dephasing length derivation,

$$L_{Dpwa} = \frac{\lambda_p}{2(\beta_e - \beta_{drive})}, \tag{2.18}$$

where β_e is the velocity of the witness electron beam divided by c and β_{drive} is the velocity of the drive beam divided by c.

Using the 3 GeV electron Diamond beam as an example and the same plasma density as the laser driven example above and assuming $\beta_e \gg \beta_{drive}$, the dephasing length is $L_D = 1330$ m. This is a full six orders of magnitude higher than the laser driven case. Later the Diamond beam is shown to be able to drive a wakefield of the order $E_z = 1$ GVm^{-1} in numerical simulations, when manipulated correctly. This gives a theoretical maximum energy gain of the order of a TeV, given other limiting factors, such as depletion length, are mitigated.

One solution to dephasing between the driver and the witness beam is to taper the plasma density longitudinally [41]. Increasing the plasma density reduces the

length of the wakefield ($n_e \propto \lambda_p^{-2}$). The front of the wakefield remains with the driving beams head, whilst the rear accelerating region sweeps forward with the faster travelling electron beam. If chosen correctly, a tapered longitudinal plasma density profile can maintain the phase experienced by the witness beam throughout a plasma stage.

2.2.3. Depletion Length

A beam driving a wakefield will eventually lose all its energy to the plasma, the length over which this occurs is said to be the depletion length. Acceleration of the witness beam cannot occur past this point. By equating the energy stored in the electric field of a wakefield of length L_w with the energy of the drive beam, E_d, the depletion length can be calculated.

$$E_d = E_L^2 c\tau A = E_z^2 L_w A, \tag{2.19}$$

where τ is the length of the laser pulse and A is the cross–sectional area. For a laser of length $c\tau = \lambda_p/2$, the amplitude of the wakefield driven is $E_z = a_0^2 m_e c\omega_p/e$. Assuming a constant wakefield across both; The laser's electric field is given by $E_L = m_e c a_0 \omega_0/e$. The pump depletion length of a laser pulse in the linear regime is then:

$$L_d = L_w = \frac{E_L^2}{E_z^2} c\tau, \tag{2.20}$$

$$L_d = \gamma_{wake}^2 \frac{c\tau}{a_0^2}. \tag{2.21}$$

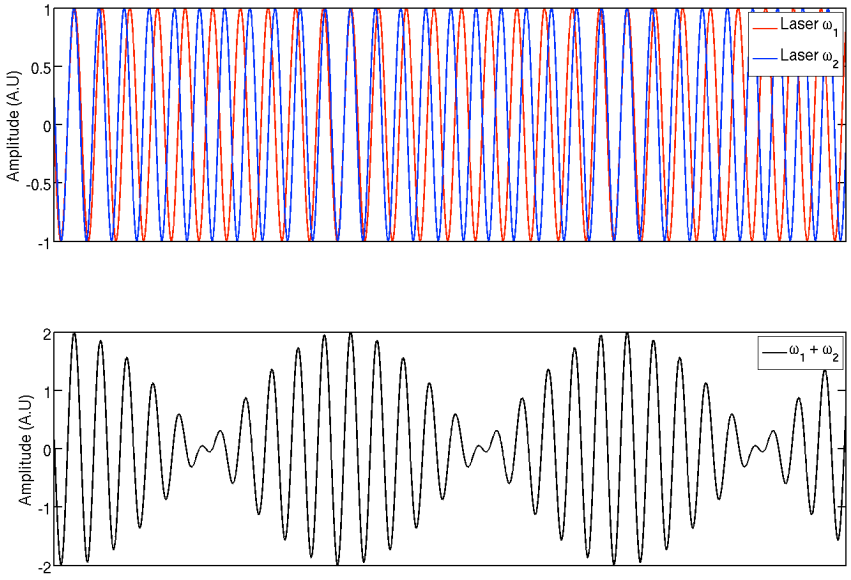

Figure 2.2.: Two laser beams of slightly differing frequencies, ω_1 and ω_2, red and blue lines respectively (top pane) and the super position of these two beams producing a beating laser beam with the envelope frequency being $\omega_2 - \omega_1$ (bottom pane).

2.2.4. Plasma Beatwave Acceleration (PBWA)

Plasma wakefield acceleration was first proposed in 1979 by Tajima and Dawson [8] who proposed to excite a plasma wake using an intense laser pulse, which would then be used to accelerate electrons. At the time, state of the art laser pulses were many nanoseconds long meaning only tenuous plasmas (whose plasma wavelengths were comparable to the laser pulse length) could be efficiently excited. The maximum achievable electric fields in such plasmas are of order kVm^{-1}, which were orders of magnitudes lower than those achieved in conventional accelerators.

As such the laser beatwave scheme was proposed. In this scheme a plasma wakefield is driven by the ponderomotive force generated by the beat envelope of two co–propagating laser beams of frequency ω_0 and ω_1, as shown in figure 2.2. The plasma frequency ω_p has to be matched to the difference of the two laser frequencies $\omega_p = \omega_1 - \omega_2$ in order for the laser beamlets to resonantly drive the wakefield to high amplitudes. This allows plasmas of much higher density to be excited. This scheme

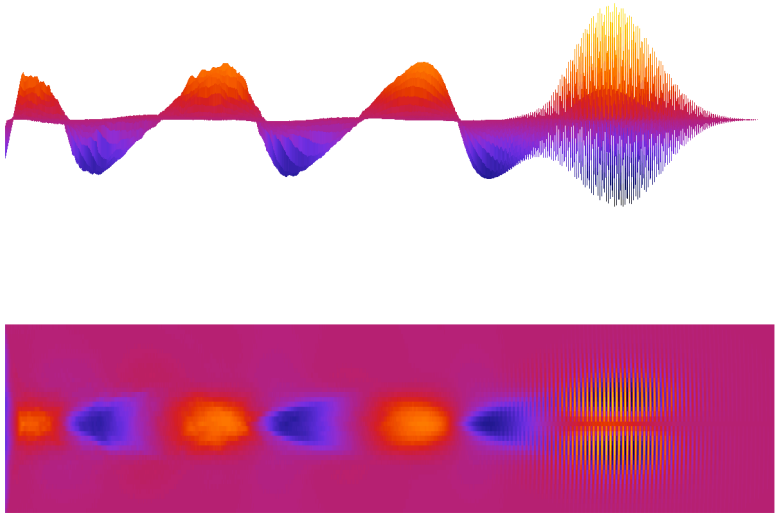

Figure 2.3.: The longitudinal electric field of a high intensity laser pulse propagating through a plasma and the resulting excited wakefield. The laser pulse is propagating to the right with the wakefield trailing behind it. The top pane shows the side view of the wakefield. The divergence of the wakefield profile from a sinusoid is caused by non–linear effects. The bottom pane shows a top down view.

however was found to have a major limitation. As the wakefield is driven to the non–linear regime the plasma wavelength increases, whilst the spacing between the laser beamlets remains the same. This resonant detuning of the plasma wave from the $\omega_p = \omega_1 - \omega_2$ condition limits the amplitude of the wakefields driven [42, 43].

2.2.5. Laser Wakefield Acceleration (LWFA)

Driving a wakefield with an ultra–short laser pulse, however, requires no tuning of plasma frequency nor has synchronisation issues of the laser beatwave scheme. A high amplitude wakefield can be driven by the ponderomotive force of a single high intensity laser pulse as shown in figure 2.3. Commercially available compact laser systems able to drive LWFA are cheap compared to dedicated particle–wakefield acceleration experiments. Also, the laser pulse can generate plasma as it propagates through a gas, relaxing the requirements of the plasma stage. Although they cannot

sustain wakefields over as long distances as particle beams, they do provide a readily available testbed for PWA experiments.

Ponderomotive Force

The ponderomotive force is the force experienced by a charged particle due to the gradient in intensity of an electromagnetic wave. For the ultra–short intense laser pulses used in laser wakefield acceleration this force is extremely large, and provides the main mechanism that couples the energy of the laser pulse to the plasma. It is stated for simplicity here and derived in appendix A.1.2.

$$F_P = -\frac{1}{4}\frac{e^2}{m\omega^2}\nabla E^2. \tag{2.22}$$

Where E is the electric field and ω is the angular frequency of the field and other parameters have their usual meaning. Note the ponderomotive force is proportional to the gradient of the electric field squared, ∇E^2, which is proportional to ∇I, where I is intensity, and is exceptional in that it is independent of the sign of the charged particle. That is to say that a charged particle will feel a force expelling it from the region of high intensity to a region of lower intensity, be it a plasma electron or an ion.

Laser Ionisation of an under dense gas

Ionisation of an under dense gas by an intense laser pulse can occur by tunnel ionisation [44], barrier suppression ionisation [45] and multi–photon ionisation [46]. Tunnel ionisation occurs when the potential barrier of an atom is drastically distorted by the presence of an intense electric field as shown in figure 2.4. An electron quantum tunnels through the lowered potential barrier to a region of equal or lower potential than its own. In the case of laser ionisation it is an alternating field that provides the distortion of the potential barrier. Modern ultra–short laser pulses have electric fields intense enough to entirely suppress the potential barrier, resulting in complete ionisation of atoms in regions exceeding the ionisation threshold. In the context of the laser–plasma simulations presented, the intensities of the lasers ($I \sim 10^{22}$ Wcm^{-2})

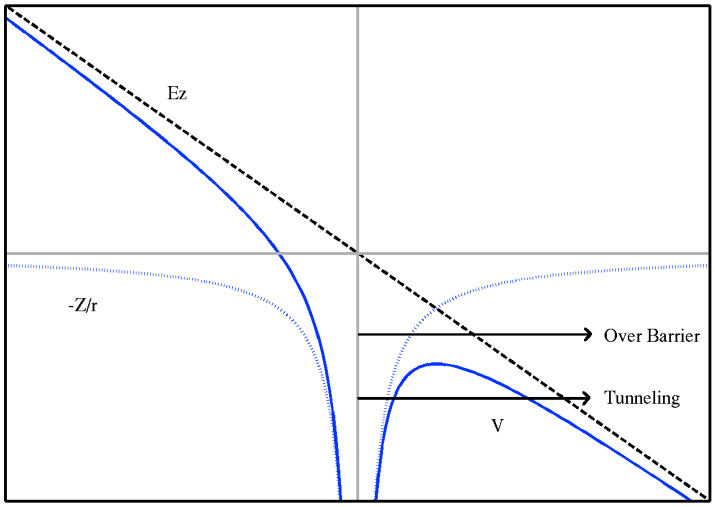

Figure 2.4.: The unperturbed potential experienced by an atomic electron is denoted by the dotted line ($-Z/r$). In the presence of a strong external electric field denoted by the dashed line (E_Z) the potential denoted by the solid line (V) is distorted allowing a previously trapped atomic electron to escape via barrier suppression ionisation or tunnelling ionisation.

exceed the ionisation threshold of Xenon ($I = 1.2 \times 10^{14}$ Wcm^{-2}) [47]. Therefore the gas is considered ionised before the trailing peak of the laser pulse arrives. As such ionisation effects will be neglected henceforth.

Self Focusing

In LWFA, laser pulses are focused to a spot size that is a few tens of the laser wavelength in order to achieve high intensities. As a consequence, the pulses rapidly diffract, diminishing their high intensities and their ability to drive a high amplitude wakefield. For a Gaussian beam propagating in free space along the $\hat{z}$ axis the width of the beam at position z is given by,

$$w(z) = w_0 \sqrt{1 + \left(\frac{z}{z_R}\right)^2} \tag{2.23}$$

Where z_R is the Rayleigh length and w_0 is the beam waist. The tighter the focus, the shorter the Rayleigh length. For each Rayleigh length of propagation, the intensity of the pulse decreases by a factor of two. This is undesirable as high amplitude electric fields need to be sustained over as long a distance as possible in order to achieve the greatest energy gains possible for the witness electron beam.

Another effect acting to disperse the laser pulse is refraction. An intense laser pulse propagating through a neutral gas will ionise it forming plasma. The plasma density will be highest on axis as the higher intensity meets higher ionisation thresholds, generating more plasma. This creates a transverse refractive index gradient that acts to defocus the laser pulse.

A competing and desirable effect is relativistic self focusing. As the plasma electrons are accelerated to relativistic velocities their mass increases. This in turn reduces the local plasma frequency, creating a refractive index gradient which increases with transverse distance from the axis of propagation. In addition, the ponderomotive force acts to dispel electrons from the axis, further increasing the refractive index gradient. The threshold for relativistic self focusing in terms of critical power is given by,

$$P_c = \frac{8\pi}{\epsilon_0}\left(\frac{m}{e}\right)^2 c^5 \left(\frac{\omega}{\omega_p}\right)^2, \tag{2.24}$$

or in a more convenient form,

$$P_c \simeq 17.5\left(\frac{\omega}{\omega_p}\right)^2 [GW]. \tag{2.25}$$

If the laser pulse has power equal to the critical power then the pulse will maintain its width, if it exceeds the critical power then it will focus to a tighter spot, enhancing its intensity.

2.2.6. Particle Wakefield Acceleration (PWFA)

A wakefield can be driven by the electric field of a passing charged particle beam. Particle beams tend to have higher total beam energy and group velocity within a plasma than their counterpart laser pulses, giving them greater depletion and dephasing lengths, allowing the wakefield to be driven over metres rather than centimetres. Electron beams have the advantage of experiencing the focusing region of the wakefield whilst driving a wake, whereas proton beams have higher total energy but instead experience a defocusing field whilst driving a wake. Such particle–beams that are suitable to drive PWA however are not readily available like the commercial laser systems. Instead existing facilities must treat their beams in order to effectively drive PWA.

Particle–Beam Driver Length

Here the ideal length of a Gaussian density profile particle–beam driving PWA is derived. To analyse the density profile of a plasma perturbed by a charged driving beam travelling close to c, consider the plasma in three regions. Region 1 is the plasma ahead of the driving beam. It is unperturbed as the beam is travelling close to c, and the beam's fields can not propagate faster than it. Region 2 is the plasma being perturbed by the beam as it passes and region 3 is the perturbed plasma behind the beam. Region 1 is trivial, region 2 is described by equation 2.9 without the laser perturbation term and region 3 is described by equation 2.7 with the amplitude of density oscillation determined by region 2. This derivation focuses on region 2 and then uses boundary conditions to find region 3. The beam is modelled as a Gaussian beam by the following equation:

$$n_b = \frac{N}{\sqrt{2\pi\sigma_z^2}} e^{\frac{-(z-ct)^2}{2\sigma_z^2}}, \tag{2.26}$$

where N is the number of particles in the beam, n_b is the beam's number density and σ_z is the length of the beam. Note that the Gaussian chosen for the beam profile has a constant area, normalised by the coefficient $1/\sqrt{2\pi\sigma_z^2}$. So the total charge of the beam remains constant. Therefore as the beam length increases, the beam

charge is distributed over a longer length and the charge density decreases. Later the case is considered where the total charge of the beam is not fixed, and is instead a function of the beam length.

Neglecting the laser term from equation 2.9 yields the expression for the number density perturbation caused by a negatively charged driver beam. The equivalent expression for a positively charged beam is simply,

$$\left(\frac{\partial^2}{\partial^2 t} + \omega_p^2\right)\frac{\Delta n_e}{n_0} = \omega_p^2 \frac{n_b}{n_0}. \tag{2.27}$$

Substituting the expression for the number density of the driving beam, equation 2.26, into equation 2.27 gives,

$$\left(\frac{\partial^2}{\partial^2 t} + \omega_p^2\right)\frac{\Delta n_e}{n_0} = \frac{\omega_p^2}{n_0}\frac{N}{\sqrt{2\pi\sigma_z^2}} e^{\frac{-(z-ct)^2}{2\sigma_z^2}}. \tag{2.28}$$

Transforming to the Quasi–Static frame, co–moving with the beam [48] we define $\xi = z - ct$ and $\tau = t$ and find,

$$\frac{d}{dt} = \frac{d\xi}{dt}\frac{d}{d\xi} + \frac{d\tau}{dt}\frac{d}{d\tau} = -c\frac{d}{d\xi} + \frac{d}{d\tau}. \tag{2.29}$$

The time τ is considered to be slowly varying during the transit time of the pulse. $d/d\tau$ can then be set to 0 in this co–moving frame. Equation 2.29 then becomes,

$$\frac{d}{dt} \simeq -c\frac{d}{d\xi}. \tag{2.30}$$

Expressing in terms of the plasma wavenumber $k_p = \omega_p/c$ and applying the above approximation to equation 2.28,

$$\left(\frac{d^2}{d\xi^2} + k_p^2\right)\Delta n_e = k_p^2 \frac{N}{\sqrt{2\pi}\sigma_z} e^{\frac{-\xi^2}{2\sigma_z^2}}. \tag{2.31}$$

We note that the form of this equation is $y'' + \omega^2 y = f_{(\xi)}$. Using Green's functions the solution to this general equation is,

$$y_{(\xi)} = \int_0^\infty G_{(\xi,\xi')} f_{(\xi')} d\xi' = \int_0^\xi \frac{1}{\omega} \sin(\omega(\xi - \xi')) f_{(\xi')} d\xi', \tag{2.32}$$

where $G_{(\xi,\xi')} = \frac{1}{\omega}\sin(\omega(\xi - \xi'))f_{(\xi')}$ for $0 < \xi' < \xi$ and 0 otherwise. Applying the solution to equation 2.31, an expression for the plasma density perturbation is found,

$$\Delta n_{e(\xi)} = k_p \frac{N}{\sqrt{2\pi}\sigma_z} \int_0^\xi \sin(k_p(\xi - \xi')) e^{\frac{-\xi'^2}{2\sigma_z}} d\xi'. \tag{2.33}$$

An important subtlety to note is that the integral in equation 2.33 is from 0 to ξ, where 0 is the point at which the beam begins and ξ is the point at which the beam ends. There are two problems, firstly the Gaussian is centred at 0 in the quasi–static frame, so integrating over these limits effectively ignores the first half of the beam, leaving an infinitely sharp leading edge. Plasmas respond very differently to hard edged beams and the integral as it stands does not represent the Gaussian beam. Secondly a Gaussian extends to $\pm\infty$, so the integration limits become $\pm\infty$ to encompass the entire beam giving,

$$\Delta n_{e(\xi)} = k_p \frac{N}{\sqrt{2\pi}\sigma_z} \int_{-\infty}^\infty \sin(k_p(\xi - \xi')) e^{\frac{-\xi'^2}{2\sigma_z}} d\xi'. \tag{2.34}$$

Integrating 2.34 the analytic expression for the variation in the electron density of a plasma being perturbed by a relativistic Gaussian proton beam of charge N and length σ_x is found,

$$\Delta n_{e(\xi)} = k_p N \sin(k_p \xi) e^{-\frac{1}{2}k_p^2 \sigma_z^2}. \tag{2.35}$$

Note that this linear solution applies to situations where the charge density of the driving beam is considerably less than the charge density of the plasma electrons, $n_{b_0} \ll n_e$.

Now the case where the charge density at the centre of the Gaussian beam profile is fixed is considered and as the beam length is increased the total charge of the beam increases — the variable–charge model. First n_b from equation 2.26 is modified by dropping the coefficient that conserved the charge of the Gaussian and instead defining the peak number density of the Gaussian beam as n_{b_0},

$$n_b = n_{b_0} e^{\frac{-(z-ct)^2}{2\sigma_z^2}}. \tag{2.36}$$

Integrating equation 2.36 and applying the same treatment as before equation 2.37 is found,

$$\Delta n_{e(\xi)} = k_p n_{b_0} \int_{-\infty}^{\infty} \sin(k_p(\xi - \xi')) e^{\frac{-\xi'^2}{2\sigma_z}} d\xi'. \tag{2.37}$$

Integrating 2.37, the analytical expression for the variation in the electron density of a plasma being perturbed by a proton beam of fixed peak charge density of length σ_x travelling close to c is found,

$$\Delta n_{e(\xi)} = \sqrt{2\pi}\sigma_z k_p n_{b_0} \sin(k_p \xi) e^{-\frac{1}{2}k_p^2\sigma_z^2}. \tag{2.38}$$

To find which value of σ_z yields the highest Δn_e, i.e. the highest amplitude wakefield, first neglect the non σ_z components,

$$f(\sigma_z) = \sigma_z e^{-\frac{k_p^2\sigma_z^2}{2}} \tag{2.39}$$

Differentiating equation 2.39 with respect to σ_z allows us to find the turning points for the expression. The turning points occur when the derivative is equal to zero.

$$f'(\sigma_z) = \left(1 - k_p^2\sigma_z^2\right) e^{-\frac{k_p^2\sigma_z^2}{2}}. \tag{2.40}$$

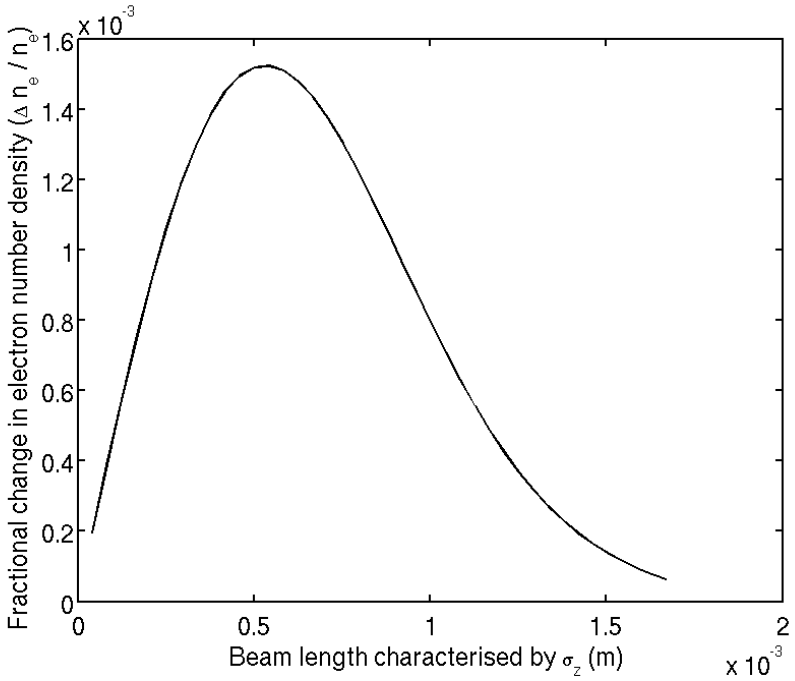

Figure 2.5.: The mathematical model, found in equation 2.38, for the amplitude of a one–dimensional wakefield excited by a Gaussian beam of constant charge. The fractional peak electron number density perturbation, i.e. the amplitude of the wakefield is plotted as a function of the driving beam's length.

Two values of σ_z set the derivative to zero, $\sigma_z = 1/k_p$ and $\sigma_z = \infty$. Differentiating once more and evaluating the function at these solutions determines if the solutions are a maximum or a minimum.

$$f''(\sigma_x) = \left(k_p^2\sigma_z^2 - 3\right) k_p^2\sigma_z e^{-\frac{k_p^2\sigma_x^2}{2}}. \tag{2.41}$$

$f''(1/k_p) < 0$ and is the maximum. Therefore we have found the ideal length for a Gaussian beam of peak charge density n_{b_0} to drive a plasma wakefield to be,

$$\sigma_{x_{ideal}} = \frac{1}{k_p}. \tag{2.42}$$

This result not only gives the ideal driver length but also shows that there is one unique optimum length for Gaussian profile beams. Figure 2.5 shows the amplitude of the wakefield driven as a function of beam length for the fixed number density model.

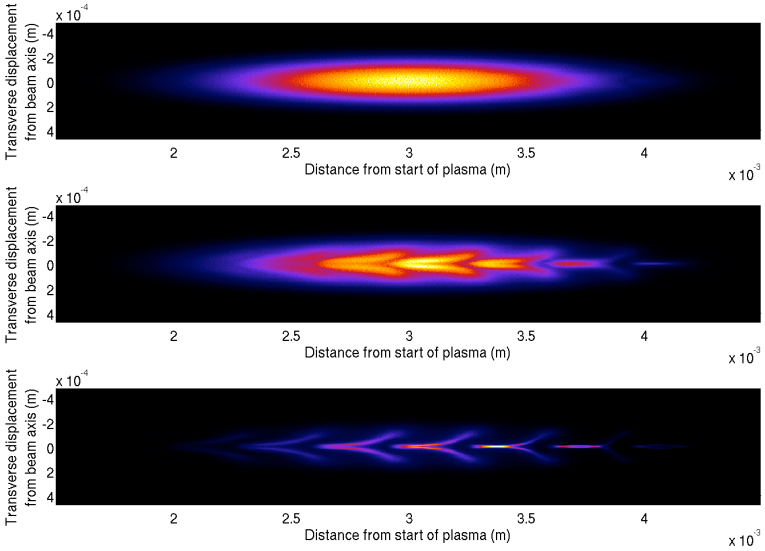

Figure 2.6.: A top down view of the number density of a particle beam undergoing strongly seeded self modulation. The top pane shows the initial number density of the beam before interaction with the plasma, the middle pane shows the head of the beam becoming micro–bunched via interaction with the wakefield and the bottom pane shows saturation of the self modulation instability with micro–bunches fully formed and evenly spaced at the plasma wavelength.

One–dimensional solutions can be usefully applied. For example, a very wide beam ($\sigma_r \gg \lambda_p$) will drive a one dimensional wakefield. Also a strong magnetic field can constrict the movement of charged particles to the field lines and reduce the system to one dimension. In both these situations equation 2.38 would model the response of the plasma to a Gaussian particle beam.

2.2.7. Self–modulated PWFA

For exciting wakefields in plasma densities of interest, particle–beam lengths have to typically be the order of $\sigma_z = 100$ μm to satisfy equation 2.43. Given that both proton and electron synchrotron beams are typically of length $\sigma_z > 10$ mm it would seem that existing particle beams are unsuitable for PWA. Long beams can, however, drive high amplitude wakefields via the self–modulation instability, so long as the initial amplitude of wakefield driven is sufficient to seed the self–modulation instability [49].

Take an electron beam that is significantly longer than the plasma period. The head of the beam will drive a low amplitude wakefield, exposing the trailing beam to weak focusing and defocusing regions. The beam electrons in the defocusing region will feel an off axis force, diminishing the number density, whilst the opposite is true for the electrons in the focusing region. This leads to an enhanced wakefield driving capability of the beam as the wakefield driven by the beam electrons in the focusing region constructively adds to the initial wakefield. A feedback loop is established resulting in an envelope modulated at the plasma frequency, as in figure 2.6. The growth rate of the self modulation instability for a long ($k_p\sigma_z \gg k_\beta z$), flat top, cylindrically symmetric narrow ($k_p\sigma_r \ll 1$) bunch at position $\xi = z - ct$ along the bunch is given by e^G [50], where,

$$G \simeq \frac{3\sqrt{3}}{4}\left(\frac{n_b}{n_0}(k_p\xi)(k_\beta z)\right)^{1/3}. \tag{2.43}$$

The self–modulation instability is also known to affect laser pulses that are longer than the plasma wavelength. Instead of the high amplitude electric fields found in wakefields affecting the number density profile of a long particle beam, the high and low density regions of a wakefield act to diffract and self focus regions of the laser pulse, forming a train of short pulses [51–53].

2.3. Betatron X–ray Generation

Electrons oscillating within a wakefield emit synchrotron radiation [54]. The spectrum, direction and power of this radiated light is well known in conventional insertion devices such as undulators and wigglers. By showing the trajectory of an electron within a wakefield is identical to that of those in these conventional insertion devices one can then assume the radiation characteristics are equivalent also.

2.3.1. Electron Trajectories within a Wakefield

By considering the radial electric field acting on a beam electron within a wakefield, the betatron frequency of the beam electron can be calculated. Consider a strongly driven wakefield in the blow–out regime. The electric field generated by the ion

channel at a distance r from the axis of propagation can be calculated using Gauss's law,

$$\nabla \cdot \mathbf{E} = \frac{\rho}{\epsilon_0} = \frac{-en_e}{\epsilon_0}. \tag{2.44}$$

Using cylindrical symmetry and integrating and setting the on–axis field to zero (i.e $E_r(r = 0) = 0$) yields,

$$\nabla \cdot \mathbf{E} = \frac{1}{r}\frac{d}{dr}(r\mathbf{E_r}) = \frac{-en_e}{\epsilon_0}, \tag{2.45}$$

$$\mathbf{E_r} = \frac{-en_e}{\epsilon_0}\frac{\mathbf{r}}{2}. \tag{2.46}$$

The force experienced by an electron at distance r from the channel is then,

$$\mathbf{F} = -e\mathbf{E} = \frac{e^2 n_e \mathbf{r}}{2\epsilon_0}. \tag{2.47}$$

The equation of motion is then,

$$\frac{d\mathbf{p}}{dt} = \mathbf{F} = \frac{m_e \omega_p^2 \mathbf{r}}{2}. \tag{2.48}$$

For ultra relativistic beams it can be assumed that the transverse momentum is small compared to the forward momentum of the beam (i.e $\gamma \simeq \gamma_0$ where γ_0 is the initial Lorentz factor of the beam). Expressing the relativistic momentum as $\mathbf{p} = \gamma m_e \dot{\mathbf{r}}$ and considering the radial component, equation 2.48 yields,

$$\ddot{\mathbf{r}} - \frac{\omega_p^2}{2\gamma}\mathbf{r} = 0. \tag{2.49}$$

Recognising this as simple harmonic motion, the frequency of this radial oscillation is,

$$\omega_\beta = \frac{\omega_p}{\sqrt{2\gamma}}, \tag{2.50}$$

where ω_β is the betatron frequency. The beam electrons, then, follow a sinusoidal path as they propagate through the plasma. The model given by equation 2.49 allows the trajectories to be calculated given the electron's initial momentum and transverse position.

It is known that electrons propagating through an undulator also follow a sinusoidal path [55] described by,

$$x(z) = \frac{K}{\beta\gamma k_u}\sin(k_u z), \tag{2.51}$$

where K is an important dimensionless parameter known as the undulator parameter and for conventional undulators is given by $K = eB_0\lambda_\mu/2\pi m_e c$ where B_0 is the magnetic field strength and λ_μ is the undulator period. For plasma wigglers the undulator parameter is given by,

$$K = \frac{\omega_b \gamma r_0}{c}, \tag{2.52}$$

where r_0 is the radial distance of the beam from the wakefield. For $K \gg 1$ the amplitude of the betatron oscillation is large compared to the wavelength of emitted radiation, so the emitted photons are spatially decoupled. Because of this, the emitted photons do not interfere, leading broad band emission. Such a device is known as a wiggler. For $K \ll 1$ the emitted photons are not spatially decoupled, as such self–amplified spontaneous emission occurs, leading to enhanced emissions of the undulator frequency and its harmonics. These devices are known as undulators.

2.3.2. Calculating Brilliance from Spectral Intensity

The spectral intensity radiated by a single accelerating charged particle [56] is given by,

$$\frac{d^2I}{d\omega d\Omega} = \frac{e^2\omega^2}{4\pi^2 c}\left|\int_{-\infty}^{\infty} \hat{\mathbf{s}} \times (\hat{\mathbf{s}} \times \beta) e^{i\omega(t-\hat{\mathbf{s}}\cdot\mathbf{r}(t)/c)}\mathrm{d}t\right|^2. \tag{2.53}$$

where I is the energy, Ω is the collection angle, ω is the frequency, $\hat{\mathbf{s}}$ is in the direction of observation and the expression is in CGS units.

The RDTX code used in later chapters to calculate the radiation emitted by undulating particles expresses the spectrum in terms of spectral intensity. The radiation generated by undulators and wigglers however, is commonly expressed as brilliance having units of photons s^{-1} mm^{-2} mrad^{-2} 0.1% BW^{-1}.

The RDTX code calculates the spectral intensity [57] of radiation emitted by a number N_P of accelerating point charges, with the jth particle at position $\mathbf{r}_j$ and with normalised velocity $\beta_j = \mathbf{v}_j/c$, in the far–field as,

$$\frac{d^2I}{d\omega d\Omega} = \frac{\mu_0 e^2 c}{16\pi^3}\omega^2\left|\int_{-\infty}^{\infty}\sum_{j=1}^{N_p} \hat{\mathbf{s}} \times \beta_j e^{i\omega(t-\hat{\mathbf{s}}\cdot\mathbf{r}_j/c)}\mathrm{d}t\right|^2, \tag{2.54}$$

where $\omega = v/\rho$, $\beta = |\mathbf{v}|/c$ being the normalised velocity and ρ being the orbit radius. The total number of radiated photons, N_B, can be calculated from this quantity,

$$N_B = N_b \frac{d^2I}{d\omega d\Omega}\frac{\Delta\omega}{\omega}\frac{\pi\theta_d^2}{\hbar}. \tag{2.55}$$

Assuming that the collection angle θ_d is small ($\theta_d < (\Delta\omega/\omega)^{1/2}$) so that the intensity distribution is flat over the virtual spectrometer's collection solid angle ($\Delta\Omega = \pi\theta_d^2$), the number of photons intercepted in a small bandwidth, $\Delta\omega = 0.001\ \omega$, about ω for an electron bunch of N_b electrons is given by equation 2.55. The peak brilliance is simply the photon flux per 0.1% bandwidth per unit volume in phase space, as

described by Q. Shen [58], and is then given by,

$$\hat{B} = \frac{N_B}{(2\pi)^3 \epsilon_x \epsilon_y \epsilon_E \tau}, \tag{2.56}$$

where ϵ_x and ϵ_y are the transverse emittances, ϵ_E is the longitudinal energy spread and τ is the beam length. Equations 2.55 and 5.1 are later used to convert the output from the RDTX code into peak brilliance.

2.4. Photon Acceleration and Wave Kinetics

Photon acceleration is a simple and general concept associated with electromagnetic wave propagation. It is best understood by relating it to the well known concept of refraction. Refraction is the change in wave vector suffered by a photon crossing a boundary between two optical media of differing refractive indices. Calling this space–refraction, we can imagine a symmetric situation where the refractive index of a medium varies in time. In such a situation the wave vector of the photon remains the same and instead the frequency of the photon changes. We can think of this process as time–refraction. Photon acceleration is the combination of these effects where a medium's refractive index varies with both space and time. Photon acceleration leads to longitudinal pulse compression of laser pulses of length $c\tau \approx \lambda_p$ within a plasma. Consider two adjacent wave fronts, 1 and 2, of a laser pulse propagating through an inhomogeneous plasma. The wavefronts will travel at different group velocities, v_1 and v_2 as they are in regions of different plasma densities, n_1 and n_2. As such, after a short time Δt the distance between the wavefronts in this example will vary, changing the wavelength by,

$$\Delta\lambda = (v_1 - v_2)\Delta t. \tag{2.57}$$

Given Δv is small relative to the change in wavelength, we can express the change in wavelength after a time Δt as,

$$\Delta\lambda = \Delta t \lambda_0 \frac{\partial v_\phi}{\partial x}, \tag{2.58}$$

where λ_0 is the wavelength of the laser and v_ϕ is the phase velocity of the laser. Then, the rate of change of the wavelength becomes,

$$\frac{\partial \lambda}{\partial t} = \lambda_0 \frac{\partial v_\phi}{\partial x}. \tag{2.59}$$

Moving to the speed of light frame, $\psi = t - x/c$ and $t = \tau$, note that,

$$\frac{\partial \psi}{\partial x} = \frac{-1}{c}, \tag{2.60}$$

$$\partial x = -\partial \psi c, \tag{2.61}$$

equation 2.59 becomes,

$$\frac{1}{\lambda_0}\frac{\partial \lambda}{\partial \tau} = \frac{-\partial v_\phi}{c \partial \psi}. \tag{2.62}$$

Equation 2.62 can then be expressed in terms of frequency using $\lambda = 2\pi c/\omega$ and $\partial\lambda = -\partial\omega 2\pi c/\omega^2$. The expression for the rate of change of frequency is then,

$$\frac{1}{\omega}\frac{\partial \omega}{\partial \tau} = \frac{c}{v}\frac{\partial v}{\partial \xi} = \frac{-\partial v_\phi}{c \partial \psi}. \tag{2.63}$$

Chapter 3.

Computational Methods

This chapter describes the simulation codes used in this thesis. A brief outline of each code is given and parameter scans and benchmarking of the main code EPOCH are presented.

3.1. EPOCH

EPOCH[1] is a plasma physics Particle In Cell (PIC) simulation code. The PIC method represents a collection of physical particles with a smaller number of macro–particles which are distributed on a underlying grid of fixed spatial resolution. These macro–particles interact self–consistently via the electromagnetic fields they produce [59, 60]. The fields generated by the motion of these macro–particles are calculated using a finite difference time technique and are projected onto the grid. Then these fields are used to calculate the forces on the macro–particles and update their velocities, and these velocities are then used to update the macro–particles positions as shown in figure 3.1. As a fully kinetic code, EPOCH is able to capture the full range of classical micro–scale behaviour of a collection of charged particles. PIC codes effectively represent a Lagrangian Monte–Carlo sampling of the phase space of Vlasov's equation[2]. EPOCH is based upon the particle push and field update algorithms developed by Hartmut Ruhl [61], with modules added to capture physics

[1]The EPOCH code used in this work was developed as part of an ESPRC funded project, Grant No, EP/G054950/1.

[2]The Vlasov equation in partial differential form, $\frac{\partial f}{\partial t} + \frac{\mathrm{d}\bar{\mathrm{q}}}{\mathrm{dt}} \cdot \frac{\partial f}{\partial \bar{q}} + \frac{\mathrm{d}\bar{\mathrm{p}}}{\mathrm{dt}} \cdot \frac{\partial f}{\partial \bar{p}} = 0$, where f is a function of generalised coordinates $\bar{q}$, $\bar{p}$ and t.

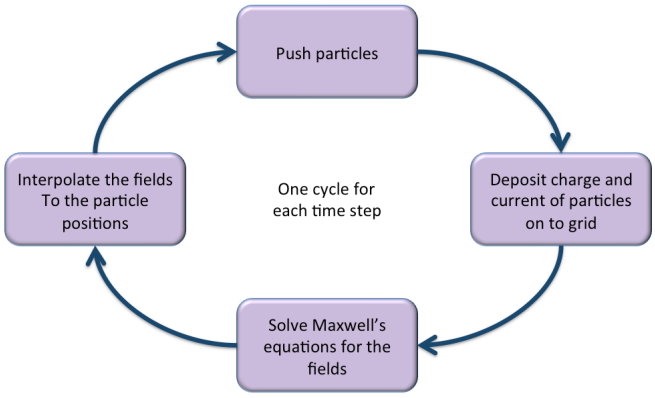

Figure 3.1.: The core program flow of particle–in–cell codes such as EPOCH.

such as collisions, ionisation and quantum electrodynamics driven radiation [62]. EPOCH was written with the intent of being used by a wide number of communities, with that in mind the code's output is in S.I. units, with the exception of charge which is normalised to that of the electron charge. EPOCH's input deck accepts either S.I. or cgs units.

3.1.1. Grid Resolution

When designing a simulation using a PIC code one has to provide a suitably fine grid such that the smallest scale structures within the simulation are fully resolved. Failure to do so will result in either a diminishing or absence of physical effects. A finer grid requires the code to not only have a higher number of total macro–particles to sufficiently populate each cell, but also to execute smaller time steps in order to satisfy the Courant condition. The Courant condition is a necessary condition for stability while solving partial differential equations numerically by the method of finite differences. For N dimensions the Courant condition is given by: $C = \Delta t \sum_{i=1}^{N} \frac{u_{x_i}}{\Delta x_i} \leq C_{max}$ [63] where Δt is the time step, u_x is the magnitude of velocity and Δx is the distance between grid points and C_{max} is the dimensionless Courant Number and is typically 1.

The runtime of a simulation scales with the total number of particles, $\tau_r \propto N_{Part}$, and is proportional to the number of time steps $\tau_r \propto N_{steps}$. By doubling the grid resolution in one dimension, the total number of particles needed to maintain the particles–per–cell is doubled and the number of time steps doubled. As such

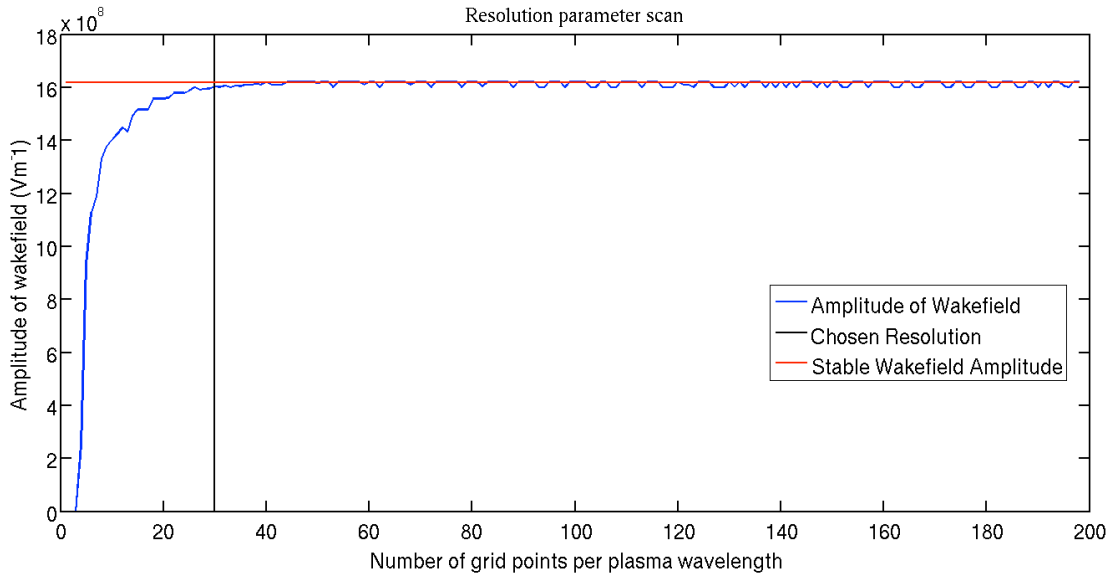

Figure 3.2.: A parameter scan of two hundred simulations over the number of grid points resolving the plasma wavelength. The amplitude of the wakefield driven (blue line) as a function of grid points per plasma wavelength is plotted. The chosen resolution for future simulations is indicated by the black line (thirty grid points per plasma wavelength). The red line indicates the amplitude of the wakefields driven in simulations with sufficiently high resolution to fully capture the physics of particle–beam driven plasma wakefields. For simulations where the spatial variations in the density profile of the drive beam are on the scale of, or greater than, the plasma wavelength, i.e. $\sigma_b \gtrsim \lambda_p$.

the runtime of a one dimensional simulation scales as $\tau_r \propto N_{points}^2$ of the grid size. It is necessary then to pick the coarsest resolution that fully captures the physics whilst minimising runtime of the simulation. To this end a simple particle–beam driven wakefield simulation was designed and the grid size scanned over (parameters found in table 3.1). The smallest scale of interest in the particle–beam simulations presented within this thesis is the plasma wavelength, and a main physical result of such simulations is the amplitude of the wakefield driven. The grid sizes scanned over were chosen such that they resolved the plasma wavelength with j points, where $j = 1 : 200$. Figure 3.2 shows the amplitude of the wakefield driven as a function of grid points per plasma wavelength in the two hundred simulations.

The resolution scan shows that forty five grid points per plasma wavelength and above yield a stable wakefield amplitude of $E_{zmax} = 1.62 \times 10^9$ Vm^{-1}. Note however, that above thirty grid points per plasma wavelength yields a wakefield of amplitude

Grid	Values	Beam	Values	Plasma	Values
n_x	$j \times 2$	*species*	e^-	*species*	H
n_z	$j \times 4$	$E\ (GeV)$	3	PPC	6
$grid\ width(m)$	$2 \times \lambda_p$	$\sigma_r\ (m)$	$\sqrt{2}/k_p$	$n_e\ (m^{-3})$	1.11×10^{23}
$grid\ length(m)$	$4 \times \lambda_p$	$\sigma_z\ (m)$	$\sqrt{2}/k_p$		
j	$1:200$	N	10^9		

Table 3.1.: Resolusion-scan parameters. For the grid parameters: n_x and n_z are the grid width and length respectively; j is the integer parameter scanned over; and *grid width* and *grid length* are the physical width and length of the grid. For the beam parameters: *species* is the particle composing the beam; E is the beam's individual particle energy; σ_r and σ_z are the beam's width and length respectively; and N is the number of particles composing the beam. For the plasma parameters: *species* is the ionised element composing the plasma, PPC is the number of particles per cell; and n_e is the plasma electron number density.

$E_{zmax} = 1.6 \times 10^9$ Vm^{-1} (99% of the stable wakefield amplitude) whilst requiring two thirds of the grid points. Below thirty grid points per plasma wavelength the amplitude of the wakefield is diminished significantly, falling to zero at one grid point per plasma wavelength. As such all PIC simulations presented henceforth were run with thirty grid points per plasma wavelength unless expressly stated otherwise.

3.1.2. Particles Per Cell

Another technical parameter of PIC simulations is the total number of macro–particles populating the grid, also expressed as particles per cell. The growth rate of noise of the electric field in PIC simulations is inversely proportional to the number of particles per cell, $\delta E = N_{ppc}^{-1/2}$. It is best then to choose a number of particles per cell that both minimises the runtime whilst keeping $\delta E \ll E$. A parameter scan over the number of particles per cell was run for a basic particle–beam driven plasma wakefield simulation with parameters summarised in table 3.2, in the same way as the resolution scan detailed above. Figure 3.3 shows the fractional deviation in the amplitude of the wakefield from a perfect sinusoid as a function of particles per cell. Six particles per cell was chosen as it achieves under 3% error and higher particles per cell give diminishing returns on the error reduction. As such all PIC simulations

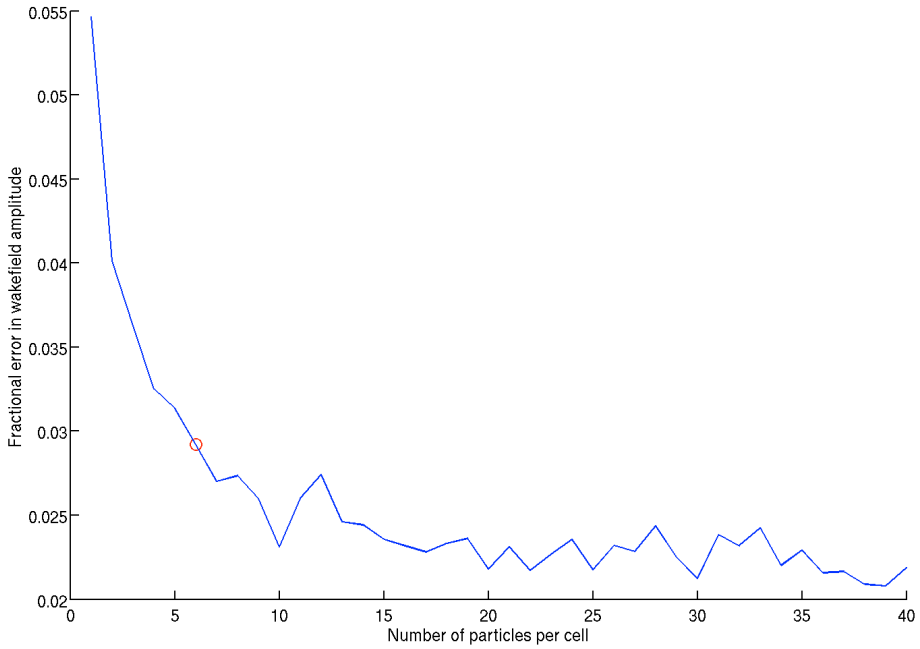

Figure 3.3.: The fractional error of the amplitude of a wakefield driven over a range of particle-per-cell simulations.

Grid	Value	Beam	Value	Plasma	Value
n_x	200	*species*	e^-	*species*	H
n_z	400	E (GeV)	3	PPC	$1:1000$
grid width (m)	$2 \times \lambda_p$	σ_r (m)	$\sqrt{2}/k_p$	n_e (m^{-3})	1×10^{20}
grid length (m)	$4 \times \lambda_p$	σ_z (m)	$\sqrt{2}/k_p$		
		N (e^-)	1×10^9		

Table 3.2.: Particles–per–cell–scan parameters. Parameters as defined in table 3.1.

presented henceforth were run with six particles per cell unless expressly stated otherwise.

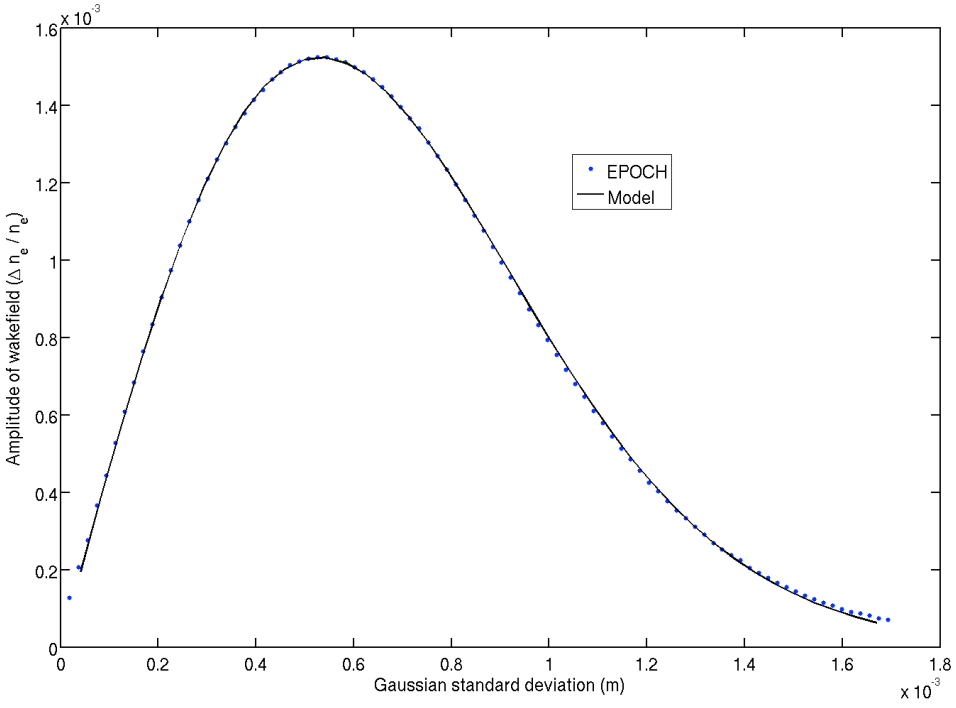

Figure 3.4.: The beam length of a driving beam plotted against the amplitude of the resulting plasma density perturbation. Data are from simulations using the PIC code EPOCH (blue dots). The model (black line) is that derived in section 2.2.6.

3.1.3. Benchmarking

To validate the code EPOCH for use in simulating plasma wakefield acceleration its predictions were compared to the predictions of the theoretical model derived in the theory section given by equation 2.38. Figure 3.4 plots the fractional number density perturbation of the plasma as a function of beam length. The theoretical model gives the electron number density perturbation caused by a passing Gaussian beam.

A true Gaussian extends infinitely in both directions. When designing a simulation, one has to truncate the Gaussian beam at an arbitrary point in order to fit it into the simulation window. As such, the model was adapted to yield the electron number density perturbation caused by a truncated passing Gaussian beam, as detailed in appendix A.2.1. A parameter scan over driver beam length was performed with EPOCH, whose parameters are found in table 3.3. Figure 3.4 shows close agreement

Grid	Value	Beam	Value	Plasma	Value
n_x	200	*species*	p^+	*species*	H
n_z	400	E (GeV)	3	PPC	6
grid width (m)	$2 \times \lambda_p$	σ_r (m)	$\sqrt{2}/k_p$	n_e (m^{-3})	10^{20}
grid length (m)	$4 \times \lambda_p$	σ_z (m)	$\sqrt{2}/k_p \times j/50$		
j	1 : 100	n_{b_0}/n_e	10^{-3}		

Table 3.3.: Beam-length-scan parameters. n_{b_0} is the peak beam number density, n_e is the plasma electron number density and other parameters are as defined in table 3.1.

between the fractional plasma density perturbation caused by the Gaussian beam as predicted by the theoretical model and as calculated by EPOCH.

3.1.4. EPOCH Analysis software

A bespoke graphical user interface program, EpochGUI, was written to expedite analysis of EPOCH simulations. EpochGUI was written by myself with contributions from F. Keeble and J. Leland. The program is designed so the user can quickly preview any data set present in the time step of interest, as shown in figure 3.5, compare two data sets evolving with time, compile a range of time steps into movies at the desired view angle and queue up arbitrary numbers of movies to be compiled as shown in figure 3.6. EpochGUI is available for both Mac and Linux environments.

EPOCH is bundled with numerous MATLAB functions that aid in handling the simulation data. However, a drawback is that to access a single dataset within a time step, the whole time step must be loaded into memory. Given that individual time steps can exceed several gigabytes in size this is both a time and resource intensive task. EpochGUI first scans the time step of interest for all the names of data sets it contains, returning a drop down menu to the user. The user then chooses the data set of interest and EpochGUI extracts only that array from the time step. By dynamically reading the data sets present within each time step, EpochGUI has proven to be future–resistance to updates to EPOCH. In practice this speeds up

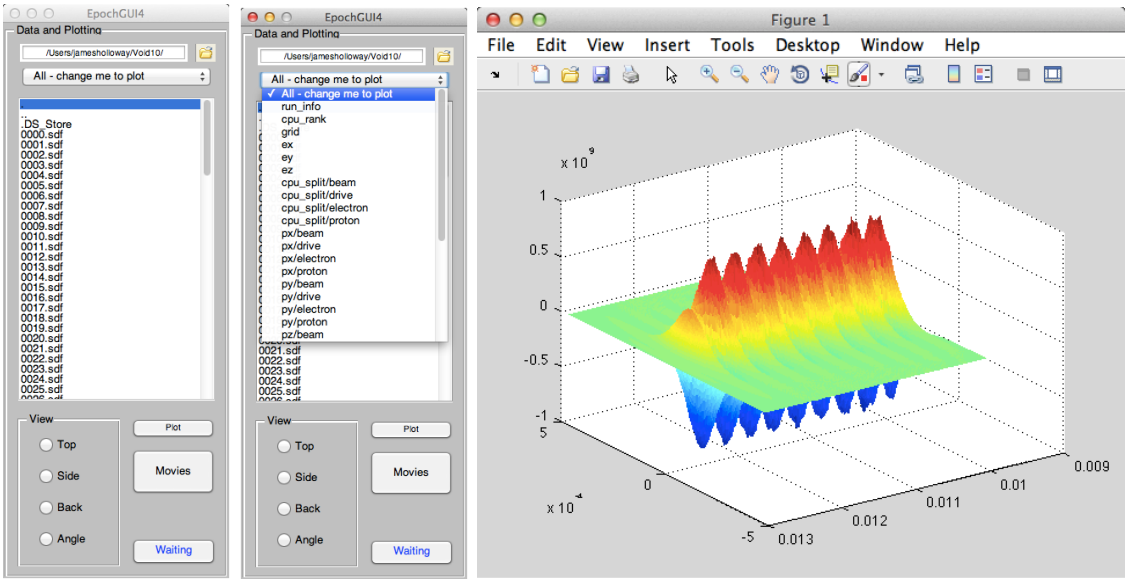

Figure 3.5.: The EpochGUI program with a directory containing EPOCH time steps selected (left pane), EpochGUI displaying the detected datasets within an EPOCH time step (middle pane) and the electric field of a a time step plotted by EpochGUI (right pane).

the access time of the data by an order of magnitude, crucial for previewing the evolution of datasets in real time.

Given the total size of a simulation's output can exceed terabytes of data, compiling a movie from a dataset takes significant amounts of time on high end computers. For this reason EpochGUI was written to allow the user to queue up several movies to compile sequentially. This way interactionless compilation of movies of many variables can be achieved overnight. Whilst compiling a movie, EpochGUI only holds the current times step's data set in memory, discarding the set once the movie frame has been generated and saved, relaxing the memory requirements of the program.

3.2. Radiation Damped Electron Tracking Code (RDTX)

RDTX code is designed to calculate radiation spectra from arbitrary electron orbits in prescribed potential structures [64]. Particles populate a grid, as with other PIC codes, and are pushed using a fourth order Runge–Kutta integrator with a

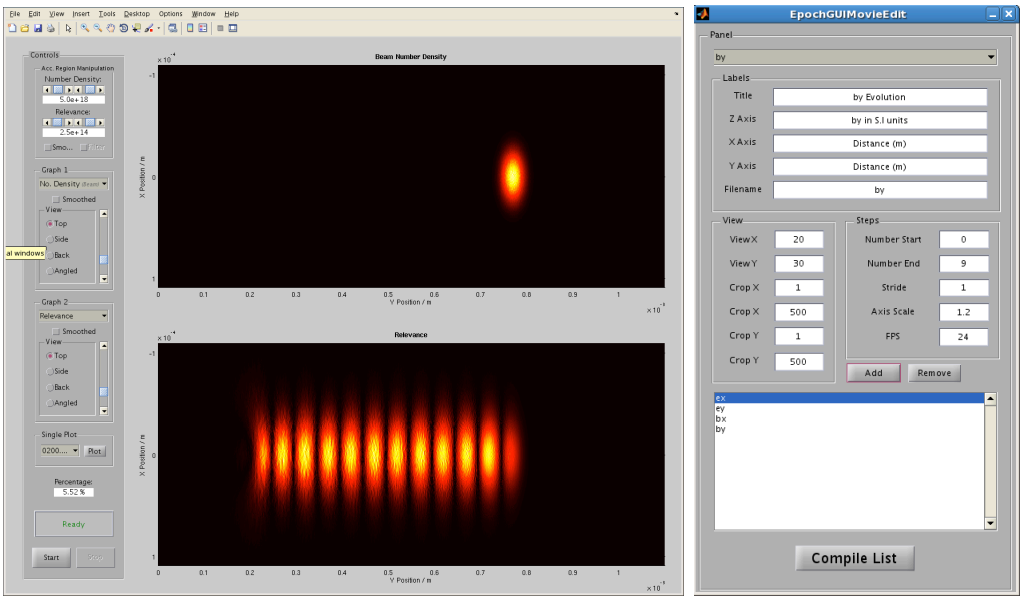

Figure 3.6.: The EpochGUIMovieMaker (right pane) with four movies queued for compilation (ex, ey, bx and by variables) and the EpochGuiRealTime previewer (left pane) displaying an electron driving beam in its upper pane and the resulting wakefield within its lower pane.

modified Lorentz–Abraham–Dirac equation of motion. The fourth order Runge–Kutta integrator is a numerical method that approximates the solutions of ordinary differential equations in a temporally discretised system. Being a fourth order method yields a total accumulated error of order $O(h^4)$, where h is the size of the time step.

As the potential is prescribed and not dynamically calculated, RDTX can simulate a beam–plasma interaction orders of magnitude quicker than fully kinetic PIC codes such as EPOCH or OSIRIS. Having a prescribed potential however means that it is unsuitable for simulating situations where the wakefield evolves significantly throughout the interaction, such as self–modulation simulations. As such, RDTX is used to calculate the radiated spectra from particle beam–plasma simulations that have been performed in EPOCH once the wakefield has evolved to a stable state.

A feature of RDTX is a virtual spectrometer, which measures the spectral intensity of radiation emitted by the moving charge being simulated. This feature is useful for assessing the properties of potential light sources such as charge undulating in a wakefield as discussed later in section 5. The benchmarking of the core algorithm of RDTX against analytic theory is detailed d in the cited paper by the code's author, A.G.R. Thomas [65]

3.3. FROGed

The code FROGed determines the phase and intensity profile of the laser pulse that generates an experimentally recorded FROG trace. This non trivial task is performed by starting with a hypothetical laser pulse, determining the FROG trace produced by the hypothetical pulse and calculating the error between the FROG trace of the hypothetical laser pulse and the experimentally recorded trace. The code then attempts to improve upon the guess and minimise the error between the two traces by applying several retrieval algorithms. The retrieval algorithms are briefly summarised here, with a more in–depth discussion provided by M. Streeter [66]. The Data Constriants method, Generalized Projections method and the Genetic Algorithm method are employed to minimise the error in the order stated.

Each retrieval algorithm is capable of reducing the difference between the hypothetical and experimental FROG trace, however, individually they are prone to becoming stuck in local minima and will not converge to the correct solution. As such a master algorithm switches between the different retrieval algorithms after a certain number of iterations yields no improvement on the discrepancy between the two FROG traces. FROGed is later used to retrieve the intensity and phase of laser pulses emerging from laser–plasma interactions.

3.4. Limitations of PIC Codes

PIC codes provide valuable insight into laser–plasma and beam–plasma interactions, making predictions which have good general agreement with experiment [10, 67]. They do have limitations however.

Firstly they are computationally intensive, requiring hundreds of cores on high performance computers. A typical realistic particle beam–plasma simulation takes between two and four days to complete running on 256 cores. When introducing a laser pulse the required resolution increases significantly and the largest of such simulations completed took ten days to complete on 4096 cores. These simulations resolve the plasma wavelength of a tenuous plasma ($n_e \approx 10^{23}$ m^{-3}). When increasing the plasma density to solid densities, whilst resolving small scales such as the Debye Length (given by equation 2.1), the runtime becomes prohibitive. Failure to resolve

the Debye length results in numerical heating of the plasma, but can be safely ignored if the heating time of the laser–plasma or beam–plasma interaction is greater than that of the numerical heating.

PIC codes are commonly collisionless, again making them more suitable for tenuous plasmas. EPOCH has an optional collisional module but it is in the early stages of testing.

Chapter 4.

Conventional Beams Driving Wakefields

A novel numerical study is presented, showing that existing third generation light sources can produce X–ray pulses with equally unique properties as state–of–the–art fourth generation sources, by undulating their beams within plasma wakefields.

This study shows that by longitudinally micro–bunching a long electron beam an X–ray pulse can be generated with orders of magnitude enhancement to both brilliance and photon energy when propagated through a plasma stage when compared to conventional magnetic insertion devices. First the micro–bunching technique is refined in simulations on the $\sigma_z = 26$ mm long electron beam generated in the booster

Beam	Value
E (GeV)	3
$\Delta E/E$	0.007
ϵ (nm rad)	140
σ_z (mm)	26
σ_r (mm)	1.58
N	1.25×10^{10}

Table 4.1.: Diamond beam baseline parameters. Where E is the electron energy, $\Delta E/E$ is the longitudinal energy spread, ϵ is the normalised emittance, σ_z is the beam length, σ_r is the beam radius and N is the number of electrons.

Figure 4.1.: The transfer line between the Diamond Light Source's inner booster ring and outer storage ring (red circle) where the available 6 m of beam line is found. A tuneable quadrupole is positioned before the start of the 6 m of beam line (blue circle) allowing control over the radial size of the Diamond beam. Picture courtesy of Dr. Michael Bloom.

section of the Diamond Light Source (referred to hereafter as the Diamond beam, parameters found in table 4.1). After, the technique is applied to the shorter, lower emittance Diamond beam found in the storage ring and the radiation produced is studied.

The production mechanism ensures the pulses are radially polarised on creation. Also, a micro–bunched electron beam is demonstrated to be an effective wakefield driver in itself, providing a potential new cost–effective route to a reliable X–ray free electron laser generation.

The first part of this chapter is concerned with testing various treatments to the Diamond beam to make it an effective wakefield driver (i.e. able to drive a well defined wakefield of $E_z > 1$ GVm^{-1}). Once a regime is found, an optimisation study is performed and a detailed beam line is designed and fully simulated demonstrating the Diamond beam can drive high amplitude wakefields.

As this work forms an experimental proposal where the proposed beam line would be installed at the Diamond facility, a strict requirement is that the beam line fits within the 6 m of beam line available between the inner booster and outer storage ring (figure 4.1).

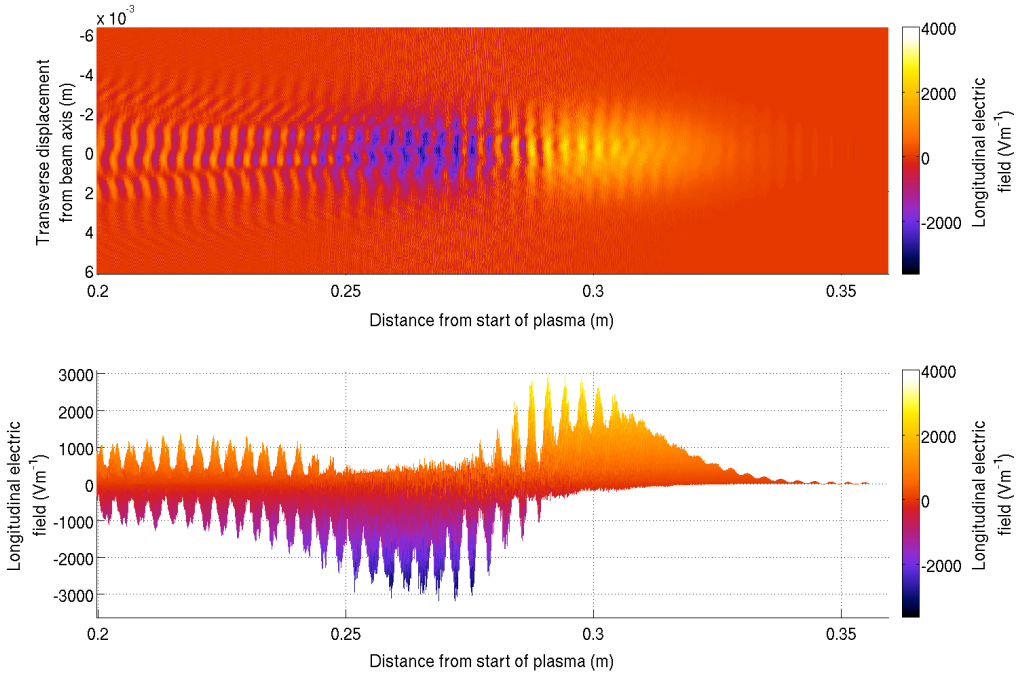

Figure 4.2.: Top view (top pane) and side view (bottom pane) of the wakefield driven by the baseline Diamond beam within a plasma of number density $n_e = 10^{20}$ m^{-3} after 200 mm of propagation within the plasma.

4.1. Compressing and Cutting the Diamond Beam

As discussed in the introduction, particle beams found in modern synchrotrons and linear accelerators are typically too long to drive a high amplitude wakefield. An obvious solution is to longitudinally compress a beam with a series of magnetic chicanes, such that $\sigma_z = 1/k_p$, making the beam an effective wakefield driver. Another approach is to shape the density profile of the beam such that the head sharply increases in number density over a distance comparable to the plasma wavelength, i.e. to cut the beam. A beam with a sharp rise time kicks the plasma electrons abruptly in much the same way as a short beam does. A third approach is to radially compress the beam, increasing its on–axis number density. This section presents simulations of these schemes.

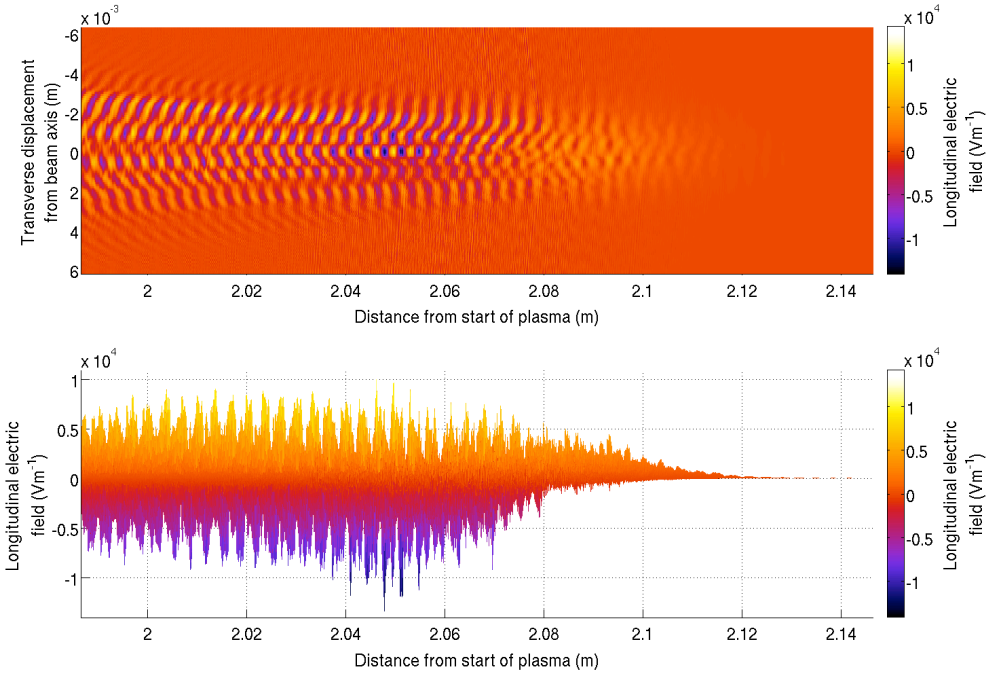

Figure 4.3.: Top view (top pane) and side view (bottom pane) of the wakefield driven by the baseline Diamond beam within a plasma of number density $n_e = 10^{20}$ m^{-3} after 2 m of propagation within the plasma.

4.1.1. Baseline Diamond Beam

The Diamond beam has a beam length of $\sigma_z = 0.026$ m which would effectively excite a wakefield in a plasma of density $n_e = 8.38 \times 10^{16}$ m^{-3}, as described by equation 2.43. Such a plasma supports a maximum electric field of $E_{zmax} = 2.78 \times 10^7$ Vm^{-1} before succumbing to wave breaking, given by equation 1.1. This electric field is in the region of those achievable by conventional accelerators, therefore the simulations performed herein are at higher plasma densities.

The initial plasma density of $n_e = 1 \times 10^{20}$ m^{-3} was chosen as the Diamond beam shares similarities to the Super Proton Synchrotron (SPS) proton beam at the LHC, which the Advanced Wakefield Experiment (AWAKE) collaboration proposes to use to drive PWFA in this plasma density region [68]. They are both long conventional particle beams with the SPS and Diamond beam having gamma factors of $\gamma = 481$ and $\gamma = 5871$ respectively. Furthermore, this initial plasma number density has a plasma wavelength of $\lambda_p = 3.34$ mm which is closer to the length of the Diamond

Grid	Value	Beam	Value	Plasma	Value
n_x	130	*species*	e^-	*species*	H^+
n_z	1660	E (GeV)	3	n_e (m^{-3})	10^{20}
grid length (m)	0.166	σ_r (m)	1.58×10^{-3}		
grid width (m)	0.01265	σ_z (m)	26×10^{-3}		
t_{end} (s)	6.66×10^{-9}	N	1.25×10^{10}		
ppc	6	ϵ (nm rad)	140		

Table 4.2.: Baseline Diamond beam simulation parameters. For the grid parameters: n_x and n_z are the grid width and length respectively; *grid width* and *grid length* are the physical width and length of the grid, t_{end} is the runtime of the simulation and *ppc* is the number of particles per cell. For the beam parameters: species is the particle composing the beam, E is the individual beam's particle energy, σ_r and σ_z are the beam's width and length respectively, N is the number of particles composing the beam and ϵ is the normalised beam emittance. For the plasma parameters: *species* is the ionised element composing the plasma and n_e is the plasma electron number density.

beam than that of higher density plasmas, meaning the Diamond beam's length is closer to that of the optimum driver length. At this density the plasma can support a maximum electric field of $E_z = 9.63$ GVm^{-1}, far exceeding conventional accelerator limits. Figure 4.2 displays the longitudinal electric field excited within the plasma by the baseline parameter Diamond beam after 20 mm of propagation into the plasma, which is a superposition of the driven wakefield and the beam's electric field.

A maximum of $E_z = 2.4$ kVm^{-1} is achieved, which is four orders of magnitude lower than the maximum electric fields attainable in conventional accelerators. Furthermore, the top pane of figure 4.2 shows that the wakefield excited is not made of distinct, regularly spaced smooth buckets in which particles can be reliably accelerated. The initial wakefield driven by the baseline Diamond beam is therefore unsuitable for PWFA.

Co–propagating a particle beam with its own wakefield modulates the density profile of the beam, enhancing its wakefield driving capabilities as discussed in section 2.2.7. Figure 4.3 shows the electric field of the Diamond baseline simulation after 2 m of propagation through the plasma. Note that although the maximum wakefield has increased to $E_z = 10$ kVm^{-1}, the quality of the wakefield has decreased significantly

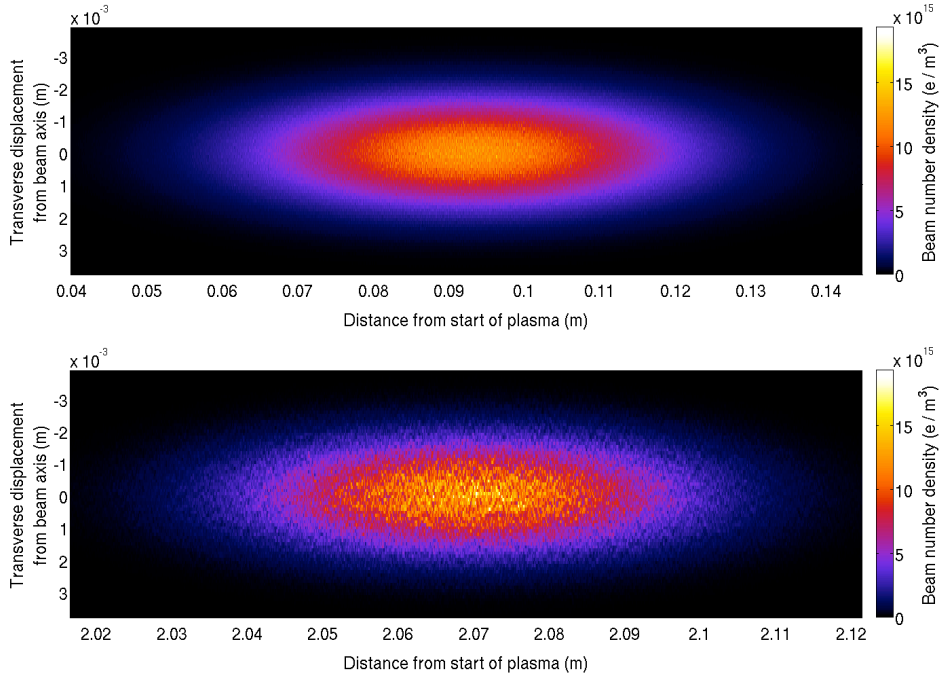

Figure 4.4.: Top view of the baseline Diamond beam before (top pane) and after (bottom pane) 2 m of propagation through a plasma of number density $n_e = 10^{20}$ m^{-3}.

as the individual buckets are less defined. Figure 4.4 shows the number density of the Diamond beam before and after 2 m of propagation through the plasma. Note that the density profile of the beam has not been modulated significantly and shows no micro–bunching at the plasma wavelength. The baseline Diamond beam is therefore unsuitable for PWFA.

4.1.2. Ideal Compression of the Diamond Beam

Ideally, the Diamond beam would be compressed longitudinally and radially such that $\sigma_z = \sigma_r = 1/k_p$[1]. A parameter scan over plasma density was performed to see the amplitude of the wakefields driven by the ideally compressed Diamond beam, parameters found in table 4.3. The ideally compressed Diamond beam drives an initial wakefield in excess of $E_z = 1$ GVm^{-1} in plasma densities of $n_e = 1 \times 10^{22}$

[1]Theoretically a point–like beam would drive a higher amplitude wakefield, but this is not considered as it is technically unfeasible.

Grid	Value	Beam	Value	Plasma	Value
n_z	120	*species*	e^-	*species*	H^+
n_y	60	E (GeV)	3	n_e (m^{-3})	$0.278 \times 10^{20} \times 2^j$
grid length (m)	4 λ_p	σ_r (m)	$\sqrt{2}/k_p$	j	3 : 20
grid width (m)	2 λ_p	σ_z (m)	$\sqrt{2}/k_p$		
t_{end} (s)	4 λ_p/c	N	1.25×10^{10}		
ppc	6	ϵ (*nmrad*)	140		

Table 4.3.: Ideally compressed Diamond beam density scan parameters. j is the parameter scanned over and other parameters are as previously defined in table 4.2.

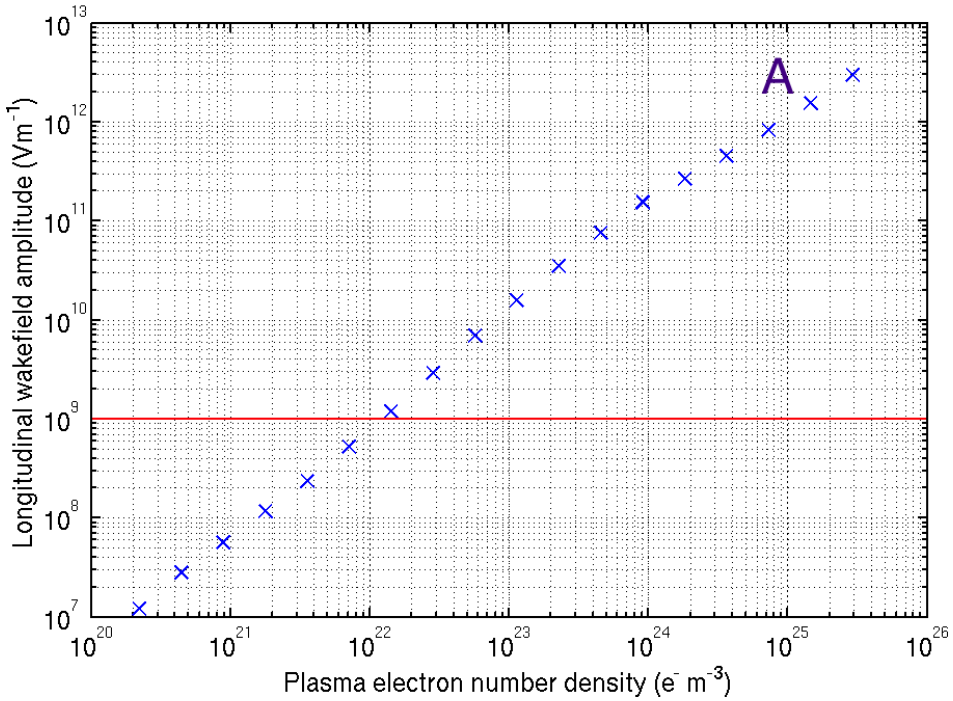

Figure 4.5.: The initial amplitude of the wakefield driven by the ideally compressed Diamond beam plotted as a function of plasma density. The length and width of the Diamond beam have been matched to the plasma such that $\sigma_z = \sigma_r = \sqrt{2}/k_p$. The red line indicates a wakefield of 1 GVm^{-1}.

m^{-3} and above, as shown in figure 4.5. The highly compressed beams diverge rapidly however, diminishing the amplitude of the wakefield driven. The simulation highlighted in figure 4.5 by label A drives an initial wakefield of $E_z \simeq 1$ TVm^{-1}. This high incredibly high amplitude wakefield however, is extremely short lived. The initial wakefield of $E_z \simeq 1$ TVm^{-1} decreases to $E_z \simeq 0.4$ TVm^{-1} after 2 λ_p of propagation as the beam's radius rapidly increases from $\sigma_r = 1/k_p$ to $\sigma_r \simeq 2/k_p$. The rapidly expanding driver beam can only drive the high amplitude wakefield for very short distances, therefore limiting the total energy gain of a witness beam.

At the plasma density of $n_e = 1 \times 10^{22}$ m^{-3}, the Diamond beam is longitudinally compressed to $\sigma_z = 75.2$ μm, driving a wakefield of amplitude $E = 1$ GVm^{-1}, making it a more viable parameter set. Investigations into compressing the SPS proton beam concluded it would take 600 m of beam line to compress the beam from $\sigma_z = 120$ mm to $\sigma_z = 3.6$ mm to make it suitable for the AWAKE experiment [69]. According to the linear theory of magnetic bunch compression it would take approximately 40 m of beam line to compress the Diamond beam to $\sigma_z = 75.2$ μm. Given the hard constraint of 6 m of beam line and the softer constraint of total cost of the experimental proposal, compressing the Diamond beam in this way was deemed unfeasible.

4.1.3. Radial Compression

Radial compression of a particle beam is a straight forward task compared to longitudinal compression. Quadrupoles in the existing Diamond beam line can be used to focus the Diamond beam to a smaller waist at the entrance of the plasma stage. Radially compressing a particle beam increases the peak number density and therefore the amplitude of the wakefield driven. The radial compression simulation has the same parameters as the baseline Diamond simulation, found in table 4.2, but has the beam's radius decreased by a factor of ten. This increases the beam's peak number density by a factor of one hundred. Figure 4.6 shows the radially compressed beam driving a wakefield of $E_{zmax} = 4$ MVm^{-1} after 2 m of propagation, significantly below the $E_z = 1$ GVm^{-1} of interest. The wakefield quality degrades over the 2 m of propagation, with high amplitude off–axis electric fields and low on–axis fields. This is due to the beam rapidly expanding over the 2 m, hosing significantly as a result of the radial compression, as shown in figure 4.7. The effective temperature of a

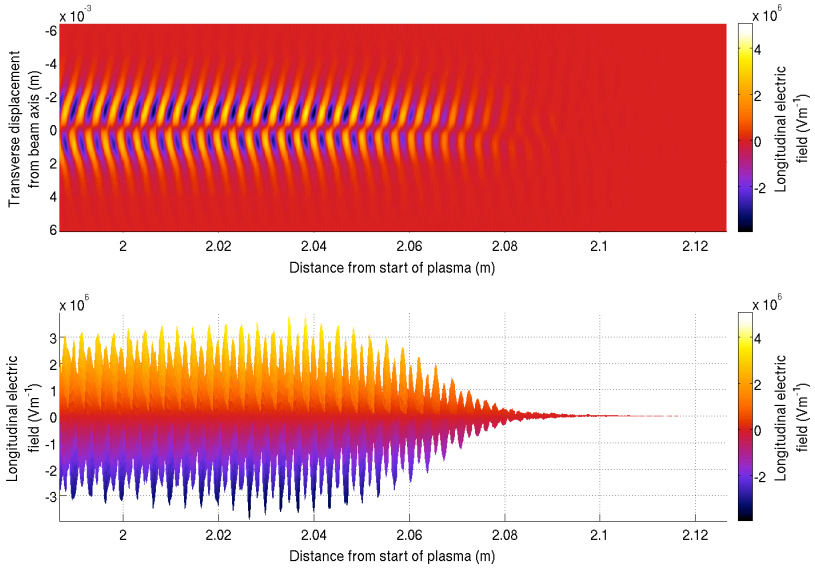

Figure 4.6.: The top view (top pane) and side view (bottom pane) of the wakefield driven by the radially compressed Diamond beam after 2 m of propagation within a plasma of number density $n_e = 10^{20}$ m^{-3}. Hosing can be seen in the form of pronounced transverse asymmetry in the number density of the beam (the zig–zaging along the length of the beam.

particle beam is given by,

$$T_{eff} = \frac{E^2 \epsilon^2}{m_e c^2 k_B \sigma_r^2}, \tag{4.1}$$

where ϵ is the normalised emittance, k_B is the Boltzmann constant, σ_r is the beam's radius, E is the beam's energy and the other terms have their usual meaning. Given that the emittance of a beam is constant, compressing the beam radially by a factor of ten increases the beam's temperature by a factor of one hundred to $T_{eff} = 1.59 \times 10^{11}$ K. The low amplitude focusing fields of the wakefield driven is insufficient to contain the now hotter beam. Further compression results in a greater divergence. Therefore the radially compressed Diamond beam is not an effective wakefield driver.

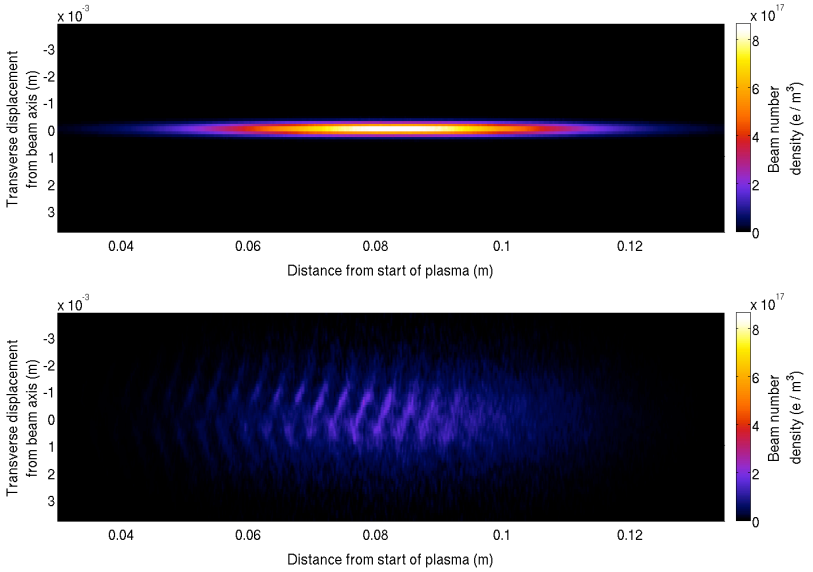

Figure 4.7.: The radially compressed Diamond beam before (top pane) and after (bottom pane) 2 m of propagation through plasma of number density $n_e = 10^{20}$ m^{-3}.

4.1.4. Half Cut

Introducing a sharp cut to the density profile of the beam is a technically challenging, but feasible task. A longitudinally cut Diamond beam was simulated, discarding the front half of the beam, giving a sharp leading edge to the density profile. Figure 4.8 shows the $E_z = 1.05$ MVm^{-1} wakefield driven by the half–cut beam after 2 m of propagation through the plasma. The wakefield is well defined and of a much higher quality than those presented in the preceding simulations — albeit a factor of four lower than the radially compressed Diamond beam. The half–cut beam experiences this high quality wakefield throughout the 2 m of propagation, however the initial wakefield driven of $E_z = 1$ MVm^{-1} does not sufficiently seed the self–modulation instability and there is no micro–bunching to the Diamond beam after 2 m as shown in figure 4.9. Given the beam line required to half–cut the beam in addition to an extended stage for the self–modulation instability to saturate, half–cutting the Diamond beam was considered unsuitable for the purposes of driving a high amplitude wakefield.

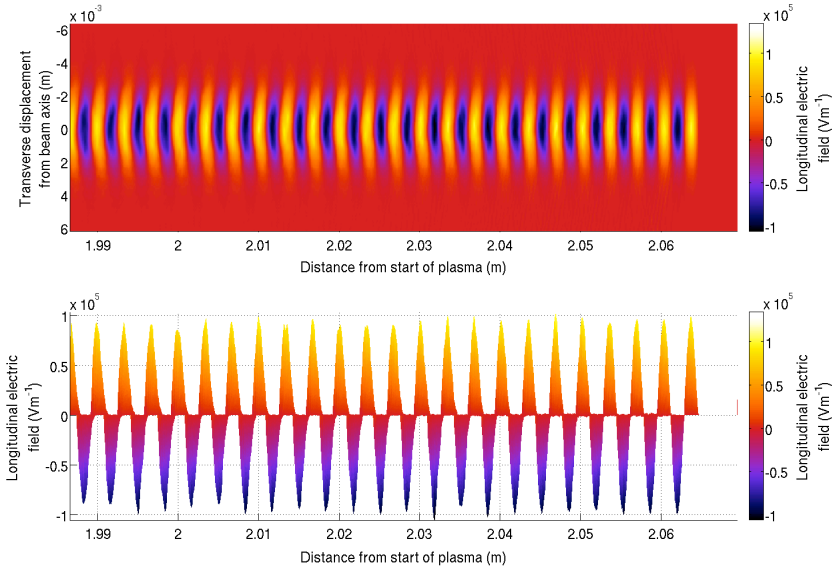

Figure 4.8.: The top view (top pane) and side view (bottom pane) of the wakefield driven by the half–cut Diamond beam after 2 m of propagation through a plasma of number density $n_e = 10^{20}$ m^{-3}.

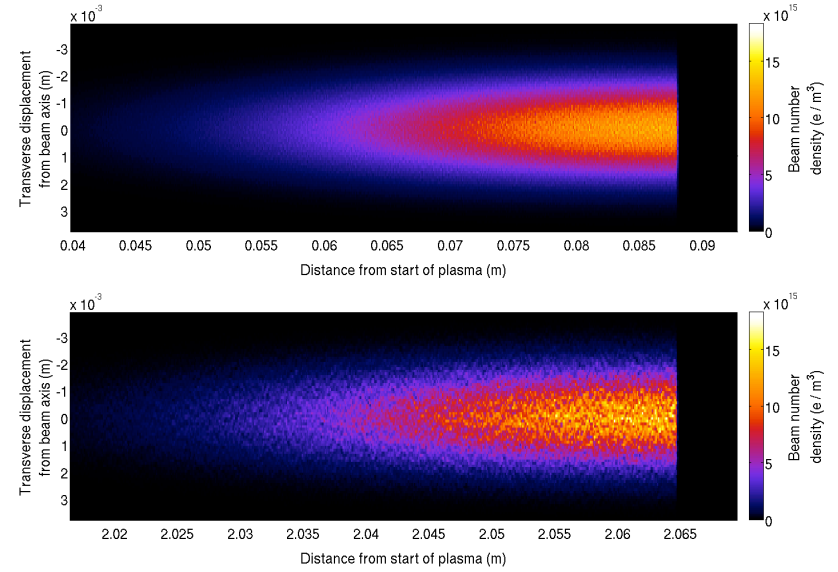

Figure 4.9.: The half–cut Diamond beam before (top pane) and after (bottom pane) 2 m of propagation through plasma of density $n_e = 10^{20}$ m^{-3}.

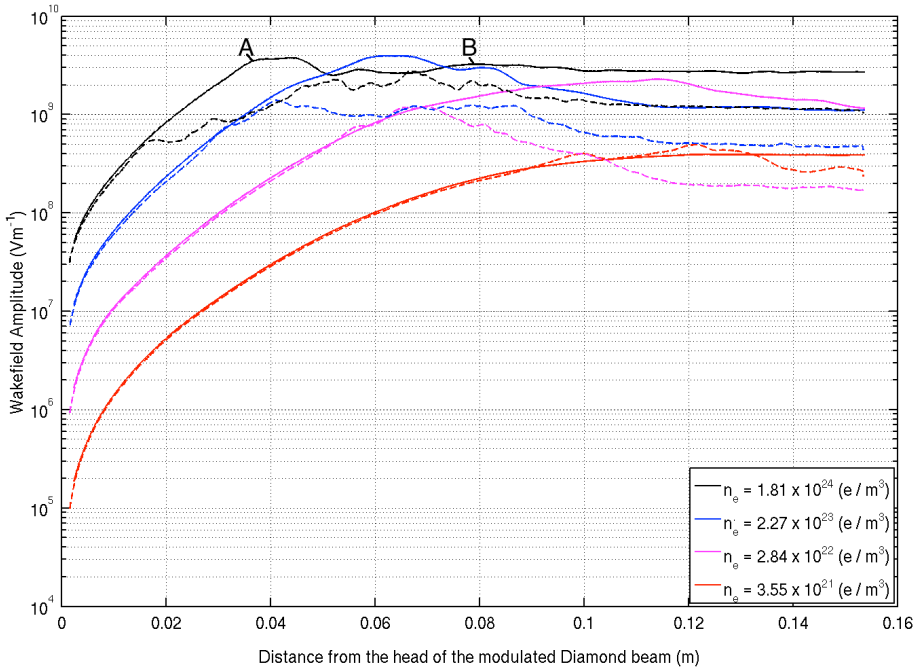

Figure 4.10.: The amplitude of the wakefield driven across the length of the Diamond micro–bunch train by the micro–bunched Diamond beam for four hydrogen plasma densities (dashed line) and for four caesium plasma densities (solid line). These four densities were chosen from a parameter scan of eleven as they show the transition into the ion motion regime.

4.2. The Micro–Bunched Diamond Beam

Particle and laser beams longitudinally micro–bunched at the plasma wavelength are effective wakefield drivers. Each micro–bunch is short compared to the plasma wavelength and efficiently couples energy from the beam into the plasma. A micro–bunch train, with micro–bunches evenly spaced at the plasma wavelength, will resonantly excite the wakefield to high amplitudes. This section starts by investigating the amplitude of the wakefield driven by a micro–bunched Diamond beam matched to various plasma densities. Then a scheme to rapidly micro–bunch the Diamond beam by co–propagating it with a high amplitude wakefield is devised. Optimisation of the scheme then leads to a start–to–finish simulation of a novel two plasma stage beam line where the Diamond beam is micro–bunched by a high amplitude laser driven wakefield in a short plasma stage before going on to drive a particle–driven wakefield in a second, longer plasma stage.

Grid	Value	Beam	Value	Plasma	Value
n_z	150	*species*	e^-	*species*	H^+
n_y	150	E (GeV)	3	n_e (m^{-3})	$0.278 \times 10^{20} \times 2^j$
grid length (m)	2 λ_p	N	1.25×10^{10}	j	5 : 15
grid width (m)	2 λ_p	ϵ (nm rad)	140		
t_{end} (s)	6 σ_z/c				
ppc	6				

Table 4.4.: Micro–Bunched Diamond beam density scan parameters. j is the parameter being scanned over and other parameters are as defined in table 4.2

4.2.1. Modelling the Micro–Bunched Diamond Beam

A scan over plasma density was designed to identify the density at which the largest amplitude wakefield could be driven by the micro–bunched Diamond beam without ion motion disrupting the wakefield. To model a micro–bunched beam a bi–Gaussian envelope was assumed with a sinusoidal modulation along its length, described by equation 4.2,

$$n_b(z,x) = \frac{N}{(2\pi)^{3/2}\sigma_z\sigma_x^2} e^{-z^2/2\sigma_z^2} e^{-x^2/2\sigma_x^2} (1-\cos(k_p z)/2). \tag{4.2}$$

Where $n_b(z,x)$ is the beam number density and other parameters have their usual meaning. The initial density scan was performed over a hydrogen plasma, parameters summarised in table 4.4. The wakefield amplitude as a function of distance from the head of the Diamond beam (defined here as +3 σ_z from the centre of the Gaussian) is plotted in figure 4.10. The amplitude of the wakefield increases with distance from the head of the train of micro–bunches as the bunches constructively excite the wakefield. This continues until the plasma ions move from their initial positions, which acts to disrupt the wakefield.

Label A on figure 4.10 shows the point at which ion motion starts to disrupt the wakefield for the highest plasma number density simulation. The ion number density and electric field of this simulation are plotted on the top left and bottom

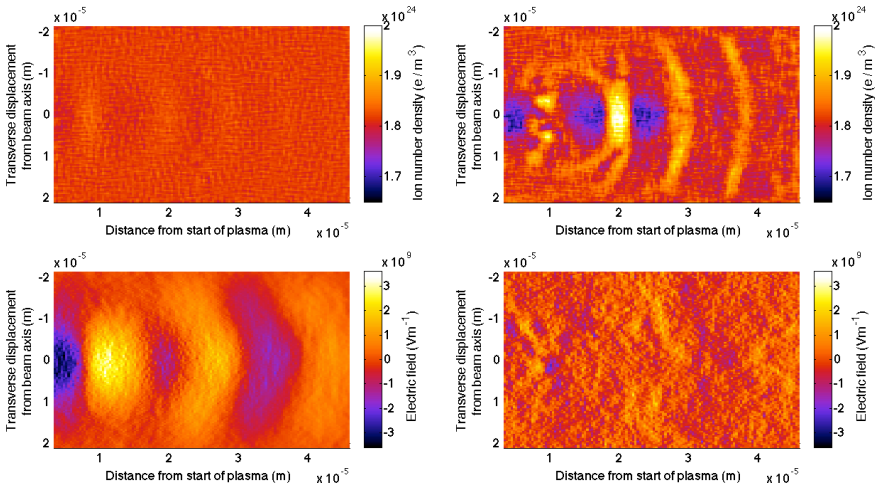

Figure 4.11.: The electric field excited by the micro–bunched Diamond beam in a caesium plasma of density $n_e = 1.84 \times 10^{24}$ m^{-3}, 37 mm from the head of the beam (bottom left pane) and 91 mm from the head of the beam (bottom right pane). The caesium ion number densities at these points are plotted in the panes above.

left panes of figure 4.11 respectively. The ion number density has subtle peaks and troughs along the direction of propagation. The electric field excited has distinct accelerating and decelerating regions, although not of a classic wakefield such as that in figure 4.6. Label B on figure 4.10 is at a later time in the same simulation where significant ion motion has occurred, the ion number density and electric field are plotted on the top right and bottom right panes of figure 4.11 respectively. Note that the distribution of ions has evolved to include sharp peaks and troughs as well as regions of undisturbed ions. The electric field excited in such a plasma may have high amplitude regions, as shown in the bottom right pane, but their distribution is chaotic with no periodic well defined accelerating regions in which to accelerate a witness beam. Therefore ion motion constrains the plasma densities in which a high amplitude wakefield can be driven by the micro–bunched Diamond beam.

One way of mitigating ion motion is to decrease the charge–to–mass ratio of the ion, i.e. to move to heavier singularly ionised elements. As such the density scan was performed with the same parameters found in table 4.4, but over a singularly ionised caesium plasma.

Figure 4.10 shows the maximum possible wakefield the micro–bunched Diamond beam can drive in a caesium plasma is 4 GVm^{-1}; above this the wakefield is disrupted

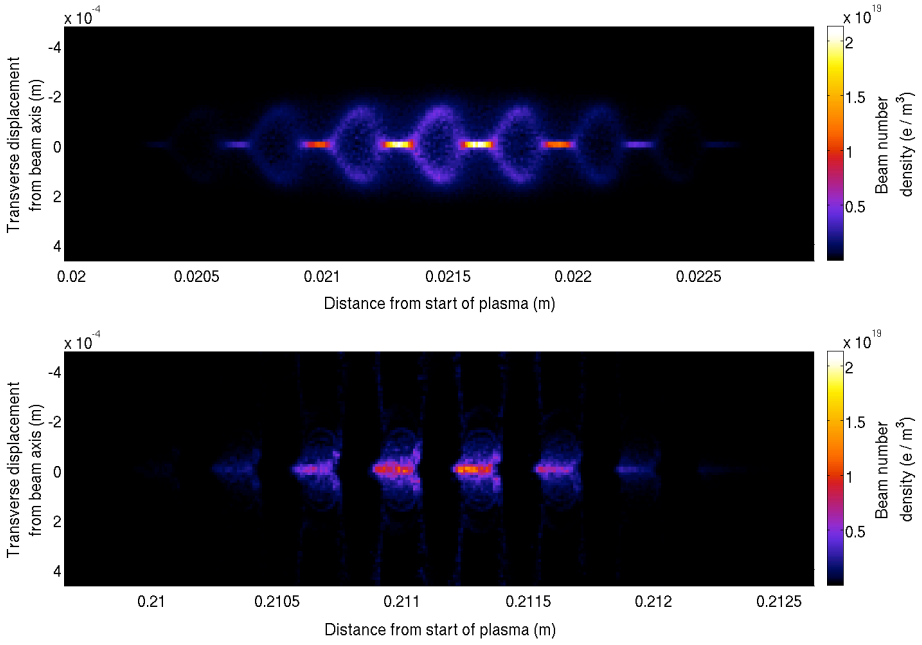

Figure 4.12.: Micro–bunching of the short Diamond beam via co–propagation with a $E_r = 1$ GVm^{-1} wakefield. The top pane shows the short Diamond beam at the point where the micro–bunches have fully formed $L = 20$ mm, and the bottom pane shows the diverging micro–bunches at $L = 200$ mm.

by the motion of the background plasma ions motion. The density scan identified the density of interest $n_e = 2.8 \times 10^{22}$ m^{-3}. At this density a high amplitude wakefield is driven along the length of the Diamond beam peaking at 2 GVm^{-1}, 0.062 mm behind the centre of the Diamond beam. 74.7% of the charge of the Diamond beam experiences a wakefield of $E_z > 1$ GVm^{-1}.

4.2.2. Single Stage Design

A charged particle beam can be micro–bunched at the plasma wavelength by co–propagating it with a high amplitude wakefield. The transverse fields of a wakefield form alternating focusing and defocusing regions which the beam particles experience. The particles in the focusing region are focused on–axis forming evenly spaced micro–bunches. Those in the defocusing regions are defocused as a result of the transverse momentum imparted and leave the wakefield. The resulting micro–bunch train is a highly effective wakefield driver.

An ultra–short laser pulse can be used to drive the micro–bunching wakefield as only a short co–propagation distance is needed between the wakefield and particle beam to achieve micro–bunching of the beam. Resolving the laser wavelength within a particle–in–cell simulation requires approximately two orders of magnitude more computational resources to compute at the densities being simulated[2]. As such, a way to model the laser pulse was required.

A simulation was performed using an ultra–short electron beam that drove a $E_r = 1$ GVm^{-1} wakefield, modelling the laser pulse, as a computational save. This ultra–short electron beam led the core of the Diamond beam by $+1$ σ_z, driving a wakefield in the plasma which co–propagates with the trailing Diamond beam. The electron beam driven wakefield neglects effects, a significant one being slippage between the wakefield and witness Diamond beam, as a laser driven wakefield typically propagates slower than particle driven wakefield. Furthermore the electron driver does not evolve significantly over the propagation distance whereas a laser pulse would experience self focusing, diffraction and beam head erosion effects. As a first iteration of simulations however, the electron driven wakefield approximation was suitable for initial investigations.

Further computational savings were needed to simulate the interaction of the Diamond beam with the wakefield over long distances. As the point of the simulation was to investigate the micro–bunching effect of a wakefield on the Diamond beam, the whole length of the Diamond beam need not be simulated, so a shorter Diamond beam of $\sigma_z = 0.6$ mm was used.

The top pane of figure 4.12 shows the Diamond beam forming micro–bunches at a distance of 20 mm into the plasma, and then the micro–bunches again at 200 mm (The plasma length of 200 mm is significantly shorter than the minimal defacing length of 1330 m calculated in section 2.2.2). The micro–bunches are spaced λ_p apart, crucial in allowing them to successively excite a wakefield. Furthermore, the peak number density of the central micro–bunch is $n_b = 2 \times 10^{19}$ m^{-3}, an increase by a factor of 5 from the peak number density of the centre of the baseline Diamond beam, due to radial compression from the focusing fields of the wakefield. When modelling the Diamond beam in subsection 4.2.1 radial compression of the micro–bunches was not considered. Given the enhanced driving capabilities of radially compressed

[2]This is due to the smallest structure that needs to be resolved becomes the laser wavelength, $\lambda = 1$ μm, instead of the plasma wavelength of $\lambda_p \approx 100$ μm.

beams, the micro–bunch train achieved here could drive a higher amplitude wakefield than the maximum $E_z = 4$ GVm^{-1} achieved in figure 4.10.

The on–axis number density of the central micro–bunch decreases from its peak of 2.07×10^{19} m^{-3} at the 20 mm focus to 1.28×10^{19} m^{-3} at 200 mm. This is due to the beam electrons in the focusing regions overshooting the axis, having sufficient transverse momentum to escape the wakefield. The micro–bunches continually leak charge, degrading the wakefield driving capability of the micro–bunch train. Co–propagating the Diamond beam with a high amplitude wakefield for extended propagation distances achieves micro–bunching of the Diamond beam, but the micro–bunches have a too high a divergence for the transverse electric fields of the wakefield to contain. This limits the effectiveness of the single–stage design for driving stable wakefields over long distances.

4.2.3. Two Stage Design

Lower divergence micro–bunches can be attained by only briefly exposing the beam electrons to the focusing fields of the wakefield. Then, by allowing the beam to propagate through vacuum, the micro–bunches form as the transverse momentum imparted causes the beam electrons to drift on axis. To achieve this the single plasma stage was split into two stages. The first being short, wherein the Diamond beam co–propagates with the laser–driven wakefield and the second being longer, where the now micro–bunched Diamond beam drives a higher amplitude wakefield of its own. The added advantage of such a scheme is that the laser pulse can be steered onto the axis of propagation of the Diamond beam with a mirror (with a hole allowing the Diamond beam to propagate through unperturbed) before the first stage, and discarded similarly after the first stage, once its laser–driven wakefield has been utilised.

The distance from the start of the first stage to the point at which on–axis number density of the forming micro–bunches is maximised is said to be the ‘focal point’ of the first stage. A simulation set scanning over plasma stage length was designed to identify the co–propagation length needed between the Diamond beam and a wakefield that achieves micro–bunching of the beam whilst minimising the divergence of the micro–bunches, parameters found in table 4.5. For this scan a $E = 300$ MeV Diamond beam was used to further save on runtime.

Grid	Value	Beam	Value	Plasma	Value
n_z	600	*species*	e^-	*species*	Cs^+
n_y	180	E (GeV)	0.3	n_e (m^{-3})	1.11×10^{22}
grid length (m)	10 λ_p	N	1.25×10^{10}		
grid width (m)	3 λ_p	ϵ (nm rad)	140		
t_{end} (ns)	0.6				
ppc	6				

Table 4.5.: Plasma stage length scan parameters. Parameters as defined in table 4.2.

Stage Length (mm)	Focal Point (mm)	n_b at 200 mm (m^{-3})
∞	N/A	1.30×10^{19}
2.5	65.5	4.09×10^{19}
3.0	57.0	4.00×10^{19}
3.5	48.5	3.90×10^{19}
4.0	42.0	3.73×10^{19}
4.5	37.5	3.80×10^{19}
4.0	32.0	3.64×10^{19}

Table 4.6.: The focal points of the Diamond beam micro–bunches for various plasma stage lengths and their peak on–axis number density after a total propagation length of 200 *mm*.

Once the focal points of various stage lengths were identified the simulations were re–ran with a second plasma stage added at these focal points. Table 4.6 summarises the geometries of the two–stage simulations and the on–axis number density of the micro–bunches after 200 mm of propagation through the beam lines. Note that the longer stages have shorter focal lengths, focusing the micro–bunches harder but resulting in less charge remaining on–axis at 200 mm of total propagation.

Figure 4.13 shows the micro–bunch train at focus ($L = 63$ mm) for a plasma stage length of 2.5 mm and then again at propagation distance $L = 200$ mm. The on–axis number density of the micro–bunch train at focus is $n_e = 2.82 \times 10^{19}$ m^{-3}

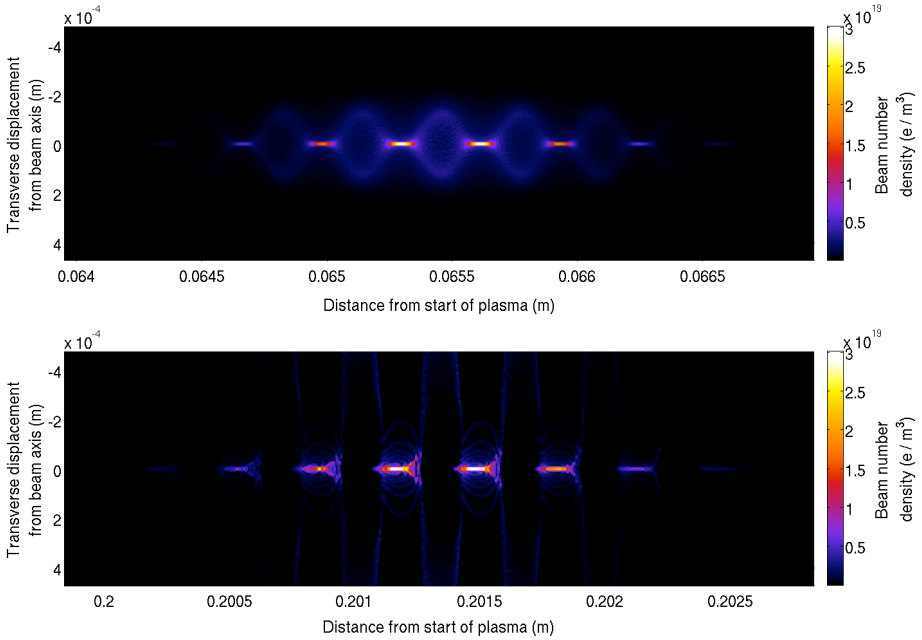

Figure 4.13.: Micro–bunching of the short Diamond beam via co–propagation with a $E_r = 1$ GVm^{-1} wakefield. The top pane shows the short Diamond beam at the point where the micro–bunches have fully formed $L = 63$ mm, and the bottom pane shows the stable micro–bunches at $L = 200$ mm, after 137 mm of further propagation through the second plasma.

and actually increases to $n_e = 4.09 \times 10^{19}$ m^{-3} at 200 mm, demonstrating that the two stage design leads to low divergence, stable[3] micro–bunches.

The first plasma stage length of $L_{1st} = 14$ mm was chosen as it produces a micro–bunch train of sufficient quality and is short enough such that a laser–driven wakefield of $E_r = 1$ GVm^{-1} can be driven over its length before divergence of the laser pulse diminishes the micro–bunching wakefield.

4.2.4. Laser–Driven Micro–Bunching Wakefield

Section 4.2.3 above details how an electron–driven wakefield can be used to micro–bunch the Diamond beam. This section is concerned with finding the parameters of an ultra–short laser pulse that can drive such a wakefield, as the electron beam used previously would require unfeasible amounts of space and expense to generate.

[3]Stable over the lengths relevant to the experimental proposal.

Laser	Parameter
E (J)	0.5
σ_t (fs)	50
σ_r (μm)	$\sqrt{2}/k_p$
λ_0 (μm)	1.06
P (TW)	10

Table 4.7.: Laser parameters. Where E is the laser pulse energy, σ_t is the beam length, σ_r the beam width, λ_0 is the laser wavelength and P is the laser's peak power.

The critical power for a laser pulse of $\lambda = 1$ μm to self focus in a plasma of density $n_e = 2.8 \times 10^{22}$ m^{-3} is $P_c = 648$ TW, given by equation 2.24. Given the short laser pulse requirement of $\sigma_z = 1/k_p$ this means the energy of the pulse must exceed $E = 32.5$ J in order to self focus. Such an ultra–short near peta–watt laser system would be a bespoke design at the cutting edge of laser technology, a prohibitively expensive piece of equipment. Self focusing, however, is not required to maintain a significant wakefield over the $L_{1st} = 14$ mm of plasma in the first stage. By increasing the laser's focal spot radius the Rayleigh length will be increased, maintaining the pulses (albeit lower) intensity over more of the plasma stage. Furthermore positioning the laser's focal spot half way into the first stage instead of at the first stage entrance maximises the amplitude of the wakefield driven throughout the stage. If a sufficient wakefield can be driven without requiring the laser pulse to self focus, then the requirements of the laser parameters will be relaxed, leading to a lower cost laser system.

Figure 4.14 shows the amplitudes of the radial and longitudinal wakefields driven by laser pulses of $E = 1$ J, $E = 0.5$ J and $E = 0.2$ J, parameters found in table 4.8. The laser pulse length and width were chosen to match the plasma such that $\sigma_z = \sigma_r = \sqrt{2}/k_p$. As such, the higher plasma density simulations had shorter, more tightly focused laser pulses, enhancing their intensity. At densities of $n_e = 5 \times 10^{22}$ m^{-3} and above the laser pulses drive a non–linear wakefield, resulting in the breaking of the linear relationship between number density and electric field amplitude. From these simulations a parameter set for a suitable laser pulse was found, summarised in table 4.7, capable of driving a wakefield of $E_r = 0.8$ GVm^{-1} at focus without entering the self–focusing regime.

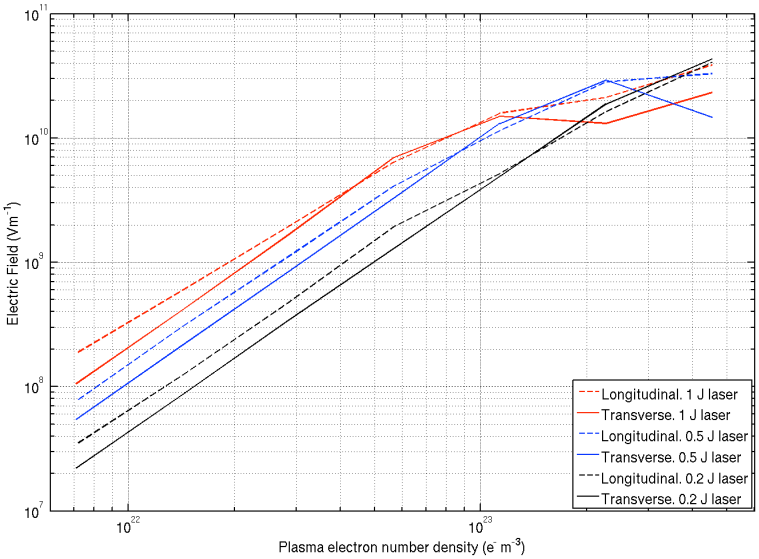

Figure 4.14.: The amplitudes of transverse (solid lines) and longitudinal (dashed lines) wakefields driven by laser pulses of $E = 0.2$ J, $E = 0.5$ J and $E = 1$ J for a range of plasma densities.

Grid	Value	Laser	Value	Plasma	Value
n_z	$(\lambda_p/\lambda_l) \times 90$	E (J)	$0.2, 0.5, 1$	*species*	Cs^+
n_x	120	τ (fs)	50	n_e (m^{-3})	$0.278 \times 10^{20} \times 2^j$
grid length (m)	4 λ_p	σ_r (m)	$\sqrt{2}/k_p$	j	8:14
grid width (m)	3 λ_p	λ_0 (μm)	1.06		
t_{end} (s)	$(\lambda_p \times 4)/c$				
ppc	6				

Table 4.8.: Laser energy and density scan parameters. Parameters as defined in tables 4.2 and 4.7.

The laser pulse surmised in table 4.7 propagating through a plasma of density $n_e = 2.8 \times 10^{22}$ m^{-3} has a dephasing length of 8 m (given by equation 2.17). The pulse has 0.5 J giving a depletion length of 1.2 m (given by equation 2.20). Both of these lengths are greater than the first plasma stage length of 14 mm and the laser pulse is deemed suitable for driving a wakefield to micro–bunch the Diamond beam. Such a laser system is commercially available. The AVET Ti:S Femtosecond TW System [70] delivers a $E = 0.5$ J, $\tau < 45$ (fs) pulse at a wavelength of $\lambda_0 = 800$ nm

Grid	Value	Laser	Value	Plasma	Value
n_z	$1,200,000$	E (J)	0.5	n_e (m^{-3})	2.84×10^{22}
n_x	78	σ_t (fs)	50	*species*	Cs^+
grid length (m)	0.040	σ_r (m)	$3 \times \sqrt{2}/k_p$	L_{1st} (mm)	1
grid width (m)	$2.6 \times \lambda_p$	λ_0 (μm)	1.06	L_{vac} (mm)	120
t_{end} (s)	1.3×10^{-10}	P (TW)	10	L_{2st} (mm)	380
cores	4096				
runtime (*hours*)	240				

Table 4.9.: Full final simulation parameters for the Diamond Booster electron beam. L_{1st} is the first plasma stage length, L_{vac} is the length between the first and second plasma stage and L_{2st} is the length of the second stage. Other parameters as defined in tables 4.2 and 4.7.

with a footprint of $4000 \times 1200 \times 220$ mm^3. Such a system meets the requirements of the experiment as well as being economically feasible.

4.3. Fully Inclusive Diamond Beam Simulation

Given the optimisation study detailed thus far, a two stage conceptual beam line was designed as shown in figure 4.15. The ultra–short laser pulse detailed in table 4.7 is focused by an off–axis parabolic mirror (not shown) before being steered onto the Diamond beam's axis of propagation, leading the beam, via a turning mirror. The hole in the mirror allows the Diamond beam to propagate though unperturbed. The ensemble of laser pulse and particle beam then enter the first plasma stage where the laser–driven high amplitude wakefield imparts transverse momentum onto the Diamond beam. Upon exiting the first plasma stage the micro–bunches form, and the laser pulse defocuses, allowing the bulk of the pulse to be steered away via a second turning mirror with a hole (not shown in figure 4.15). The micro–bunched Diamond beam then enters the second plasma stage where the focusing fields in this purely particle–driven wakefield stage are sufficient to keep the micro–bunches contained. A start–to–finish high resolution simulation was performed, parameters found in tables 4.9 and 4.1.

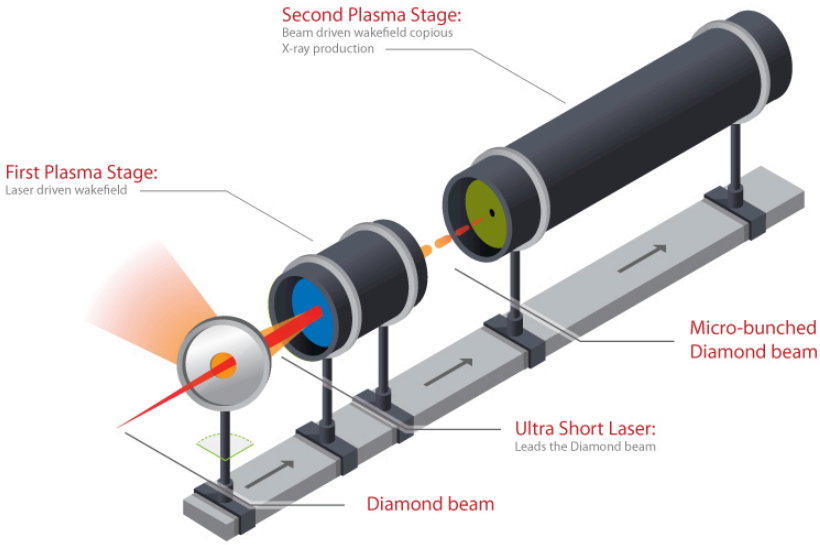

Figure 4.15.: A conceptual design of the two plasma stage design. An ultra short laser pulse drives a high amplitude wakefield in the first, short stage that exposes the Diamond beam to alternating focusing and defocusing fields along its length. The Diamond beam forms into micro–bunches between the two stages. Upon entering the second stage the micro–bunched Diamond beam constructively drives a 4 GVm^{-1} wakefield. This wakefield provides the focusing fields that stimulate whole micro–bunch oscillations leading to copious X–ray emission.

The fully inclusive simulation required resolving of the laser wavelength to capture the physics that the previous simulations have neglected, such as beam head erosion, diffraction and photon acceleration effects. As such the grid size needed was 1,200,000 $\times$ 72. This simulation required a dedicated high performance computer to run. 2.5 million core hours were awarded to run on the DiRAC high performance computer[4]. Estimations taking into account how well EPOCH scales with large numbers of cores approximated that with this number of core hours the full 2 m of beam line would not be able to be simulated. As such two major computational saving techniques were devised.

[4]This research made use of the DiRAC@durham.ac.uk HPC cluster. DiRAC is the UK HPC facility for particle physics, astrophysics and cosmology and is supported by STFC and BIS. We acknowledge technical support from Lydia Heck, a member of the DiRAC HPC facility programming team.

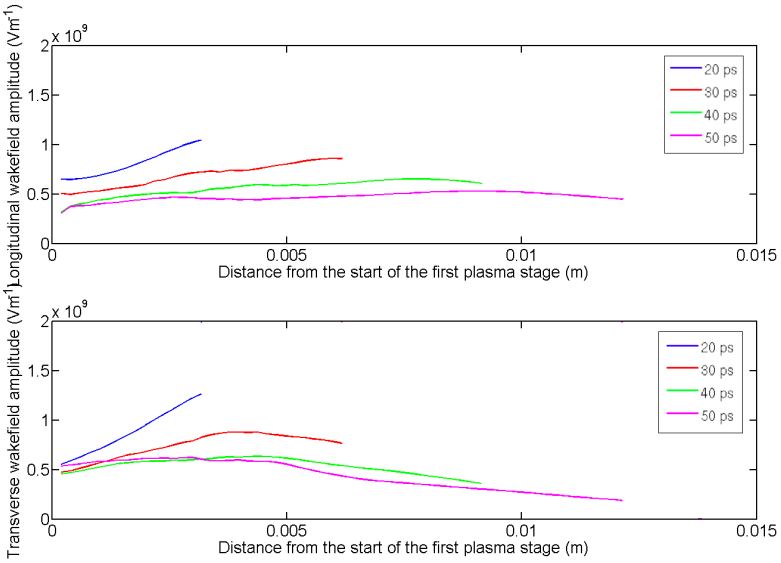

Figure 4.16.: The amplitude of the wakefield (longitudinal electric field in the top pane, transverse electric field in the bottom pane) driven by the ultra–short laser pulse at 10 ps snapshots throughout the first plasma stage (parameters found in 4.9).

The first saving measure involved running the simulation at a high enough resolution to resolve the laser wavelength, with the 1,200,000 × 72 grid size, from the start of the simulation until the laser beam propagated through the first plasma stage. At this point, the simulation would be terminated and a 'restart' time step recorded. The data sets within this restart time step were binned down to a much smaller grid size of 6000 × 72 (a factor of 200 reduction) using a custom program and used to create a new restart time step. The simulation was then restarted from this time step and the vacuum and second plasma stage interactions simulated.

The second computational save was necessary to capture the geometry of the beam line and involved overcoming a limit of the EPOCH code. EPOCH only allows laser pulses to be injected on the boundary of a simulation grid, whilst particle beams can only be initialised within the grid. This means that the laser pulse could not lead the beam. To overcome this the particle pusher of EPOCH was modified to generate new particles on the boundary of the grid with a specified momentum, temperature and density profile until a specified time step by an EPOCH developer C. Brady. Further modifications were introduced by myself to the particle–pusher, the initial positions of the boundary–pushed particles were randomised within the boundary cells, solving the problem of unphysical beam profiles. This allowed not only the

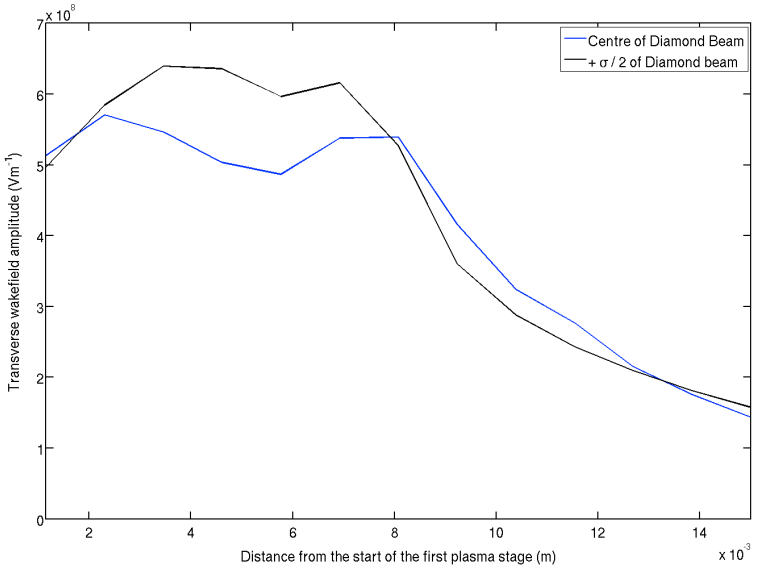

Figure 4.17.: The amplitude of the focusing electric field experienced by the centre of the Diamond beam (blue line) and the beam electrons at $+\sigma_z/2$ (black line) throughout the first plasma stage. This demonstrates that different parts of the Diamond beam experience different integrated focusing fields, therefore forming micro–bunches at different distances from the first plasma stage.

laser pulse to lead the beam, but also took away the necessity of having additional vacuum before the first plasma stage where the beam would first be generated before proceeding to the plasma. This brought the total propagation distance needing the 1,200,000 $\times$ 72 grid from 2052 mm (2 m and the $2 \times \sigma_z$ before the first plasma stage) down to 40 mm.

The laser pulse is at focus half way through the plasma first stage (7 mm). As the pulse comes to focus, its intensity increases, driving a higher amplitude wakefield. As such, the wakefield amplitude varies with position throughout the plasma stage. Furthermore, a wakefield's amplitude diminishes the further behind the driving pulse (as energy is transferred from the wakefield to the witness beam, and dissipates as heat), meaning a wakefield's amplitude also varies with time. Figure 4.16 shows the amplitude of the transverse wakefields driven by the laser pulse in the high resolution simulation at 10 ps snapshots. Note that Diamond beam electrons just behind the laser pulse experience a $E_z = 1$ GVm^{-1} to $E_z = 0.4$ GVm^{-1} wakefield as they traverse the plasma stage, whereas beam electrons further behind will sample a more consistent wakefield of $E_z = 0.4$ GVm^{-1}. This means that different sections

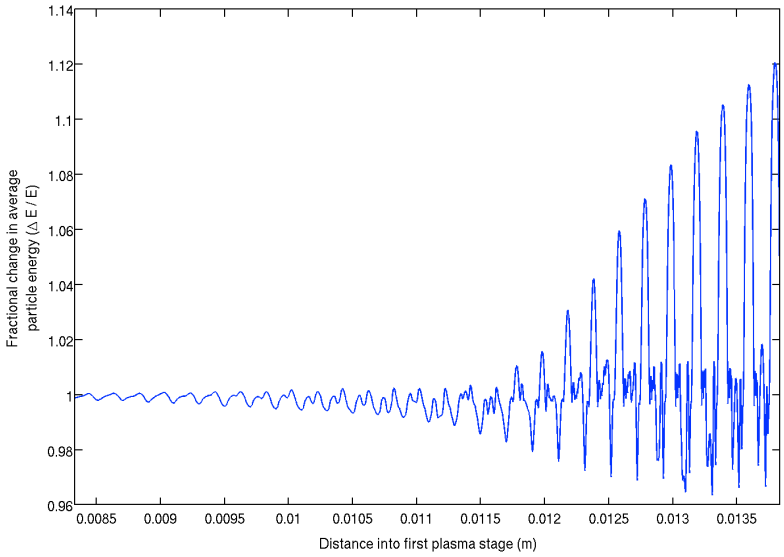

Figure 4.18.: The fractional energy change of particles within the Diamond beam along the direction of propagation. The wakefield imparts an energy spread — or chirp — on each of the micro–bunches, with the head of each micro–bunch being lower energy than the tail. Magnetic chicanes can be used to utilise this chirp to longitudinally compress the micro–bunches.

of the beam experience varying strength focusing fields — a result not captured with the electron–driven model used in the previous plasma stage parameter scans. These different regions of the Diamond beam will then have different focal points at which they form micro–bunches. It was necessary then to investigate this effect in order to optimally place the second plasma stage such that the central high–charge micro–bunches of the Diamond beam would be focused onto the entrance of the second stage.

Figure 4.17 shows the amplitude of the longitudinal and transverse wakefield sampled by the electrons at the centre and at $+\sigma_z/2$ of the Diamond beam. The focal points for these two regions were found to be $L_0 = 21$ mm and $L_{+\sigma_z/2} = 20.8$ mm. Given the small difference between these focal points, and the fact that 38% of the charge in the Diamond beam lies within $\pm\sigma_z/2$, the second stage was positioned 21 mm after the end of the first stage in order to capture the optimal amount of micro–bunched charge.

Figure 4.18 shows the longitudinal energy spread imparted on the Diamond beam by the longitudinal wakefield shown in figure 4.17. This energy spread, also known

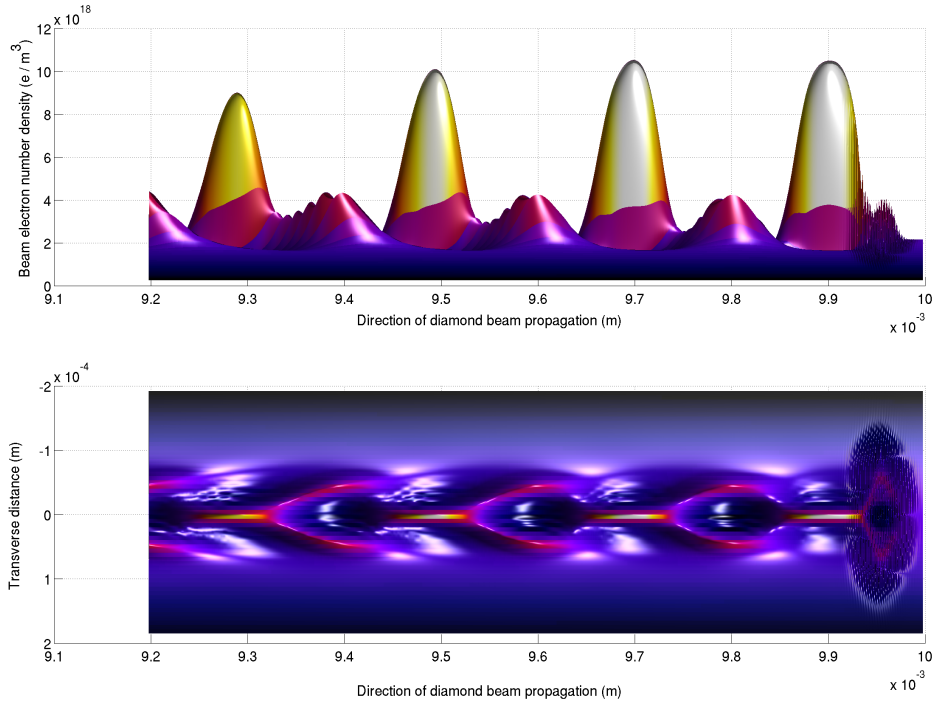

Figure 4.19.: The micro–bunched Diamond beam as it enters the second plasma stage. Electrons in focusing regions have formed the micro–bunches whilst electrons in the defocusing regions are transversely expelled (circular formations in the bottom pane).

as the chirp, can be used to compress these micro–bunches longitudinally via a conventional chicane. This opens up the possibility of a more complex future beam line design incorporating a chicane between the first and second stages. If compressed in this way, the micro–bunches would retain their spacing whilst having a greater peak number density.

Figure 4.19 shows the head of the Diamond beam at focus, from the fully inclusive simulation described in table 4.9, demonstrating the laser–driven wakefield successfully micro–bunching the Diamond beam. The top pane shows the steep leading edges of the micro–bunches, giving them a greater wakefield driving ability than those modelled by Gaussian profiles in the ideal compression simulations and those modelled by a sinusoidal profile found in the micro–bunched density scan simulations. The micro–bunches are regularly spaced a plasma wavelength apart, satisfying the strict requirement allowing successive bunches to constructively excite a wakefield. Also they have enhanced on–axis number density as the charge has

been focused on–axis, further enhancing their wakefield driving ability. It is these micro–bunches that then undergo radial oscillations about the axis of propagation in the second plasma stage, leading to copious X–ray production, that is studied in the next chapter.

This fully inclusive simulation demonstrates that the Diamond beam can be micro–bunched at the plasma wavelength over centimetres of plasma using a commercially available laser system, producing a highly effective wakefield driver. The two–stage beam line that achieves this can be applied to other charged particle beams, micro–bunching them at arbitrary plasma wavelengths and allowing existing conventional particle beam facilities to perform plasma wakefield experiments without a significant rehaul of their infrastructure or at great cost.

4.4. Micro–bunching the Diamond Storage Ring Beam

The two–stage micro–bunching technique has been applied to the electron beam of the Diamond booster synchrotron via simulation in the previous section. The electron beam found in the storage ring of the Diamond Light Source is shorter and has significantly lower emittance than that of the Diamond Booster electron beam. Both of these improvements are beneficial to generating more stable micro–bunches via the two–stage method. Lower emittance allows the micro–bunches to stay formed for longer and same amount of charge over a shorter beam allows fewer bunches to drive the same amplitude wakefield, leading to less dephasing between them.

In this section the two–stage micro–bunching technique is applied to the storage ring Diamond beam, parameters found in table 4.10, and the resulting wakefield driven in the second plasma stage detailed. It should be noted that the geometry of the two–stage beam line is the same for the Diamond Storage Ring electron beam. This is because the 'focusing length' of an electron beam by a wakefield lens is dictated primarily by the effective mass of the particle, that is to say the energy. Given the Storage Ring electron beam and Booster electron beam are $E = 3$ GeV in energy, there is no need to change the length of the first stage and position of the second. It should also be noted however, that lower emittance effects the

Grid	Value	Laser	Value	Plasma	Value
n_z	$360,000 \rightarrow 1800$	E (J)	0.5	n_e (m^{-3})	2.84×10^{22}
n_x	80	σ_t (fs)	50	*species*	Cs^+
length (m)	0.040	σ_r (m)	$3 \times \sqrt{2}/k_p$	L_{1st} (mm)	1
width (m)	$2 \times \lambda_p$	λ_0 (μm)	1.06	L_{vac} (mm)	114
t_{end} (s)	1.3×10^{-10}	P (TW)	10	L_{2st} (mm)	385
cores	400				
runtime (h)	48				

Table 4.10.: Parameters for the Diamond Storage Ring electron beam simulation. L_{1st} is the first plasma stage length, L_{vac} is the length between the first and second plasma stage and L_{2st} is the length of the second stage. n_x has two values as the simulation's grid is scaled down after the laser–plasma interaction has ended for runtime purposes. Other parameters as defined in tables 4.2 and 4.7.

matched beam radius of the micro–bunches, $r_{bm} = (\epsilon_n/\gamma k_\beta)^{1/2}$ [71], where ϵ_n is the normalised beam emittance, γ is the Lorentz factor of the beam and k_β is the betatron wavenumber. The matched beam radius for the Storage Diamond Ring electron beam is then $r_{bm} = 0.4$ μm, which is two orders of magnitude smaller than the radius of the micro–bunches incident on the second plasma stage, r_i. This mismatch between the incident radius of the micro–bunches and the beam match radius is the source of the radial oscillations discussed in the next chapter. The micro–bunches' radii then oscillate between $r_b^2 = r_i^2$ and $r_b^2 = \epsilon^2/(\gamma^2 k_b^2 r_i^2) = r_{bm}^4/r_i^2$.

The form of the micro–bunched Diamond Storage Ring beam is shown in figure 4.20 as it enters the second plasma stage (top pane), 30 mm further into the stage where the micro–bunch number density maximises (middle pane) and 30 mm further still where the number density of the micro–bunches diminishes. The colour bar shows that the peak number density of the micro–bunches doubles from entering the second plasma stage to propagating 30 mm further into the stage. This is the effect of the strong transverse focusing fields of the self–driven wakefield compressing the micro–bunches. The electrons being discarded by the defocusing fields of the wakefield drive a strong wakefield as they leave the simulation box, seen in the middle pane of figure 4.21. This off–axis wakefield is π out of phase with the on–axis wakefield and will interfere with attempts to inject electrons into the main wakefield.

This off–axis wakefield is short lived however, and diminishes rapidly compared to the on–axis wakefield. If one choose an off–axis witness electron beam injection scheme then the natural point to do so would be at the entrance of the second plasma stage, where there is no off–axis wakefield to interfere as there is no plasma.

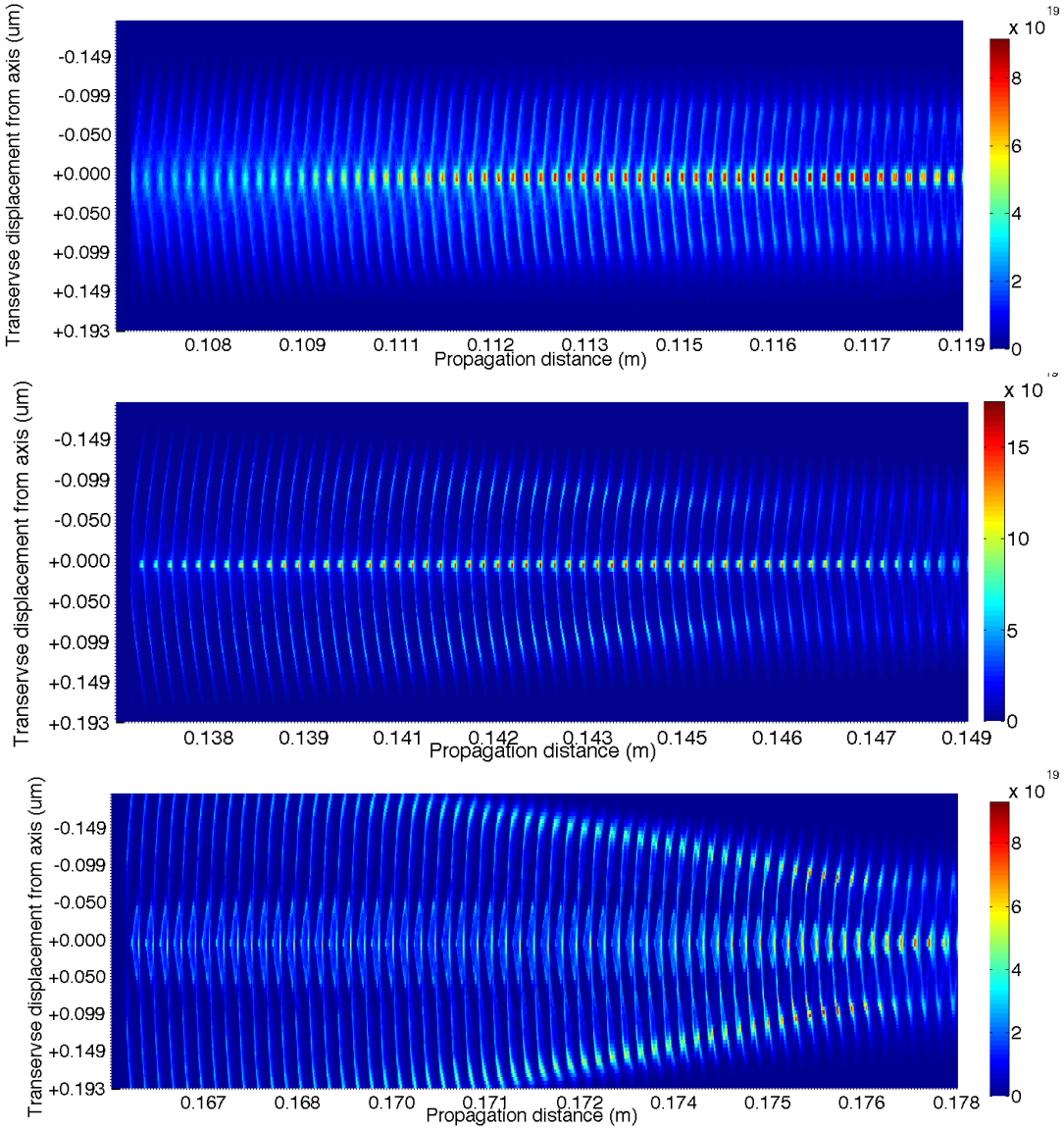

Figure 4.20.: The number density of the Diamond Storage Ring electron beam as it is entering the second plasma stage (top), as it is re-focused by the self-driven wakefield 30 mm later (middle panel) and 30 mm further as the number density of the micro–bunches begins to diminish.

Figure 4.21 shows the wakefields corresponding to figure 4.20. The wakefield peaks at $E = 1.1$ GVm^{-1}, 30 mm into the second plasma stage. The off–axis wakefield is

briefly comparable in magnitude to the on–axis wakefield 30 mm into the second stage before falling off at the discarded charge moves further from the axis of propagation.

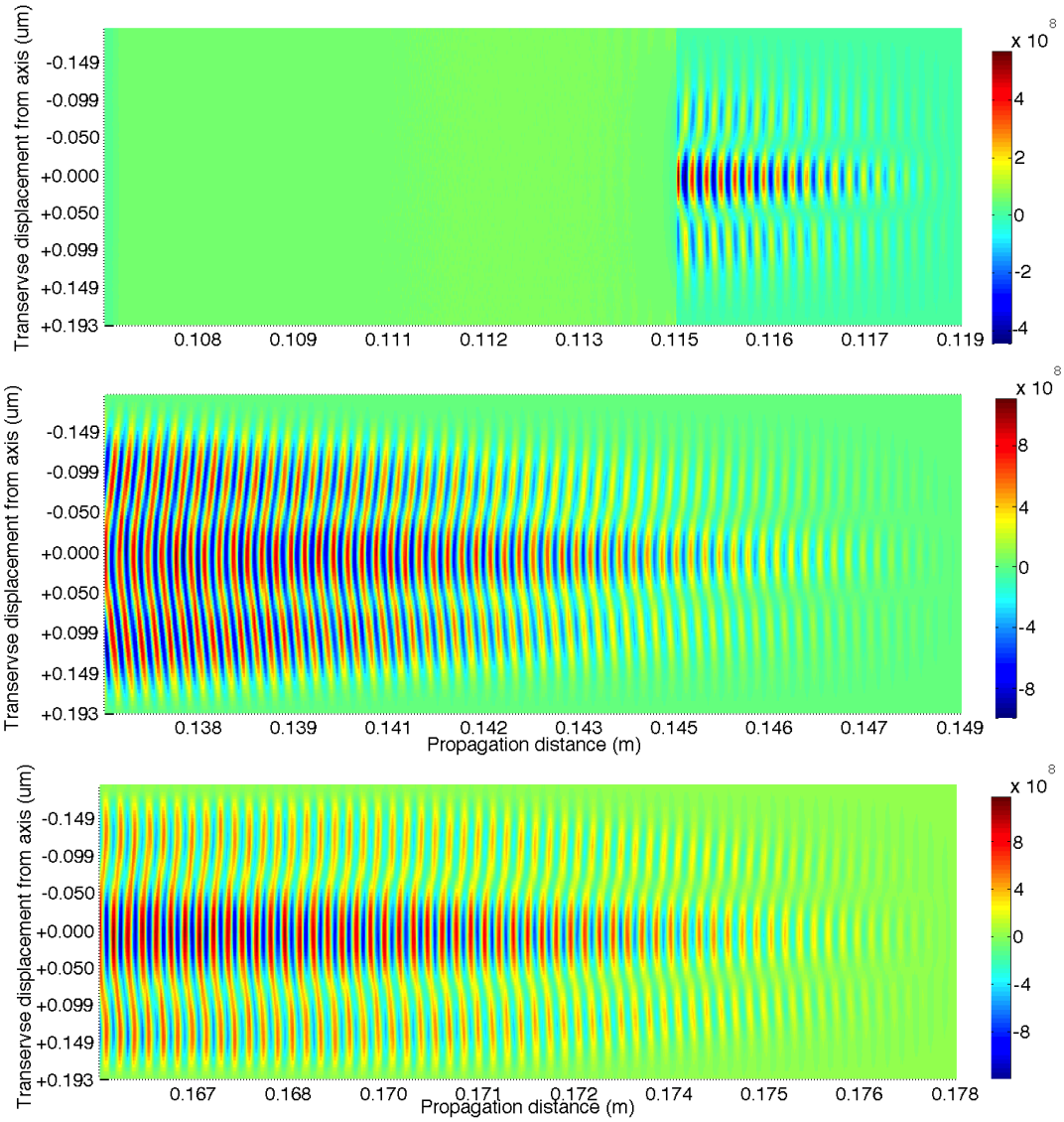

Figure 4.21.: The corresponding electric fields driven by the Micro–bunched Diamond storage beam in the above figure. The wakefield in the top pane begins at the start of the second plasma cell (115 mm). Note the short–lived off–axis π out of phase wakefield driven by the radially discarded beam electrons in the middle pane

Figure 4.22 shows the wakefield driven at the significantly longer distance of 380 mm into the second plasma stage. The top pane of figure 4.22 shows that the micro–bunches have grown transversely. The middle pane shows that the micro–bunches have a similar number density of $n_e = 1.3 \times 10^{19}$ m^{-3} along the length of the

micro–bunch train and the bottom pane shows wide wakefield of $E = 0.39$ GVm^{-1} being driven.

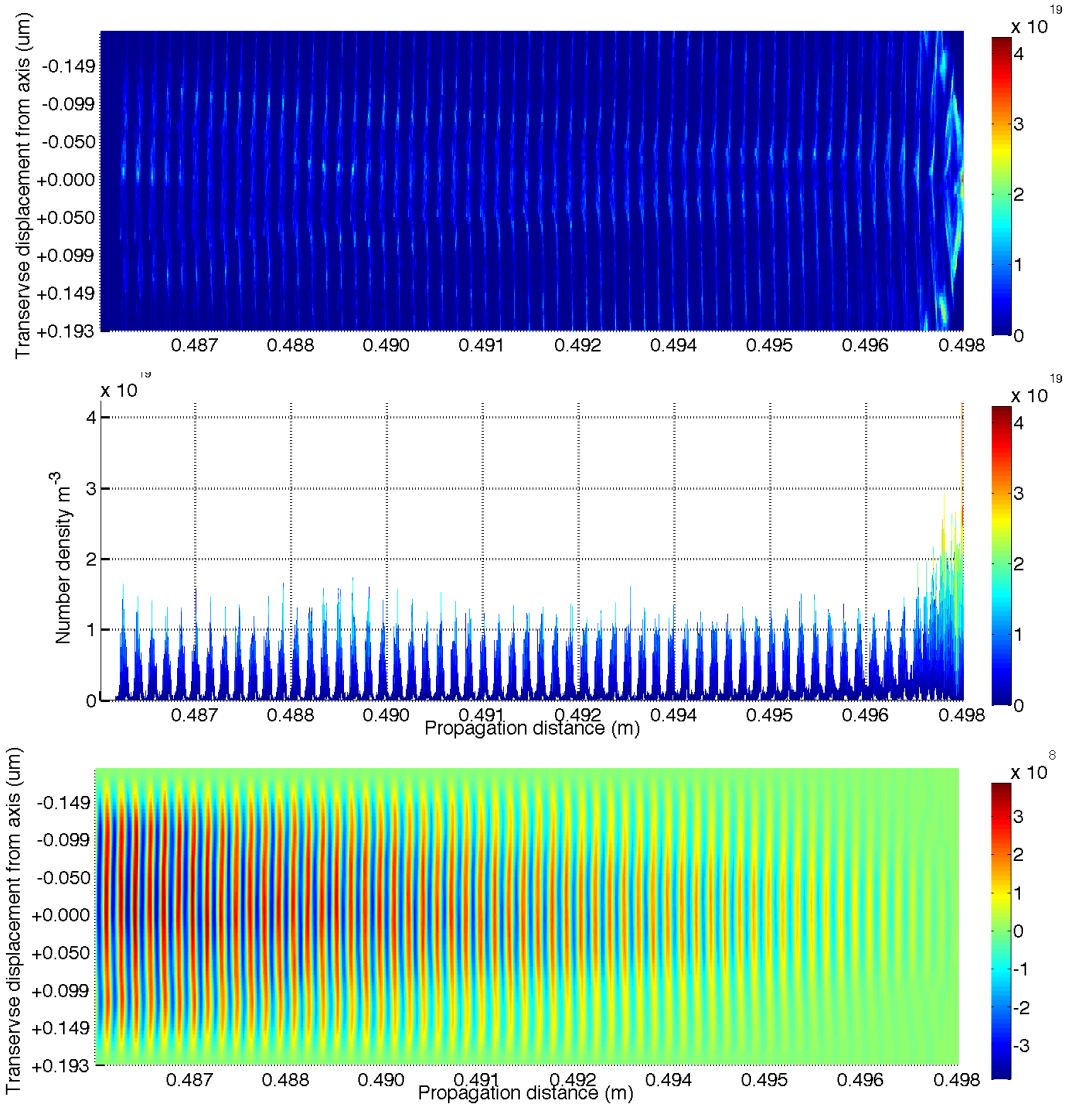

Figure 4.22.: The micro–bunch train at 380 mm into the second plasma stage. The micro–bunches are significantly wider and have a similar in peak number density of $n_e = 1.3 \times 10^{19}$ m^{-3}. The bottom pane shows the wakefield driven is also significantly wider than that driven at the beginning of the second plasma stage ($\simeq 2\lambda_p$).

Chapter 5.

X–ray Emissions of the Micro–bunched Diamond Beam within a Wakefield

It has been demonstrated, via extensive, full–scale two dimensional computer simulations, that it is possible to micro–bunch the 3 GeV Diamond beam using a novel wakefield accelerator design. The micro–bunches are maintained within their self–driven wakefield structure and undergo entire micro–bunch oscillations, generating brilliant, radially polarised, X–ray pulses. This chapter is concerned with examining the synchrotron radiation emitted by the micro–bunches as they propagate through the second plasma stage. The simulations presented demonstrate these X–ray pulses have orders of magnitude increases to key quantities, such as peak brightness and photon energy, that are produced without the long and expensive insertion devices used in conventional light source facilities.

Rather than the whole bunch oscillating in the same direction as in conventional undulators, the electron bunch repeatedly radially collapses on–axis producing radially polarised light instead of linearly polarised light, giving the X–ray pulses produced a unique property.

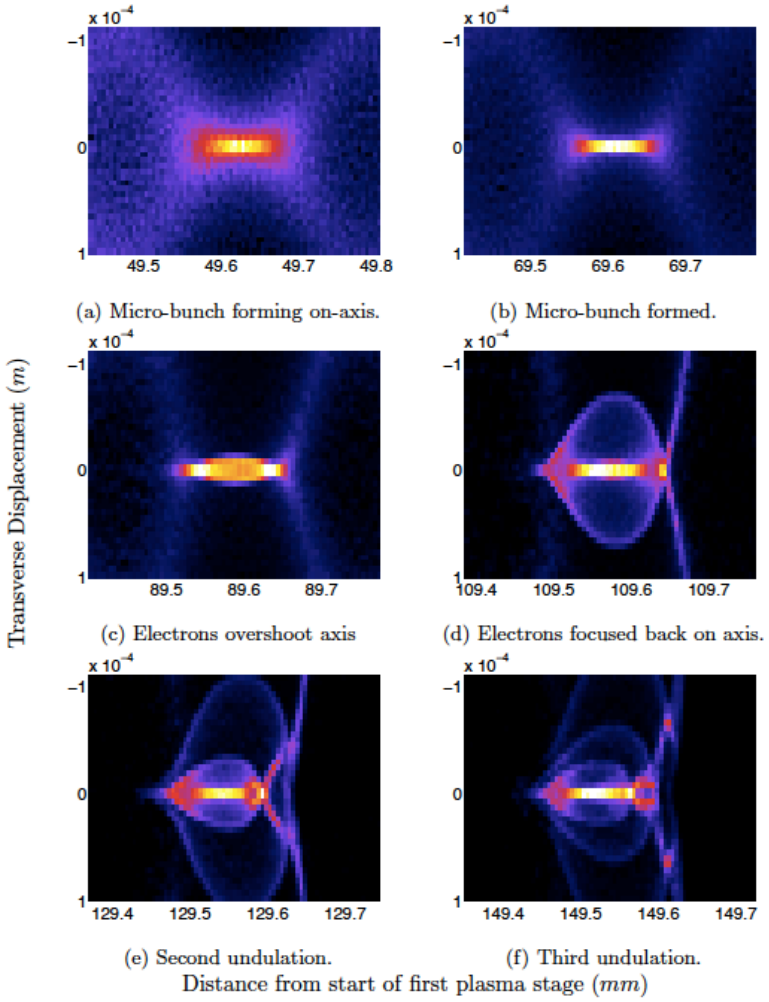

Figure 5.1.: Coherent oscillation of the simplified Diamond beam in the second plasma stage. The six panes show an individual micro–bunches number density in 20 mm intervals, progressing from pane a) to pane f).

5.1. Micro–bunch Radial Oscillations

Figure 5.1 shows a single micro–bunch undergoing such radial oscillations. The simulation presented in figure 5.1 is of the micro–bunched Diamond beam from section 4.2.3. The focusing fields of the wakefield bring the beam electrons on–axis as in pane a). The micro–bunch has maximum on–axis number density in pane b) and is regarded as formed. The electrons overshoot the axis in pane c). The bulk of the electrons are focused back on axis whilst some escape the focusing field in pane d). A second and third oscillation is seen in pane e) and pane f), again with a small amount of charge escaping the micro–bunch for each oscillation.

Beam	Value	Wakefield	Value
E (GeV)	3	E_{wake} (GVm^{-1})	1
$\Delta E/E$	0.01	V_{ph} (ms^{-1})	0.99999997 c
σ_z (μm)	38		
σ_r (μm)	38		
N_{part}	1000		

Table 5.1.: Diamond beam micro–bunch parameters for the RDTX simulation, where E is the electron energy, $\Delta E/E$ is the longitudinal energy spread, σ_z is the beam length, σ_r is the beam radius and N_{part} is the number of macro–particles. For the wakefield parameters, E_{wake} is the amplitude of the wakefield's electric field and V_{ph} is the phase velocity of the wakefield.

To examine the radial oscillations of the micro–bunches, parameters of a single micro–bunch were taken from the fully inclusive simulation as detailed in section 4.3 at the entry point to the second plasma stage, found in table 5.1. This bunch was then simulated using the code RDTX[1] co–propagating with a wakefield of amplitude $E_r = 1$ GVm^{-1} — the minimum amplitude of the wakefield experienced by 74.7% of the charge of the micro–bunched Diamond beam in the second plasma stage.

The top pane of figure 5.2 plots the transverse displacement of the 1000 simulated particles against time over a total propagation distance of 127 mm. It is seen in the top pane that the particles initially oscillate coherently about the axis of propagation, maintaining transverse coherence over several undulations before the small difference in oscillation frequency causes the electrons to dephase.

This is in part[2] due to the electrons at the centre of the micro–bunch experiencing the strongest focusing fields of the wakefield (as the micro–bunch is centred about the wakefield) and therefore having a higher oscillation frequency than those at the head

[1] RDTX is described in section 3.2.

[2] The transverse electric field profile of a wakefield in the linear regime is approximated by a parabola, as such the force on a micro–bunch electron is not proportional to its displacement from the axis of propagation. The electron motion cannot be described by simple harmonic motion and the frequency of oscillation is not independent of the particles initial transverse displacement. Theoretically a properly tailored transverse plasma density profile could provide a force that is proportional to the transverse displacement from the axis of propagation, leading to the same oscillation frequency for the micro–bunch electrons.

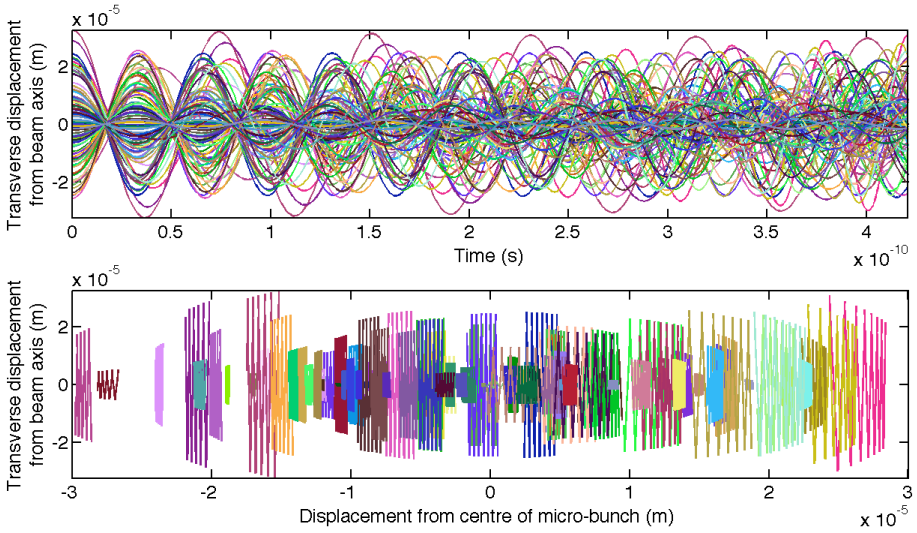

Figure 5.2.: Trajectories of 1000 electrons populating a Diamond beam micro–bunch simulated using RDTX. The top pane plots the transverse displacement of an individual micro–bunches electrons as a function of time. The bottom pane plots the transverse displacement of the electrons as a function of longitudinal displacement from the centre of the micro–bunch.

and the tail which experience diminished focusing fields and have a lower oscillation frequency.

The electrons in this simulation oscillate with a maximum amplitude of $r_0 = 2.75 \times 10^{-5}$ m and an average oscillation frequency $\omega_{B_{avg}} = 8.31 \times 10^{10}$ rads s^{-1} with a frequency spread of $\Delta\omega/\omega = 0.324$. The theoretical oscillation frequency is given by equation 2.50 and found to be $\omega_B = 8.8 \times 10^{10}$ rads s^{-1} which is in agreement with that observed in the RDTX simulation. It is important to note at this point that the amplitude of oscillation is not the same for all the electrons but varies considerably, unlike the amplitude of oscillation in conventional undulators and wigglers. For electrons oscillating with this maximum amplitude the undulator parameter is $K = 150$, given by equation 2.52. Therefore these electrons behave similarly to those in a wiggler, emitting radiation that is spatially decoupled. As such the radiated spectrum is broad without the characteristic peaks found in the spectra produced by undulators. However, electrons populating the centre of the micro–bunch have a small enough r_0 such that $K < 1$ and emit radiation that is not spatially decoupled. Given $\omega_B = 8.31 \times 10^{10}$ rads s^{-1}, the r_0 required to give an undulator parameter of $K < 1$ is $r_0 = 1.83 \times 10^{-7}$ m. The radiated spectrum of such

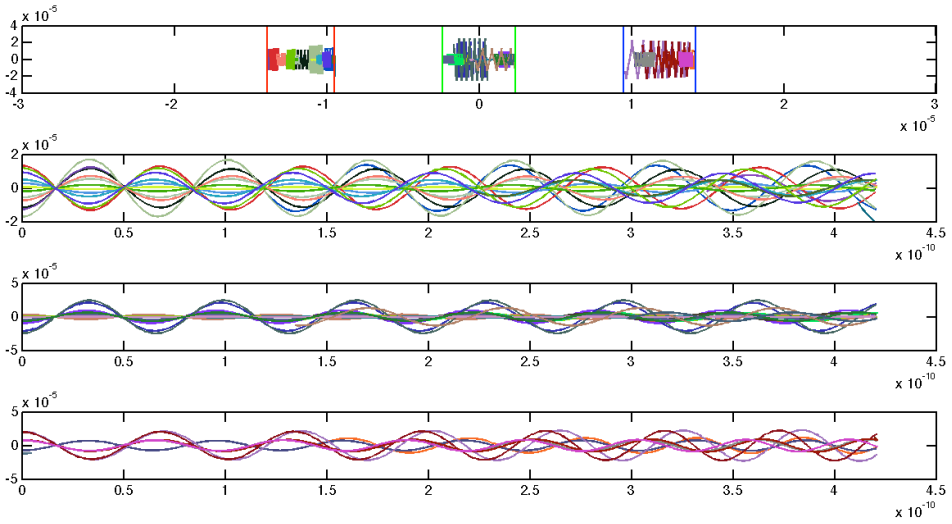

Figure 5.3.: Trajectories of electrons lying within narrow regions of a Diamond beam micro–bunch, co–propagating with a high amplitude wakefield. The top pane plots transverse displacement as a function of longitudinal displacement from the centre of the micro–bunch for electrons within three narrow regions. The second, third and fourth panes plot the transverse displacement of bunch electrons as a function of time for the regions defined by the red, green and blue lines respectively.

electrons would interfere, producing a spectrum with sharp peaks at the undulator's harmonics. For a Gaussian beam with $\sigma_r = 38$ μm it is found that 0.4% of the charge lies in the region $r_0 < 1.83 \times 10^{-7}$. Therefore the vast majority of electrons have $K > 1$ and behave as if in the wiggler regime.

5.2. Micro–bunch Coherence Length

The coherence length for a source is defined simply as $L_{co} = c/\Delta f$, giving a coherence length of $L_{co} = 71.4$ mm between all the electrons throughout the simulated micro–bunch. The bottom pane of figure 5.2 shows the transverse displacement of the same electrons against the longitudinal displacement from the centre of the micro–bunch. It is important to note from the bottom pane that although the particles do move longitudinally within the micro–bunch, they only move a fraction of the bunch length. This means that the X–rays radiated from an individual electron are spatially decoupled from those radiated by electrons a significant distance from that particle's

initial longitudinal position. This implies that although transverse coherence is lost between all the electrons of the micro–bunch after just a few oscillations as in the top pane of figure 5.2, the electrons within a narrow longitudinal region of the micro–bunch, which experience similar focusing fields, will remain coherent for longer.

Figure 5.3 examines the trajectories of electrons from three regions with respect to the centre of the micro–bunch. Those that populate -16μm $\pm 2.5\mu$m (red vertical lines in the top pane), $\pm 2.5\mu$m (green vertical lines in the top pane) and $+16\mu$m $\pm 2.5\mu$m (blue vertical lines in the top pane). The trajectories of the electrons in these three regions are plotted in the second, third and fourth pane respectively. The coherence length when considering only the electrons in these narrow regions increases with decreasing region length, giving an average coherence length of $L_{co} = 700$ mm in the three examples in Figure 5.3. As the micro–bunch propagates further through the second plasma stage the electrons have more time to slip longitudinally throughout the micro–bunch, resulting in diminished transverse coherence.

If brilliance is favoured over coherence then the second plasma stage can be extended, allowing the oscillating micro–bunches to co–propagate with the wakefield for longer radiating more X–rays.

5.3. Radiated Spectrum of the Oscillating Micro–bunch

The radiated spectrum of the whole of the micro–bunched Diamond beam can be approximated by extrapolating the radiated spectrum of the representative micro–bunch to account for the 74.7% of the beam experiencing the $E > 1$ GVm^{-1} wakefield. The output of the RDTX simulation was expressed in terms of peak brilliance using equation 5.1, restated here for convenience:

$$\hat{B} = \frac{N_B}{(2\pi)^3 \epsilon_x \epsilon_y \epsilon_E \tau}, \tag{5.1}$$

where N_B is the number of photons per pulse per 0.1% band width, ϵ_x and ϵ_y are the transverse rms emittance of the X–ray pulse and ϵ_E is the fractional energy spread of the X–ray pulse. Effectively peak brilliance is the number of photons, in a 0.1% band width frequency window, per unit six dimensional phase space volume. This calculation will be broken down by first calculating the phase space volume and then the number of photons per 0.1% frequency window.

5.3.1. Six Dimensional Phase Space Volume

Figure 5.4 shows the output of the RDTX code for the Diamond micro–bunch simulation, which is the energy deposited on the virtual spectrometer as a function of angle from the propagation axis, θ and the frequency of radiation, ω. The figure shows that the majority of the energy deposited is close to the axis ($\theta \simeq 0.001$ rads) and the spectrum is that of a synchrotron, i.e. lacks the narrow peaks emitted by an undulator. The left pane is integrated over the frequency of the photons and gives the root–mean–squared divergence of the photons. The bottom pane is integrated over angle of emittance and gives the spectrum of the radiation. The critical frequency of the synchrotron–like spectrum is given by this plot as $\omega_{crit} = 4.5 \times 10^{19}$ Hz with a FWHM energy spread of $\Delta\omega = 2.1 \times 10^{20}$ Hz. This gives a longitudinal emittance of $\epsilon_E = \Delta E/E = 2.812$.

The transverse beam size of the particle beam is used as an approximation of the X–ray transverse beam size and is displayed, as a function of time, in figure 5.5. The rms transverse beam size was found to be $\langle x \rangle = \langle y \rangle = 23$ μm. Given the quantities above, the six–dimensional phase space is found to be $V_{ps} = \epsilon_x \epsilon_y \epsilon_E \tau = 1.43 \times 10^{16}$ mm^2 mrad^2 s.

The number of photons per 0.1% bandwidth is found by taking the solid angle integrated spectrum and performing a moving point integration over the frequency window $\omega - \Delta\omega$ to $\omega + \Delta\omega$ where $\Delta\omega$ is 0.005. The peak brilliance is then trivially this quantity divided by the calculated phase space volume and the beam length, σ_t.

The code RDTX calculates the spectral intensity, $\frac{d^2I}{d\omega d\Omega}$, emitted by accelerating charge. To calculate the brilliance from this quantity one first finds the number of photons per relative bandwidth per steradian,

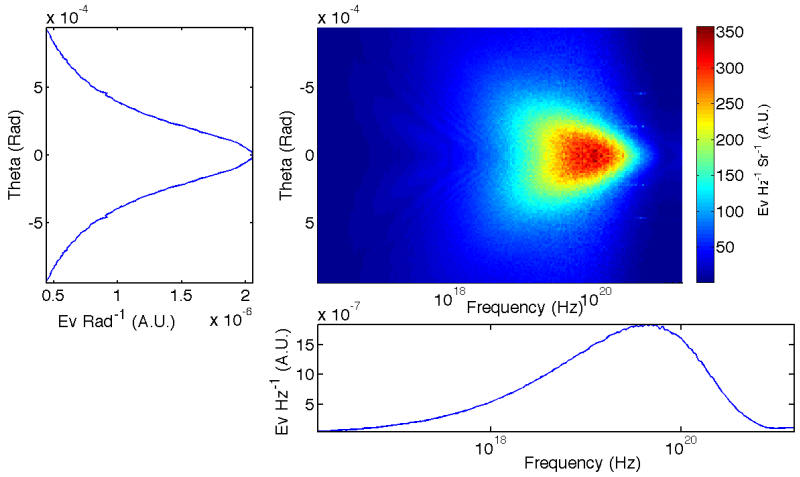

Figure 5.4.: The angularly resolved spectrum emitted by the representative Diamond micro-bunch (top right pane). The left pane is integrated over the frequency of the photons and gives the root-mean-squared divergence of the photons. The bottom pane is integrated over solid angle and gives the spectrum of the radiation.

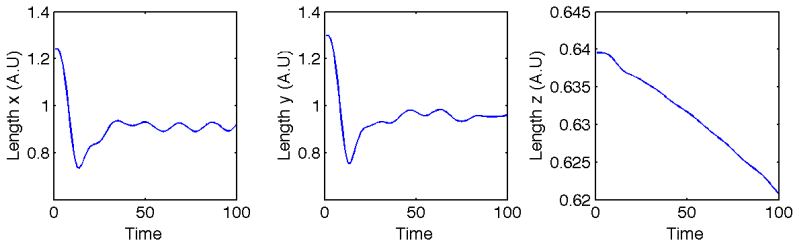

Figure 5.5.: The transverse and longitudinal root–mean-squared beam size of the Diamond micro–bunch in the second plasma stage. The initial transverse size compresses significantly during the first betatron oscillation before undergoing smaller amplitude oscillations. The length of the micro–bunch decreases throughout the simulation as the head of the bunch experiences the decelerating regions of the wakefield and the rear the accelerating.

$$\frac{d^2I}{d\omega d\Omega} = \frac{d^2N\hbar\omega}{d\omega d\Omega} = \hbar\frac{d^2N\omega}{\frac{d\omega}{\omega}d\Omega}, \tag{5.2}$$

where N is the number of photons and $\hbar$ is planck constant. Convention states that peak brilliance is given as the number of photons per 0.1% bandwidth, i.e. $\frac{d}{\frac{d\omega}{\omega}} = 10^3\frac{d}{d(0.1\%BW)}$. Furthermore peak brilliance is measured in milliradians squared, so $\frac{d}{d\Omega} = 10^6\frac{d}{d(\pi\theta^2)}$. Substituting these unit conversions into equation 5.2 yields,

$$\frac{d^2N}{d(0.1\%BW)d\pi\theta^2} = \frac{1}{10^9\hbar}\frac{d^2I}{d\omega d\Omega}. \tag{5.3}$$

This quantity is the number of photons per 0.1% bandwidth per milliradian squared. To find the peak brilliance one has to divide by the intrinsic source properties of the electron beam generating the pulse, the duration, τ, and the source area, σ_r^2, measured in millimetres squared (this convention adds a factor of 10^6 to the co-efficient to the right have side of equation 5.4).

$$\hat{B}\left[\frac{\text{photons}}{\text{s mm}^2\ \text{mrad}^2\ 0.1\%\text{BW}}\right] = \frac{1}{10^{15}\hbar\sigma_r^2\tau}\frac{d^2I}{d\omega d\Omega} \tag{5.4}$$

Figure 5.6 plots the peak brilliance of the single representative micro–bunch against existing third generation light sources. The peak brilliance of the X–ray pulse produced at the Diamond Light Source by the U-27 insertion device is shown for comparison. The peak brilliance produced by the Diamond U27 insertion device is shown in blue, with peak brilliance of $\hat{B} = 1.8 \times 10^{20}$ photons mm$^-$2 mrad$^-$2 s$^-$1 0.1%BW at $E = 2$ keV. The peak brilliance of the two–stage–device is $\hat{B} = 1.9 \times 10^{23}$ photons mm$^-$2 mrad$^-$2 s$^-$1 0.1%BW at an energy of $E = 59$ keV. The two–stage device yields a three orders of magnitude improvement when compared to the existing U27 insertion device and a factor of thirty increase in peak X–ray energy. This is accomplished over hundreds of millimetres as opposed to the tens of metres required by conventional magnetic insertion devices. Broad band emission is seen and there are no characteristic narrow energy bands, as would be seen from an undulator. In

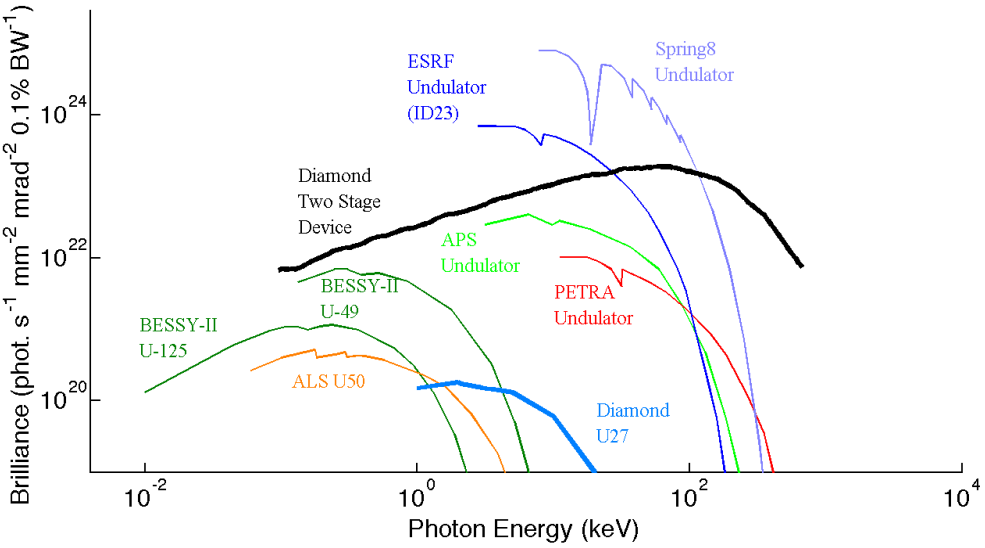

Figure 5.6.: The peak brilliance of various third generation light sources compared to the X–ray pulse produced by a Diamond beam micro–bunch in the two–stage device. The peak brilliance produced by the Diamond U27 undulator is shown in blue, with peak brilliance of $\hat{B} = 1.8 \times 10^{20}$ photons mm^{-}2 mrad^{-}2 s^{-}1 0.1%BW at $E = 2$ keV. The peak brilliance of the two–stage–device is $\hat{B} = 1.9 \times 10^{23}$ photons mm^{-}2 mrad^{-}2 s^{-}1 0.1%BW at an energy of $E = 59$ keV.

contrast to betatron oscillations that arise from electrons injected in the blow–out laser wakefield regime (comprising typically of tens of pico–coulombs of charge [33, 72] oscillating over millimetres), a nano–coulomb of charge in the micro–bunches undergo these coherent oscillations over hundreds of millimetres.

Radially polarised X–rays can overcome the diffraction limit when strongly focused and have a longitudinal component to the electric field at the focus [73] with use of a suitable aperture. These properties could potentially allow for a unique single–atom probe. It should be noted that, as the peak brilliance of a synchrotron–like source is proportional to the charge of the beam and inversely proportional to the length of the beam, the peak brilliance of the micro–bunch train will be on the order of the single representative micro–bunch.

The number of photons within an X–ray pulse is proportional to the charge of the micro–bunch that generated it. As such, the train of micro–bunches passing through the two–stage device generates a train of X–ray pulses. This allows for an interesting time resolved diagnostic to be pursued whereby a streak camera could be

used separate the images produced by individual X–ray pulses. For those applications that require femtosecond or even shorter duration X–ray pulses, the second stage can be used to accelerate a suitably conditioned witness electron beam up to 6 GeV. This witness bunch can be injected into a conventional undulator to generate harder X–ray pulses of the required pulse duration. This chapter, in conjunction with the previous, have demonstrated via numerical simulations that the Diamond beam can produce X–ray pulses with three orders of magnitude increase over a wide bandwidth to peak brilliance and over an order of magnitude increase to photon energy when compared to conventional magnetic insertion devices. The two–stage device and laser required can be commissioned with feasible capital investment over metres of beam line. The treatment described is readily generalisable and applicable to many conventional beams, potentially revolutionising many applications utilising synchrotron radiation.

Chapter 6.

Experimental Setup at the Astra Facility

Diagnosing a plasma wakefield proves to be a difficult feat. The resonantly excited wakefield detailed in the previous chapters has a profile which varies along it's length, reaching a high fractional plasma electron number density perturbation of $\Delta n_e/n_e \simeq 0.3$. One way to diagnose such a wakefield is to co–propagate it with a long laser pulse, and measure the wakefield's photon acceleration effect on said pulse.

This chapter introduces the high power laser facility, diagnostics, targets and experimental configurations used to develop a diagnostic based on the photon acceleration effect. The Astra laser system at the Central Laser Facility at the Rutherford Appleton Laboratory was used to perform the experimental work detailed in this thesis.

6.1. The Astra Laser System

The Astra laser is an ultra–short high power high repetition rate laser system [74]. It is a Titanium doped sapphire laser that delivers a near infrared 800 nm central wavelength pulse of $E = 600$ mJ in $\tau = 40$ fs. The Astra laser system has a master–oscillator power amplifier architecture, meaning that a high quality short pulse at the start of the laser chain is successively amplified to higher energies throughout a series of amplifiers. The amplifiers are a transmissive medium with a damage threshold. Ultra–short high intensity lasers can have powers that exceed this threshold and

as such must be amplified by means of chirped pulse amplification, as detailed in section 6.1.1.

The initial seed pulse of the Astra laser is a low energy high quality 12 fs pulse. The bandwidth of the pulse allows glass blocks to be used to stretch the pulse to 7 ps and then amplified to a millijoule of energy by the preamplifier. A fast Pockel cell selects some of these amplified pulses at a rate of 10 Hz. These pulses then undergo chirped pulse amplification once more by first using diffraction gratings to stretch the pulses to 530 ps, and then passing the long pulse through three amplifiers to reach a final energy of 1 J. Stretching the pulse by nearly two orders of magnitude reduces the intensity by the same factor, ensuring damage is not done to the laser optics and amplifying medium. To keep the pulse intensity below the damage threshold as it passes through the three amplifiers, both the laser beam and crystals become larger. After the third amplifier the pulse is passed to Target Area 2 where it is compressed down to 40 fs achieving intensities of $I = 10^{19}$ Wcm^{-2} at focus. The pulse can also be passed through the Astra Gemini system which amplifies the pulse further to 15 J but this system was not used for the experiment detailed in this chapter. Target Area 2 has its own control room with remote diagnostics and triggering systems, isolating experimenters from the laser hazards.

6.1.1. Chirped Pulse Amplification

When the intensity of a laser pulse approaches the damage threshold of the gain medium the pulse can suffer from non–linear effects, such as self–focusing, photoionisation and avalanche ionisation [75]. Modern high power laser pulses regularly exceed the damage threshold of the transmissive optics that form part of the laser that generates them, so the intensities must be lowered whilst traversing these optics. To accomplish this, the pulse can be expanded transversely or stretched longitudinally to lower the peak intensity. Expanding a laser pulse transversely requires the size of the optic (for example a titanium sapphire crystal in an amplifier) to increase. This is costly and, although it is implemented in the generation of the Astra laser pulses it is not economically feasible on its own to produce cutting edge high power laser pulses.

Chirped Pulse Amplification [76] stretches the pulse longitudinally, reducing the intensity by the factor of length increase, before passing it through a gain medium

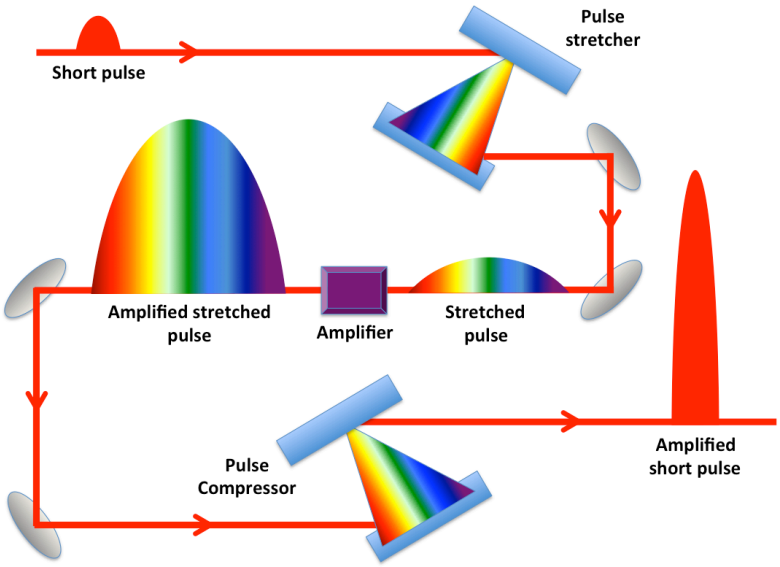

Figure 6.1.: Graphic of a short laser pulse undergoing chirped pulse amplification.

where it is amplified and then finally recompressed. Diffraction gratings disperse the laser pulse according to the wavelengths present, giving different path lengths through a pair of diffraction gratings for different wavelengths of laser light. This results in the pulse being both chirped and stretched as shown in figure 6.1 and can be stretched this way by up to three orders of magnitude. The stretched pulse is then amplified before being recompressed by a second pair of diffraction gratings whose geometry is such that they exactly counter the path length differences introduced by the first pair of gratings. As chirped pulse amplification can stretch a pulse, with power near the damage threshold of the system's optics, by three orders of magnitude, it allowed for the amplification of pulses with up to three orders of magnitude more energy. This led to huge advances in the intensities and peak powers attainable by laser systems [77].

6.2. Experimental Setup

Figure 6.2 shows a schematic of the experimental area, which includes the target chamber (centre) and two diagnostic tables (top and left). The Astra laser pulse enters the target chamber through the right port, first striking mirror M1. Mirrors M1 through to M4 steer the pulse first onto an off–axis parabolic mirror before

taking the now focusing pulse onto the gas jet, defined as target chamber centre (TCC). The Astra laser impinges on the supersonic gas jet, ionising a channel of the gas and driving a wakefield within, which traps and accelerates background plasma electrons. These accelerated electrons and surviving laser pulse travel from TCC to M14, which is a switchable magnetic base supporting different optics. If the electron spectrometer was to be used no optic was placed at M14, allowing the accelerated electrons to continue downstream from TCC, through the magnet M1 and impact upon the lanex screen mounted in the external cube. Light from TCC then passes downstream, past the lanex screen and onto the Andor soft X–ray spectrometer.

If the forward diagnostics table was favoured (left of the target chamber), then a mirror was placed at M14. The mirror steered the surviving laser pulse and light from other interaction effects first onto a spherical mirror, S1, for collimation and then out of the target chamber and onto the forward diagnostic table. The collimated collected light from TCC is focused by spherical mirror S2 onto three diagnostics: the spectrometer, an energy diode and the exit mode imaging diagnostic by a collection of mirrors and beamsplitters that ensure the path lengths to each are the same. A pickoff mirror was used to steer a small amount of the collimated light through further mirrors and onto the FROG. The FROG is the diagnostic around which the analysis in the following chapter is based, and as such will be discussed in further detail.

6.2.1. Frequency Resolved Optical Gating (FROG)

Frequency resolved optical gating (FROG) is a single shot diagnostic technique used to fully characterise ultra–short laser pulses, able to measure the full time–dependant electric field. When measuring a laser pulse a short probe pulse can be used to sample the longer pulse by crossing the two in a nonlinear crystal material (this nonlinear mixing is called gating). A third pulse is generated from where the two cross and contains information on the sampled pulse. This technique cannot be used when measuring ultra–short laser pulses on the cutting edge of technology as no shorter probe pulse exists. The FROG scheme gates the laser pulse with itself, as an auto–correlator [79] would, overcoming this problem. Figure 6.3 shows the schematic of a FROG diagnostic. The laser pulse is split and one of the split pulses is delayed with respect to the other before being gated in a frequency–doubling crystal.

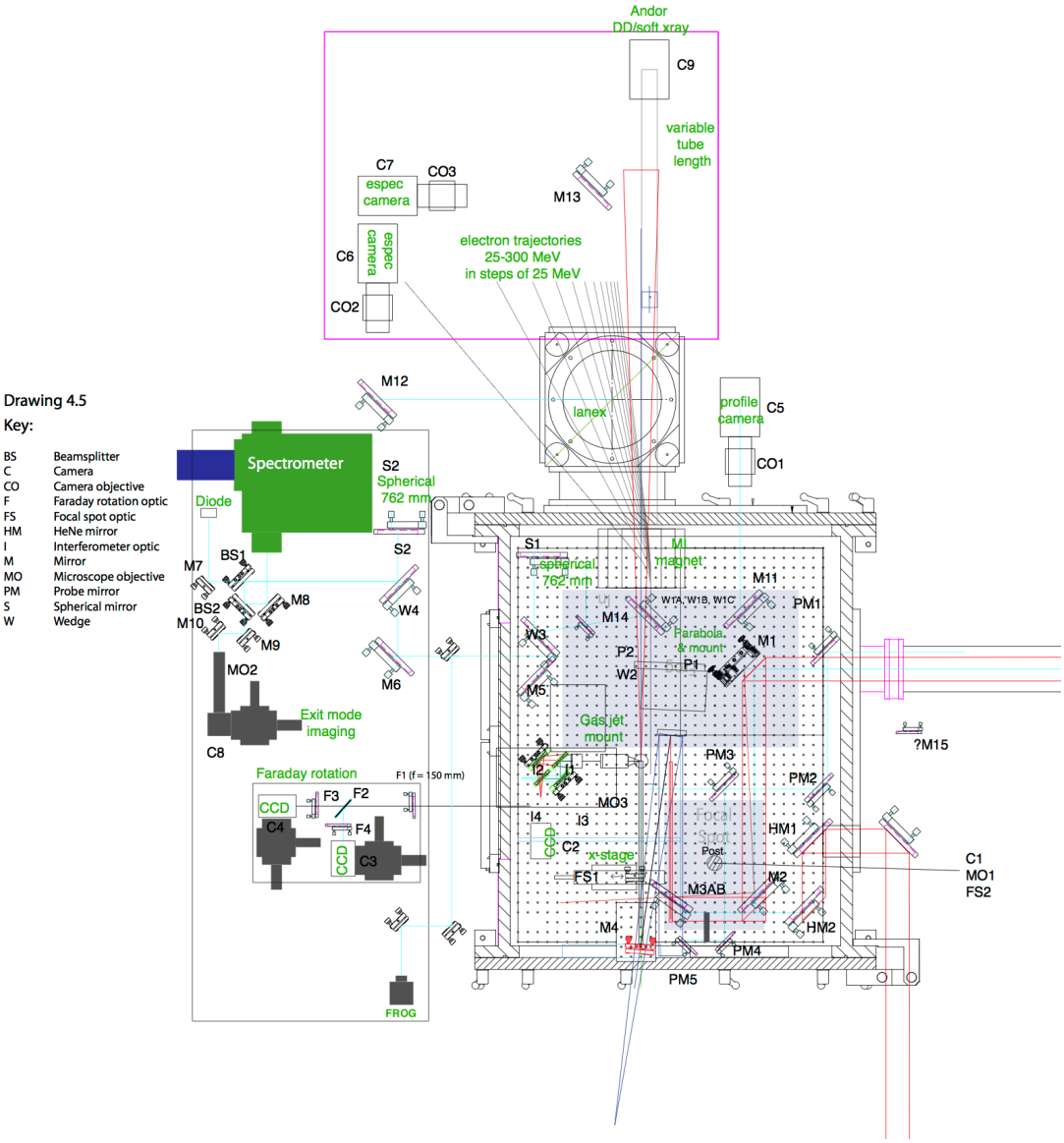

Figure 6.2.: Schematic [78] of the interaction point vacuum chamber (centre), electron spectrometer (above) and imaging diagnostic table (left) for the TA2 experiment.

This gating generates a nonlinear signal pulse which is then spectrally resolved with respect to the relative delay. The envelope of the FROG signal field has the form,

$$E_{sig}(t,\tau) = E(t)E(t-\tau), \tag{6.1}$$

where $E(t)$ is the complex envelope of the laser pulse and τ is the delay between the two beams. The intensity measured by the CCD array yields the FROG trace,

$$I_{FROG}(\omega,\tau) = \left| \int_{-\infty}^{\infty} E_{sig}(t,\tau)\exp(\mathrm{i}\omega\mathrm{t})\mathrm{dt} \right|^2, \tag{6.2}$$

$$I_{FROG}(\omega,\tau) = |E_{sig}(\omega,\tau)|^2. \tag{6.3}$$

A change in the sign of the delay time τ yields the same E_{sig}. This means that a second harmonic generation FROG trace is always symmetric about delay, leading to temporal ambiguity. This ambiguity can be overcome if an asymmetric time–dependent property of the pulse is known, such as the chirp. For this reason both positive and negative chirps are introduced to the laser driving pulse as discussed in the next chapter.

A pulse's phase and intensity can be retrieved from a spectrally resolved auto–correlation, i.e. the FROG trace, as the problem reduces to a two–dimensional phase–retrieval problem [80]. Such a problem has unique solutions and is solved in this thesis using the software FROGed[1] discussed in section 3.3.

6.2.2. Gas Jet

Gas jets are used in a variety of high intensity laser plasma interaction experiments, such as high harmonic generation [81], incoherent X–ray generation [82] and relativistic electron beam generation [83]. A gas jet releases a short burst of high velocity gas

[1] Acknowledgements to the authors Dr. Matthew Streeter and Dr. Edward Hill.

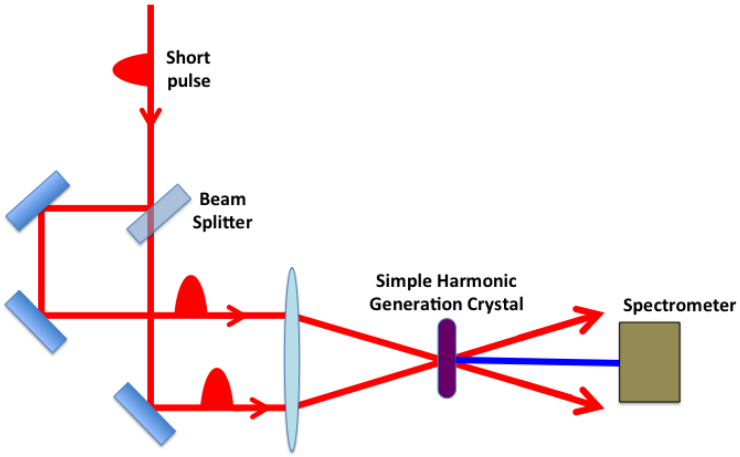

Figure 6.3.: Schematic for a frequency resolved optical gating diagnostic. The laser pulse to be measured is split and gated with itself in the non–linear medium, generating a new pulse (blue). The generated pulse is then spectrally resolved with respect to delay.

into the target chamber a short time before the laser pulse arrives. Advantages of gas jet targets include high repetition rates, the order of a thousand shot durability and shock free tailorable density profiles. The Astra laser pulse ionises the gas ahead of the high intensity peak of the pulse as discussed in section 2.2.5 providing the plasma. The gas jet is generated by having a high pressure reservoir of gas behind a nozzle, shown in figure 6.4, released by a Parker solenoid fast pulse valve shown in figure 6.5. By varying D_{crit}, D_{exit} and L_{opt} the plasma density profiles can be controlled and has been shown to yield a quasi–top–hat transverse density profile when the parameters are chosen carefully, with density decreasing with distance from the nozzle. Having a large D_{exit} for a given D_{crit} increases the angle of divergence of the emerging gas jet and therefore the Mach number, given by $\sin(\alpha) = M^{-1}$. Higher Mach numbers give higher exit velocities, sharper boundaries for the density profile and lower densities than low Mach numbers. D_{crit} should be chosen such that it is the most narrow point the gas flow experiences between its immediate storage and the target chamber. This is important as supersonic gas flow earlier in the system can affect the density of the final gas jet produced.

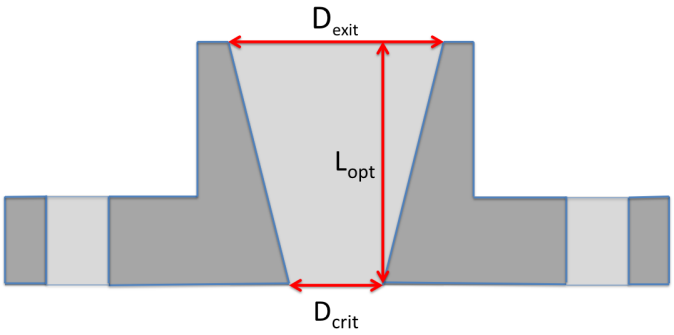

Figure 6.4.: The gas jet nozzle design [1] detailing the parameters which characterise the gas jet target. Properties of the gas jet such as density, Mach number and sharpness of the vacuum–gas boundary are set by these parameters.

Figure 6.5.: The Series 9 solenoid fast pulse Parker valve [84] used in the Astra TA2 experiment.

The nozzle used has parameters $D_{crit} = 1$ mm, $D_{exit} = 2$ mm and $L_{opt} = 6$ mm. This nozzle gives a nearly top–hat density profile with a sharp boundary, which is preferred for simple plasma wakefield experimental set ups that aim to accelerate electrons. The constant density gives a constant plasma wavelength and a stable region in which electrons can be accelerated, as well as being readily modelled in numerical simulations.

6.2.3. Electron Spectrometer

S. Mangles *et al.* were the first to drive a wakefield producing a narrow energy spread electron bunch [13]. This experiment was in fact performed using the Astra laser as the drive beam. An electron spectrometer was necessary to determine if the electrons produced from the plasma were of a narrow energy spread, as expected from wakefield acceleration, or if they had a continuous energy spread indicative of other processes. A narrow energy spread electron beam would indicate that a high amplitude wakefield was being driven, allowing any phenomena detected by more novel diagnostics, such as the FROG, to be more confidently attributed to laser–wakefield interactions. Furthermore, characterisation of the electron beam is an essential accompaniment to analysis of any X–rays produced by the laser–plasma interaction to investigate betatron emission.

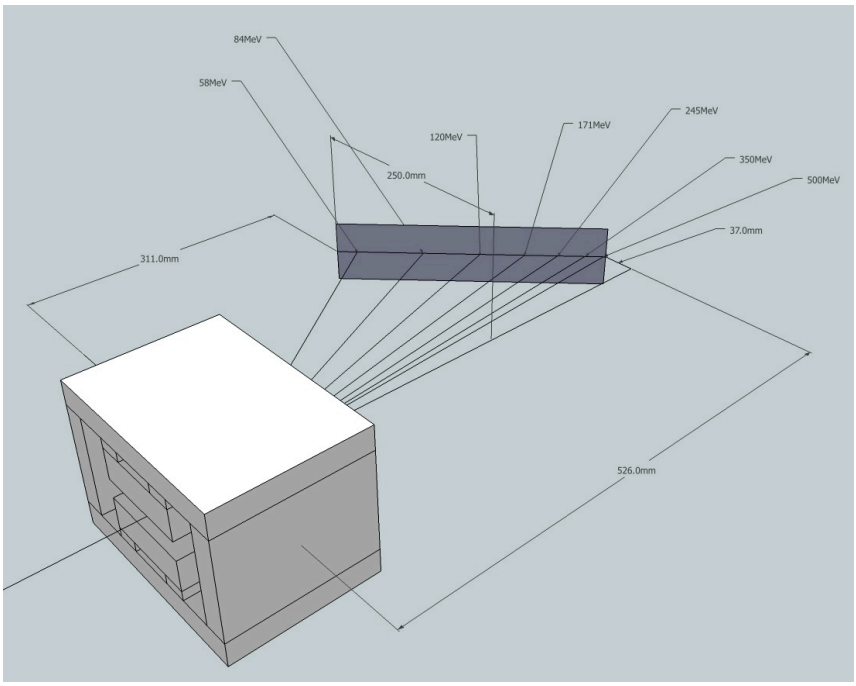

Figure 6.6.: Schematic of the electron spectrometer used in the TA2 experiment. A $B = 1$ T magnet bends the electrons according to their energy onto a lanex screen where the spectra are recorded by a camera positioned behind the screen (not shown).

The electron spectrometer was comprised of a $B = 1$ T magnet and a lanex screen covered by anodised aluminium foil, as in figure 6.6. The anodised foil prevents the laser light from activating the lanex screen and has been used in this configuration experimentally [85]. The magnet design was such that the fringe field lines were minimised by use of an appropriate yoke to simplify analysis of electron trajectories through it. The position of the lanex screen was placed such that it could reliably measure electrons in the energy range $E = 50 : 350$ MeV. Lanex is a composite material comprising of a phosphor layer backed by a polyester support that is activated by the electron beam. The phosphor atoms' electrons are excited to a meta stable state by the electron beam and scintillate over a timescale of milliseconds as the states decay [86] back down to the lower energy state. This property of prolonged scintillation allows the camera collecting the light from the lanex screen to do so some time after the laser pulse has passed. If the camera attempted to capture as the electrons were impacting upon the lanex screen the laser light would dominate over any scintillation.

Chapter 7.

Photon Acceleration as a Wakefield Diagnostic

This chapter analyses the photon acceleration effect of the plasma on the Astra laser pulse and uses this modulation of the laser intensity envelope to infer the plasma density. Photon acceleration as a diagnostic allows for characterisation of both the plasma and the wakefield being driven within on a single shot basis.

The laser light emerging from the gas target is captured by a grenouille, recording a full phase and intensity measurement of the pulse. A strong modulation to the intensity profile of the emerging pulse is seen with a well defined frequency. The modulation is caused by the laser pulse co–propagating with a wakefield and the frequency of the modulation is therefore the plasma frequency, which is used to calculate the plasma density. A first iteration set of simulations using the PIC code OSIRIS demonstrates modulation to the intensity profile of the Astra laser pulse is that of the plasma frequency.

7.1. Characterising the lengthened Astra Pulse

To sample many periods of the wakefield the Astra laser pulse was stretched from its nominal length of $\tau = 40$ fs, as seen in the third pane of figure 7.1, to $\tau = 200$ fs as seen in the fourth pane. To accomplish this, group velocity dispersion was introduced by the dazzler at the start of the laser chain such that the laser pulse emerging from the compressor was lengthened. Figure 7.1 shows the effect of four different group

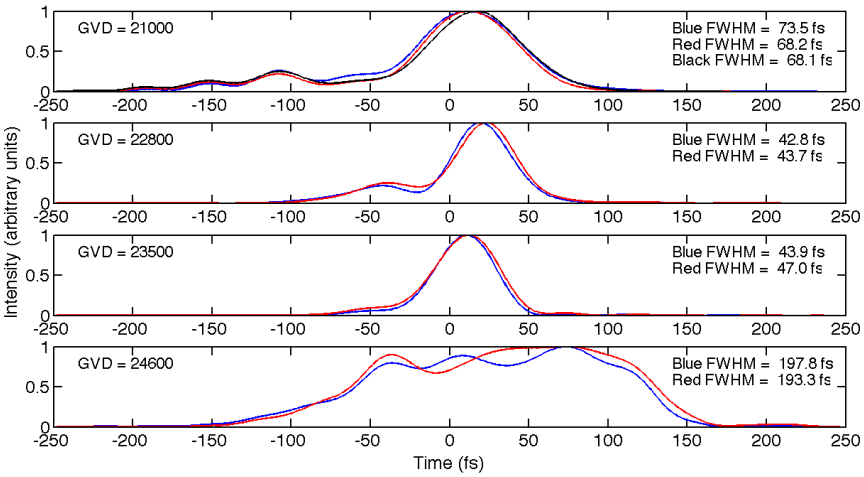

Figure 7.1.: The experimentally measured intensity profile of the Astra laser pulse after introducing group velocity dispersions by the dazzler. The red shots and blue shots were taken two hours apart, demonstrating the level of reproducibility of the intensity profiles.

velocity dispersions on the post–compressor pulse intensity profile and figure 7.2 shows the spectrum of the laser pulse before the laser–plasma interaction.

Each group velocity dispersion value has two measurements taken, two hours apart. It is seen that there is shot to shot variation and that the intensity profile of the pulse is not well described by simple models such as a Gaussian distribution. This is important to note as the presence of a periodic component to the intensity profile could be mistaken for an effect of the plasma post interaction, as well as possibly seeding the self modulation instability.

7.2. Reconstructing Laser Intensity Profiles

The raw data captured by the grenouille is a spectrally resolved auto correlation of the laser pulse, and is described in further detail in section 6.2.1. The code FROGed was used to extract the phase and intensity profile of the laser pulse from the grenouille traces. The code makes a best guess as to the intensity profile and phase of the laser pulse responsible for creating such a trace and then iteratively improves the guess by switching between several algorithms. The code converges on a unique solution given a correctly recorded trace and enough iterations. Figures

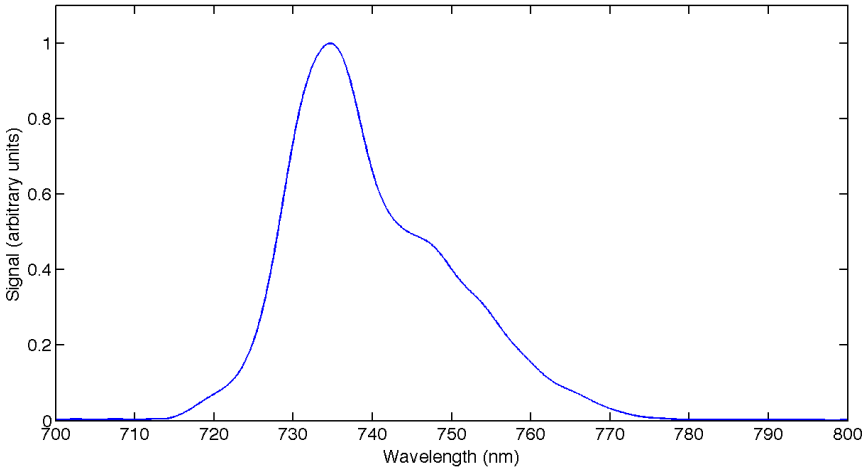

Figure 7.2.: The spectrum of the Astra laser pulse measured by a SPIDER at the start of the laser chain. With a FWHM bandwidth of 20 nm the transform limited pulse duration of a sec^2 profile beam is 40 fs. It should be noted that the centre of this $\lambda = 735$ nm spectrum pulse is not representative of the centre of the on target pulse as the longer wavelengths are preferentially amplified throughout the laser chain — leading to a $\lambda = 800$ nm centred pulse.

7.3 and 7.4 show the raw trace (top left pane), the best guess of the algorithm (top right pane), the recovered intensity profile (bottom left) and the spectrum (bottom right) of the laser pulse at the entrance of the grenouille for two shots.

A percentage error between the raw traces and the best guesses of the FROGed code below 5% were considered to have achieved a good level of convergence. The twelve shots that showed this high level of convergence fell within the range of nozzle backing pressures of 0.2 to 5 bar, achieving an average percentage error of 4.39%. It was found that at higher backing pressures insufficient laser light survived the higher density plasma to be detected by the grenouille and that at lower backing pressures so much light survived the interaction that the grenouille's CCD became saturated.

The reconstructed intensity profile of the laser has multiple distinct peaks at the entrance of the grenouille. However, the effect of the transmissive optics detailed in figure 6.2 have not been accounted for so any periodicity seen in the intensity profile at the entrance of the grenouille cannot be attributed to the plasma frequency.

To retrieve the laser pulse emerging from the plasma the laser pulse measured at the entrance to the grenouille must be back propagated through the upstream optics, accounting for any group velocity dispersion those optics would introduce.

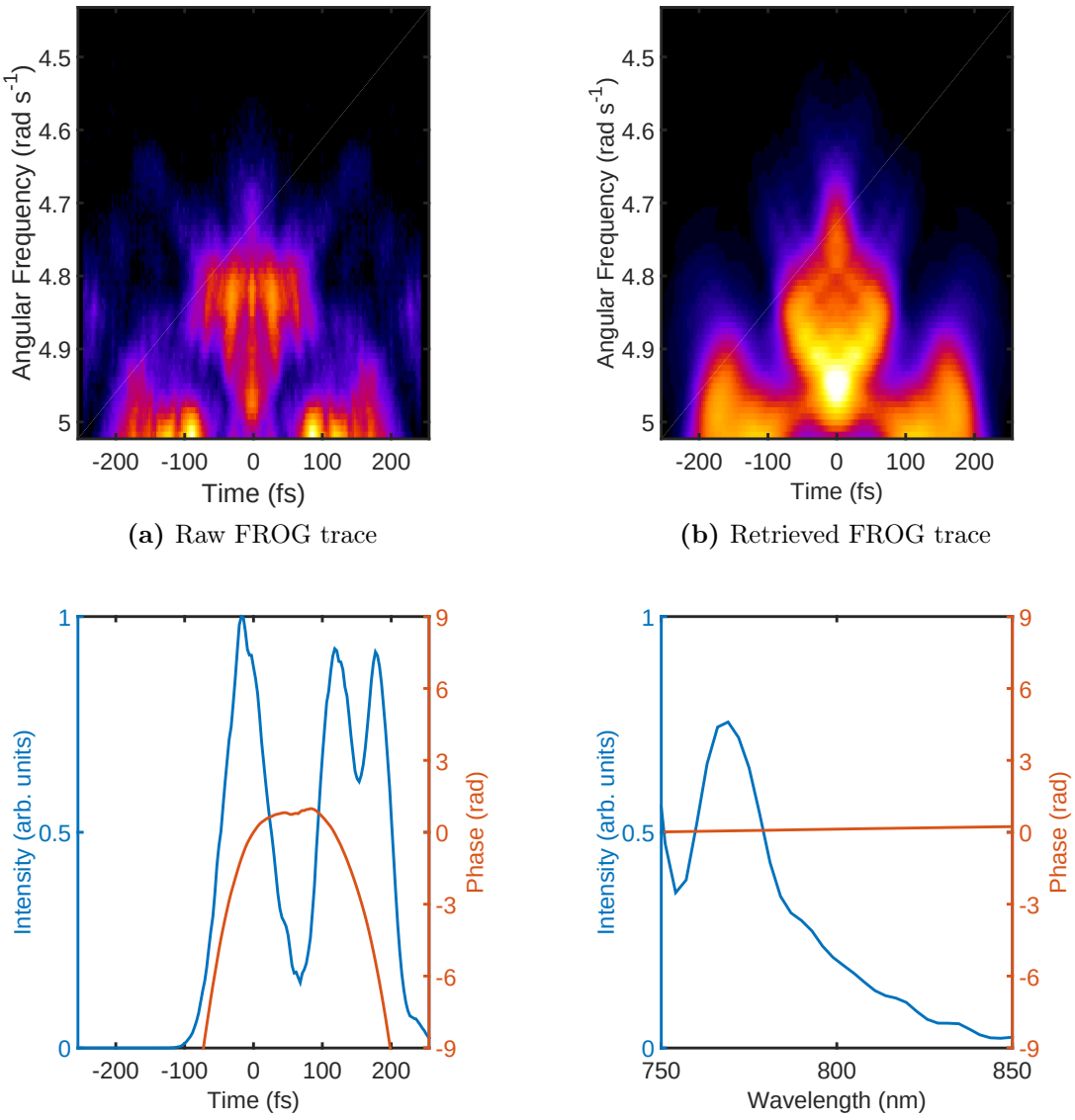

(a) Raw FROG trace

(b) Retrieved FROG trace

(c) Retrieved laser intensity

(d) Retrieved laser spectrum

Figure 7.3.: The recovered FROG trace from the FROGed code (top right pane) along with the laser pulse intensity profile and laser pulse spectrum that generates the recovered trace (bottom left and bottom right respectively). The raw data captured by the grenouille is displayed in the top left pane. The nozzle backing pressure for this shot is 2.3 bar.

Group velocity dispersion acts to delay higher frequency photons with respect to the lower frequency photons. The effect on an unchirped Gaussian pulse would be to lengthen it whilst decreasing the peak intensity. The effect on a chirped pulse would be to compress or lengthen the pulse depending on the sign of the chirp. If a

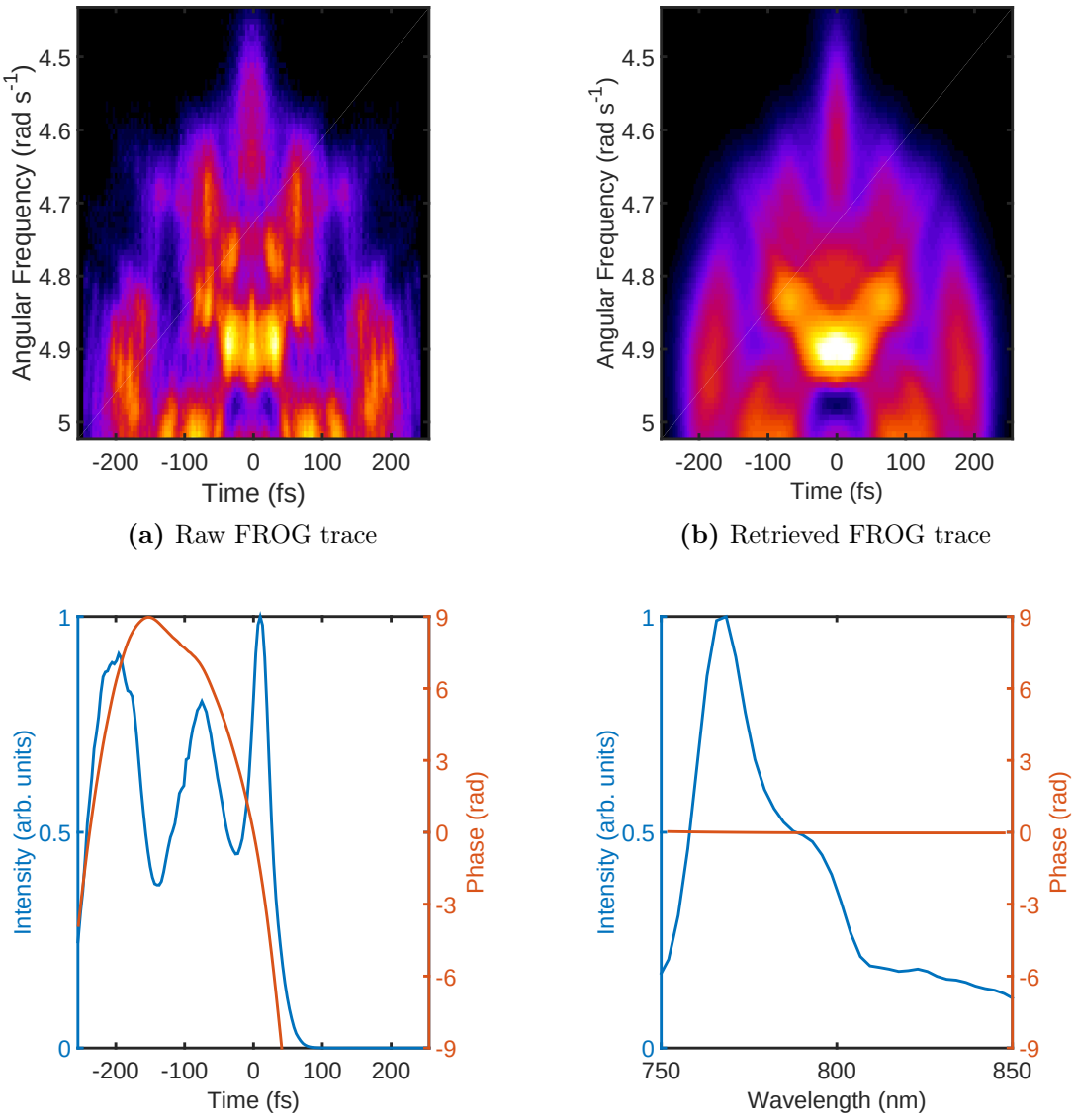

(a) Raw FROG trace

(b) Retrieved FROG trace

(c) Retrieved laser intensity

(d) Retrieved laser spectrum

Figure 7.4.: The recovered FROG trace from the FROGed code (top right pane) along with the laser pulse intensity profile and laser pulse spectrum that generates the recovered trace (bottom left and bottom right respectively). The raw data captured by the grenouille is displayed in the top left pane. The nozzle backing pressure for this shot is 3.1 bar.

chirped pulse was to have a complex intensity profile an arbitrary introduction of group velocity dispersion acts to wash out the structure. Given the pulse is known to contain a chirp before interaction with the plasma, and the photon acceleration effect

introduces chirp over the scale length of a plasma period, it is crucial to account for the group velocity dispersion introduced by the optics upstream of the grenouille.

7.3. The Effect of Group Velocity Dispersion

The reflective optics have a 100 nm coating of fused silica, which, at 45° incident angle and taking a double pass introduces a path length of 141 nm of fused silica per reflective optic. The transmissive optics introduce far more in total however. The wedge labelled as W13 introduces 7.5 mm of fused silica to photons travelling at 45° through its centre. When propagating through the wedge the laser light is collimated, and remains so until it reaches the entrance of the grenouille where an aperture selects a narrow region of the laser light (< 1 mm). The selection of a narrow region minimises the effect of the varying path difference through the wedge experienced by photons at the centre of the laser pulse compared to photons traversing the thick or thin end of the wedge.

A back propagation code was used to account for the group velocity dispersion introduced by the transmissive optic and the intensity profile of the laser emerging from the plasma was found. Figures 7.5 and 7.6 show the intensity profiles for two shots and the Fourier transforms after back propagation. A striking modulation to the laser envelope is seen with near distinct micro–pulses being formed in the shots in the top panes. The Fourier transform of the intensity profiles in the bottom panes shows a well defined frequency component to the modulations.

7.4. Reconstructed Plasma Density

Taking the frequency of the modulation to the laser intensity profiles, as seen in the bottom pane of figures 7.5 and 7.6, as the plasma frequency, the plasma densities are calculated. Plotting the plasma density as a function of nozzle backing pressure yields figure 7.7. This result shows a linear correlation between the nozzle backing pressure and the plasma density with a best fit of $n_e = 6.13 \times 10^{24} \times P + 2.03 \times 10^{23}$ m^{-3}, where P is the nozzle backing pressure in bar. The error on each datapoint has two main contributions. The FROGed code reconstruction introduces a percentage

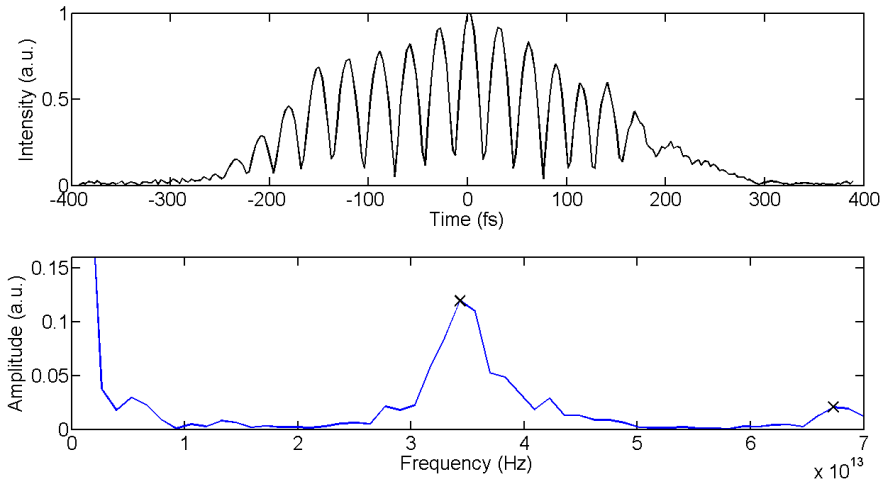

Figure 7.5.: The Astra laser pulse intensity profile of a shot back propagated through the transmissive optics upstream of the grenouille to the interaction point. The nozzle backing pressure for this shot is 3.5 bar.

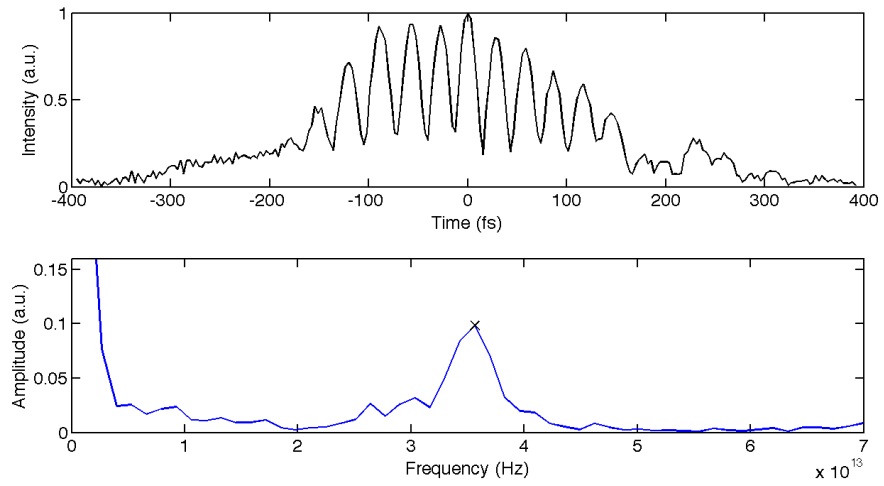

Figure 7.6.: The Astra laser pulse intensity profile of a shot back propagated through the transmissive optics upstream of the grenouille to the interaction point. The nozzle backing pressure for this shot is 4.7 bar.

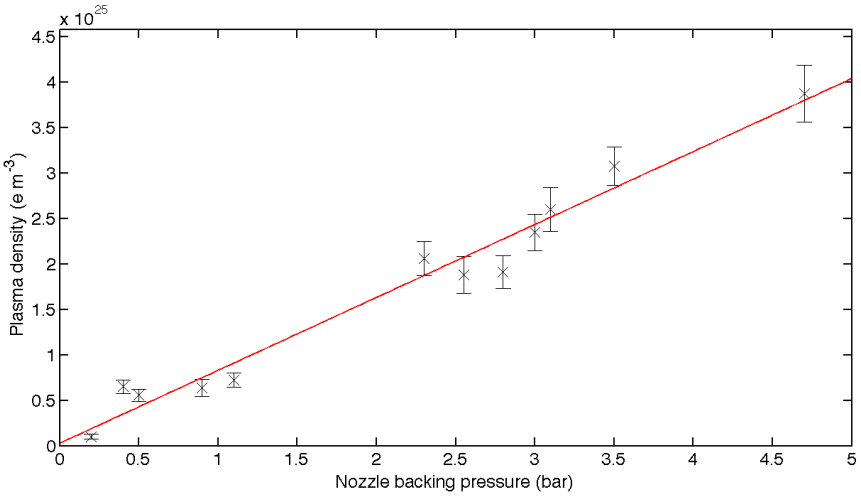

Figure 7.7.: The plasma densities calculated from the frequency of the intensity envelope modulation of the Astra laser pulse by the plasma as a function of the nozzle backing pressure.

error and the signal in the fourier transform of the intensity profile is fitted with a Gaussian which has an associated error.

The plasma densities are as high as $n_e = 3 \times 10^{25}$ m^{-3} at a nozzle backing pressure of 4.7 bar. Assuming doubly ionised helium at this pressure, this measured density is within the maximum electron number possible of $n_e = 5.4 \times 10^{26}$ m^{-3}.

7.5. Comparison with Numerical Simulation

A first iteration parameter scan over plasma density was performed to investigate the amplitude of the modulation to the laser intensity profile. The lengthened Astra laser pulse was simulated propagating through plasmas of five densities, parameters summarised in table 7.1.

In figures 7.8 and 7.9, modulation of the lengthened Astra laser pulses's intensity envelope at the plasma frequency is seen, with an increased amplitude of modulation at higher plasma densities. This effect is attributed to the modulation of the laser intensity profiles measured emerging from the plasma in figures 7.5 and 7.6. The calculated plasma densities of figures 7.5 and 7.6 are $n_e = 1.5 \times 10^{25}$ m^{-3} and $n_e = 2.3 \times 10^{25}$ m^{-3} respectively. In simulations, densities of $n_e = 2 \times 10^{25}$ m^{-3}

Grid	Values	Laser	Values	Plasma	Values
n_x	$j \times 1000$	a_0	0.868	*species*	He+
n_z	$j \times 10000$	ω_0	$41.76 \times \omega_p$	j	3 : 2 : 9
grid width (m)	50 c/ω_p	σ_t (m)	200 fs	n_e (m^{-3})	$j \times 10^{24}$
grid length (m)	30 c/ω_p	*profile*	*Gaussian*		

Table 7.1.: Density–scan parameters. For the grid parameters: n_x and n_z are the grid width and length respectively; and *grid width* and *grid length* are the physical width and length of the grid. For the laser parameters: a_0 is the normalised vector potential of the laser pulse; ω_0 is the pulses's normalised frequency, σ_t is the laser pulse's duration and *profile* is the laser pulses's intensity profile. For the plasma parameters: *species* is the ionised element composing the plasma; j is the integer parameter scanned over and n_e is the plasma electron number density.

and above show degradation of the modulation to the intensity profile of the laser at the plasma frequency, as shown in figure 7.9. The experimental measurements however, show that the laser pulse survives the interaction at these densities, and modulation to the intensity envelope at the plasma frequency can be seen up to $n_e = 4 \times 10^{25}$ m^{-3}. The idealised Gaussian intensity profile and perfect plasma density homogeneity of the simulation would lead to a stronger seeding and onset to the self–modulation instability when compared to experiment. Figure 7.10 shows the intensity profile of the laser pulse after propagation through 0.5 mm of plasma at density $n_e = 2 \times 10^{25}$ m^{-3}. Note that at this point a clear modulation to the plasma envelope is seen. It is upon further propagation that the degradation of this envelope occurs. In the experimental case however, this point of significant modulation may be reached after longer propagation distances through the plasma due to imperfections in the laser profile, as seen in figure 7.1, lower energy on target and so on, explaining why modulated laser intensity profiles are seen at up to twice the densities seen in simulations.

In summary an experiment was performed using the Astra laser system at the Central Laser Facility where the modulation to the laser intensity profile by the wakefield the laser pulse was driving was used to calculate the plasma density. An under populated dataset yielded measured plasma densities that correlated well with the nozzle backing pressures. The simulations presented qualitatively support the

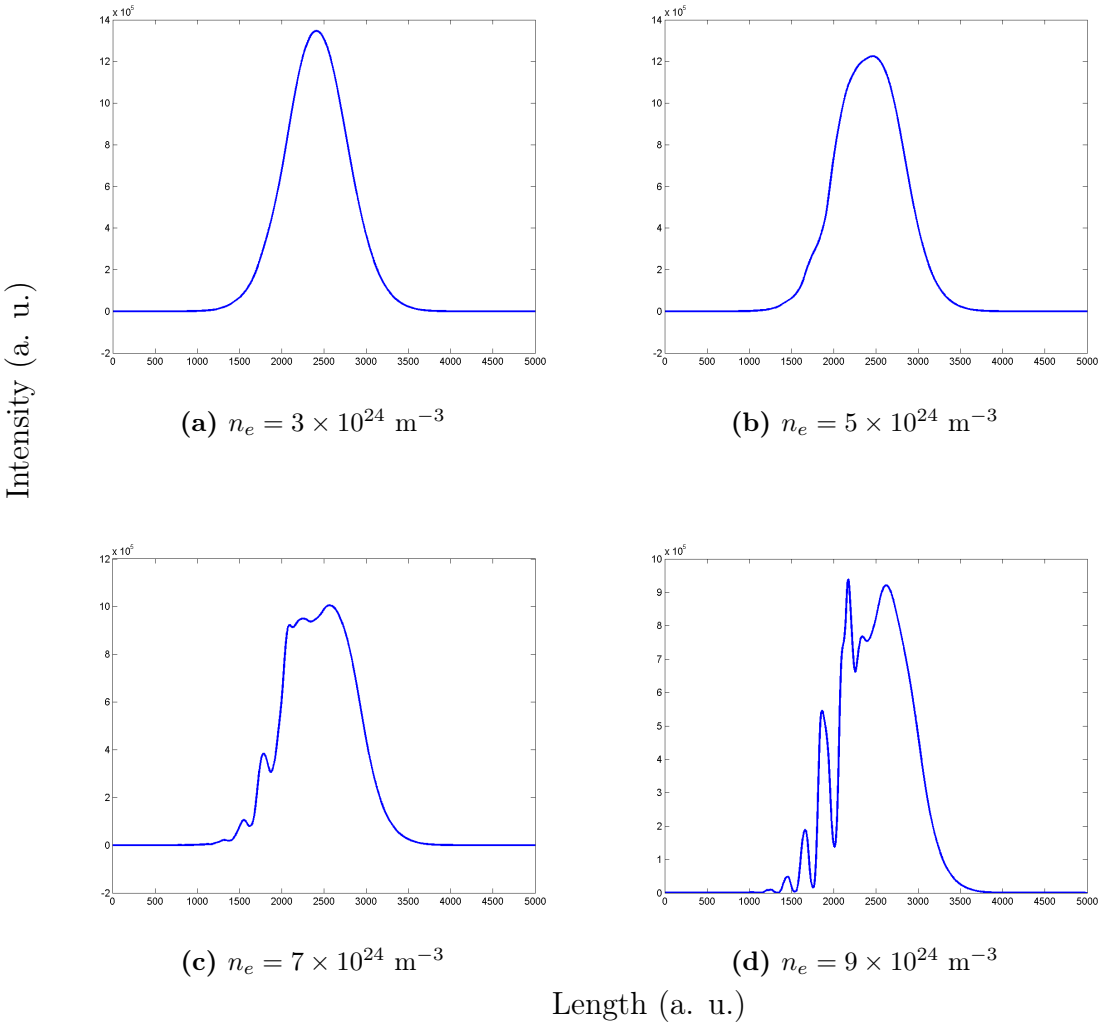

(a) $n_e = 3 \times 10^{24}$ m^{-3} **(b)** $n_e = 5 \times 10^{24}$ m^{-3}

(c) $n_e = 7 \times 10^{24}$ m^{-3} **(d)** $n_e = 9 \times 10^{24}$ m^{-3}

Figure 7.8.: Simulations [87] of the lengthened $\tau = 200$ fs Astra laser pulse after propagating through 2 mm of helium plasma at various densities. Simulations performed in OSIRIS by M. Kasim.

theory that the laser intensity envelope is modulated at the plasma frequency. This method of diagnosing the plasma density requires no dedicated probe pulse but instead relies on analysing the modulations to the laser pulse driving the wakefield, allowing for a low cost diagnostic requiring only downstream optical components from the interaction point and an appropriate FROG or grenouille. For the diagnostic to work, a significant amount of the laser pulse has to survive the interaction, so higher energy pulses are needed for larger plasma densities over longer propagation distances.

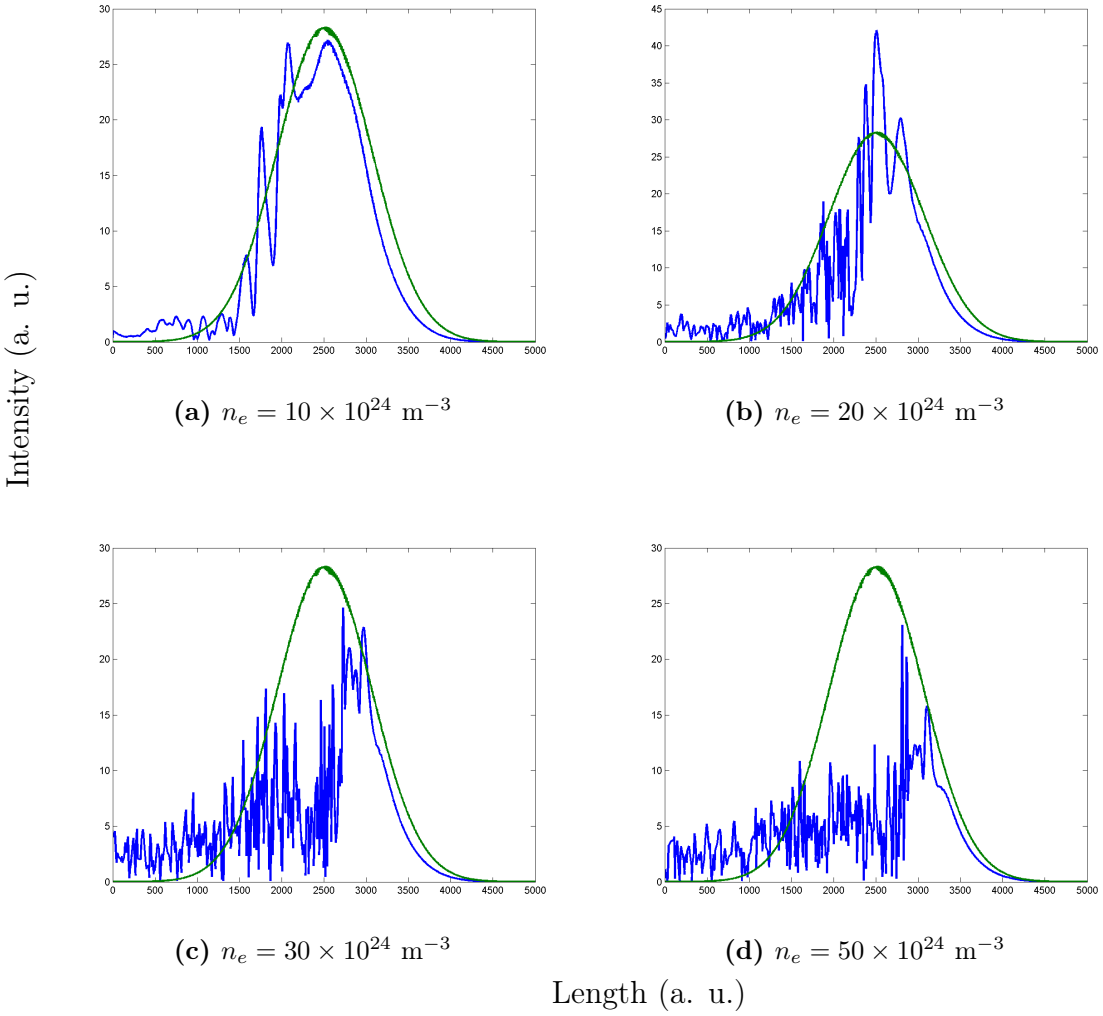

(a) $n_e = 10 \times 10^{24}$ m^{-3} **(b)** $n_e = 20 \times 10^{24}$ m^{-3}

(c) $n_e = 30 \times 10^{24}$ m^{-3} **(d)** $n_e = 50 \times 10^{24}$ m^{-3}

Figure 7.9.: Simulations [87] of the lengthened $\tau = 200$ fs Astra laser pulse before interaction (green line) and after propagating through 2 mm of helium plasma (blue line) at higher densities. Simulations performed in OSIRIS by M. Kasim.

Attenuating the laser pulse after interaction will allow the diagnostic to probe lower plasma densities, so long as the propagation distance through the plasma is increased to allow for significant modulation to the laser intensity envelope. Future work includes taking a larger data set over a greater plasma density range, allowed by the introduction of attenuating optics, and cross checking the measured densities with other established fast plasma density diagnostics. Such a diagnostic would be suitable to implement on laser driven wakefield experiments where the length of the

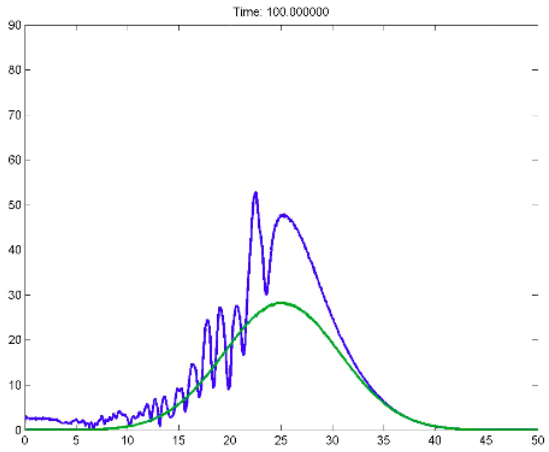

Figure 7.10.: The lengthened $\tau = 200$ fs Astra laser pulse after propagating through 0.5 mm of helium plasma of $n_e = 20 \times 10^{24}$ m^{-3}. The modulation to the laser envelope at the plasma frequency is maximised here and diminishes with further propagation.

laser pulse is several plasma wavelengths providing a direct single shot measurement of the plasma density in the region of the wakefield being driven.

Chapter 8.

Conclusions

This thesis has developed a novel two–stage beam line demonstrating, via numerical simulation, the generation of high brilliance X–ray pulses by utilising the advantages of both the laser driven and particle driven wakefields. A detailed study was presented, showing that brilliant X–ray pulses comparable to fourth generation light sources could be produced using the existing Diamond electron beam and commercially available laser systems. The novel beam line uses the high amplitude wakefield driven by ultra–short laser pulses to micro–bunch the long Diamond beam, allowing the Diamond beam to drive a high amplitude over longer propagation distances than a single laser pulse could. The co–propagation of the micro–bunch train with the driven wakefield provokes radial, whole bunch oscillations, stimulating copious X–ray emission. The wakefield driven by the micro–bunch train could also be utilised to accelerate a witness electron beam to higher energies than the 3 GeV Diamond beam.

The two–stage design is generalisable in such that the spacing between the stages, and length of the first stage can be tuned to micro–bunch other existing electron, and theoretically proton beams in the same way as demonstrated with the Diamond beam. This scheme could allow existing facilities to produce brighter X–ray pulses by violently oscillating their high charge, low emittance beams within plasmas instead of the lesser fields found in conventional insertion devices. The beam line for the Diamond beam is less than one metre in length and can be accommodated into the Diamond facility without major changes. An experiment is currently being planned where the beam line detailed will be implemented at the Diamond Light Source and the predictions of simulations tested. If the proof–of–principle experiment is

successful then utilising both laser and particle beam driven wakefields in this way promises to revolutionise the production of bright X–ray pulses.

Experimental results were presented of a plasma wakefield diagnostic utilising the photon acceleration effect. The Astra laser, at the Central Laser Facility was lengthen to several plasma periods long and used to drive a wakefield in a variety of plasma densities. Periodic modulation to the laser envelope at the plasma frequency was expected from simulation and seen experimentally. Strong modulations were seen with the laser pulse being comparable to a pulse train. The measured plasma density scaled with nozzle backing pressure as expected and was within the maximum density allowable by experimental constraints. A future experiment is planned at the Astra target area 2 late 2015 where a larger data set will be taken and the measured plasma density cross checked against independent diagnostics. The single–shot diagnostic is attractive in that it requires no dedicated probe pulse and no optics upstream of the interaction. For laser–driven experiments with drive pulses longer than the plasma period the diagnostic achieves a minimally intrusive set up with a relatively small capitol investment. A Such diagnostic is well suited to diagnosing resonantly excited wakes, such as those driven by the micro–bunched Diamond beam. The long laser pulse samples many periods of the wakefield as it ramps up, allowing for the quality and spacing of the micro–bunches to be inferred. The limitations of this diagnostic include the need for a large wakefield and propagation distance product to impart significant modulation on the laser pulse and the inability to probe wakefields that are moving significantly slower than the group velocity of the laser pulse. Such wakefields have been witnessed in self–modulated beam driven wakefields towards the rear of the micro–bunch train

Appendix A.

Appendix

A.1. Theory

A.1.1. Debye Length Derivation

To derive the Debye length, we first consider Poisson's equation:

$$\nabla \cdot \mathbf{E} = \frac{\rho}{\epsilon_0}, \tag{A.1}$$

where $\mathbf{E}$ is the electric field, ρ is the charge density and ϵ_0 is the permittivity of free space. Using $\mathbf{E} = -\nabla\phi$, where ϕ is the potential, equation A.1 becomes

$$-\nabla^2\phi = \frac{\rho}{\epsilon_0}. \tag{A.2}$$

In a uniform neutral plasma, the charge of the electrons and ions cancel completely, however in general this is not the case. ρ is then

$$\rho = n_i e - n_e e, \tag{A.3}$$

where n_e and n_i are the electron number density and ion number density respectively. Introducing a test change, equation A.3 becomes

$$\rho = n_i e - n_e e + s. \tag{A.4}$$

Boltzmann's law can be used to express the number density distribution, n, of a particle species in thermal equilibrium subject to a potential ϕ

$$n(r) = n_0 e^{-\frac{q\phi r}{k_B T}}, \tag{A.5}$$

where T is the temperature of the species, n_0 is the time averaged electron plasma density, k_B is the Boltzmann constant, q is the species' charge and r is position. Using equation A.5, equation A.4 becomes

$$\rho = e n_0 \big(e^{-\frac{e\phi}{KT_i}} - e^{\frac{e\phi}{KT_e}}\big) + s. \tag{A.6}$$

In one dimension, Poisson's equation is $\frac{\partial^2 \phi(x)}{\partial x^2} = \frac{\rho}{\epsilon_0}$. Substituting equation A.6 into Poisson's we find

$$-\frac{\partial^2 \phi(x)}{\partial x^2} = \frac{e n_0}{\epsilon_0}\big(e^{-\frac{e\phi}{KT_i}} - e^{\frac{e\phi}{KT_e}}\big) + s. \tag{A.7}$$

Solving equation A.7 analytically is non–trivial. We can linearise the equation using the assumption $\frac{e\phi}{KT} \ll 1$, allowing the approximations

$$e^{-\frac{e\phi}{KT_i}} \approx 1 - \frac{e\phi}{KT_i}, \tag{A.8}$$

$$e^{\frac{e\phi}{KT_e}} \approx 1 + \frac{e\phi}{KT_e}. \tag{A.9}$$

The linearised form of the poisson equation then becomes,

$$\frac{\partial^2\phi(x)}{\partial x^2} = \frac{e^2 n_0}{\epsilon_0}\left(\frac{1}{KT_i} + \frac{1}{KT_e}\right)\phi + s. \tag{A.10}$$

We can further simplify the equation by combining the ion and electron temperatures into an effective temperature, $\frac{1}{T_{eff}} = \frac{1}{T_e} + \frac{1}{T_i}$,

$$\frac{\partial^2\phi(x)}{\partial x^2} = \frac{e^2 n_0}{\epsilon_0 KT_{eff}}\phi + s. \tag{A.11}$$

Solving for ϕ gives the general solution

$$\phi(x) = \phi_0 e^{-x/\lambda_D}. \tag{A.12}$$

The Debye length is then:

$$\lambda_D = \sqrt{\frac{\epsilon_0 KT_{eff}}{n_0 e^2}}. \tag{A.13}$$

In convenient units, the Debye length can be expressed as

$$\lambda_D = 7.4\sqrt{\frac{T\ (eV)}{n_0\ (cm^{-3})}}m. \tag{A.14}$$

A.1.2. Ponderomotive Force Derivation

The ponderomotive force is the force experienced by a charged particle due to the gradient in intensity of an electromagnetic wave. For the ultra–short intense laser pulses used in laser wakefield acceleration this force is extremely large, and provides the main mechanism that couples the energy of the laser pulse to the plasma.

By considering the motion of an electron in the electric and magnetic fields of a laser we derive an expression for the ponderomotive force. The force on such an electron is the Lorentz force, and is given by,

$$\mathbf{F} = m\frac{d\mathbf{v}}{dt} = -e(\mathbf{E}(\mathbf{r}) + \mathbf{v} \times \mathbf{B}(\mathbf{r})) \tag{A.15}$$

where $\mathbf{E}$ is the electric field, $\mathbf{B}$ is the magnetic field and $\mathbf{v}$ is the particle's velocity. The electric field of the laser is a product of an envelope function, $\mathbf{E}_\xi$, and the fast oscillation at the laser frequency, ω:

$$\mathbf{E} = \mathbf{E}_\xi(\mathbf{r}) \cos(kx - \omega \mathrm{t}). \tag{A.16}$$

The motion of the electron can be considered in two parts. A slow motion phase, where the force due to the magnetic field can be neglected, as it requires an electron velocity, then a fast motion phase where the $\mathbf{v} \times \mathbf{B}$ term becomes important and the electric field is not constant across space. Taking the slow motion approximation, equation A.15 becomes:

$$m\frac{d\mathbf{v_1}}{dt} = -e\mathbf{E}(\mathbf{r_0}). \tag{A.17}$$

Further assuming that the laser pulse is monochromatic we can integrate equation A.17 yielding:

$$\mathbf{v_1} = -(e/m\omega)\mathbf{E}_\xi \sin(\omega t) \tag{A.18}$$

Integrating for a second time:

$$\delta\mathbf{r_1} = (e/m\omega^2)\mathbf{E}_\xi \cos(\omega t), \tag{A.19}$$

where δ signifies that this relation only holds for a small variation in $\mathbf{r_1}$. Considering the fast motion phase we have to take into account the spatial variation of the electric field around $\mathbf{r_1}$. Taking the second term in the Taylor expansion for $\mathbf{E}$ around $\mathbf{r_1}$:

$$\mathbf{E}(\mathbf{r}) = \mathbf{E}(\mathbf{r_0}) + (\delta\mathbf{r_1} \cdot \nabla)\mathbf{E}_{r=r_0} + \dots \tag{A.20}$$

Using equation A.16 with Maxwell's equation $-\partial\mathbf{B}/\partial\mathrm{t} = \nabla \times \mathbf{E}$ and integrating for $\mathbf{B}$ yields:

$$\mathbf{B}_1 = -(1/\omega)\nabla \times \mathbf{E}_{\xi_{\mathbf{r}=\mathbf{r_0}}} \sin(\omega\mathrm{t}). \tag{A.21}$$

Taking this equation with equation A.20 gives the second order approximation of our starting point, the Lorentz force experienced by the electron:

$$m\frac{d\mathbf{v_2}}{dt} = -e((\delta\mathbf{r_1} \cdot \nabla)\mathbf{E} + \mathbf{v_1} \times \mathbf{B_1}). \tag{A.22}$$

Substituting for $\mathbf{v_1}$ (equation A.18), $\delta\mathbf{r_1}$ (equation A.19) and $\mathbf{B_1}$ (equation A.21) gives the expression:

$$m\frac{d\mathbf{v_2}}{dt} = -\frac{e^2}{m\omega^2}(\cos^2(\omega t)(\mathbf{E}_\xi \cdot \nabla\mathbf{E}_\xi + \sin^2(\omega\mathrm{t})\mathbf{E}_\xi) \times (\nabla \times \mathbf{E}_\xi)). \tag{A.23}$$

Averaging over a laser cycle ($\cos^2(\omega t) = \sin^2(\omega t) = \frac{1}{2}$) and using the vector identity $\mathbf{A} \times (\nabla \times \mathbf{A}) = \frac{1}{2}\nabla \mathbf{A}^2 - (\mathbf{A} \cdot \nabla)\mathbf{A}$ gives us the non–linear force on an electron:

$$m\frac{d\mathbf{v_2}}{dt} = -\frac{1}{4}\frac{e^2}{m\omega^2}\nabla \mathbf{E}^2. \tag{A.24}$$

This is the ponderomotive force experienced by an electron:

$$F_P = -\frac{1}{4}\frac{e^2}{m\omega^2}\nabla \mathbf{E}^2. \tag{A.25}$$

Note the ponderomotive force is proportional to $\nabla \mathbf{E^2}$ which is proportional to $\nabla \mathbf{I}$ and is exceptional in that it is independent of the sign of the charged particle. That is to say that a charged particle will feel a force expelling it from the region of high intensity to a region of lower intensity, be it a plasma electron or ion.

A.2. Computational Techniques

A.2.1. EPOCH Bench Marking

In subsection 2.2.6 the ideal Gaussian beam length to efficiently drive a wakefield was derived. When simulating a Gaussian beam one has to truncate it in order to fit it into the simulation window. A hard cut to a Gaussian beam affects its wakefield driving capabilities. As such, for a true comparison between simulation code and theory predictions, the analytic model was adapted for a truncated Gaussian beam with the truncation at $\pm 3\ \sigma_z$. Changing the integration limits from $\pm\infty$ to $\pm 3\ \sigma_z$ in equation 2.37 yields,

$$\Delta n_{e(\xi)} = k_p n_{b_0} \int_{-3\sigma_z}^{3\sigma_z} \sin(k_p(\xi - \xi'))e^{\frac{-\xi^2}{2\sigma_x}} d\xi'. \tag{A.26}$$

Integrating equation A.26 gives the expressions for the variation of the electron number density perturbed by a relativistic truncated Gaussian proton beam:

$$\Delta n_{e(\xi)} = -\frac{i\sigma}{4}\sqrt{2\pi}e^{-\frac{1}{2}k^2\sigma^2-3ik\sigma-ikx}\left(e^{6ik\sigma}\mathrm{erf}\left(\frac{-\mathrm{z}+3\sigma+\mathrm{ik}\sigma^2}{\sqrt{2}\sigma}\right)+\mathrm{e}^{2\mathrm{ikz}}\mathrm{erf}\left(\frac{\mathrm{z}-3\sigma+\mathrm{ik}\sigma^2}{\sqrt{2}\sigma}\right)\right)$$
$$+\frac{i\sigma}{4}\sqrt{2\pi}e^{-\frac{1}{2}k^2\sigma^2-3ik\sigma-ikz}\left(e^{6ik\sigma}\mathrm{erf}\left(\frac{3}{\sqrt{2}}+\frac{\mathrm{i}\sigma\mathrm{k}}{\sqrt{2}}\right)+\mathrm{e}^{2\mathrm{ikz}}\mathrm{erf}\left(\frac{-3}{\sqrt{2}}+\frac{\mathrm{i}\sigma\mathrm{k}}{\sqrt{2}}\right)\right) \tag{A.27}$$

In essence the front and back hard edges of the truncated Gaussian drive a small amplitude wakefield that constructively or deconstructively interfere depending on the distance between truncations. If the distance is an integer multiple of the plasma wavelength then they interfere constructively, as a top hat density profile beam would.

When benchmarking EPOCH against theory in section 3.1.3, it is A.27 that it is compared to.

Bibliography

[1] S. Semushin and V. Malka, *High density gas jet nozzle design for laser target production*, Review of Scientific Instruments **72** (2001) no. 7, 2961–2965. http://scitation.aip.org/content/aip/journal/rsi/72/7/10.1063/1.1380393.

[2] *The Large Hadron Collider: Facts and Figures*, http://cds.cern.ch (2010) .

[3] M. S. Livingston, *The Livingston Plot*, http://tesla.desy.de (1954) .

[4] R. J. Goldston and P. H. Rutherford, *Introduction to Plasma Physics*. Springer, (1995).

[5] W. Leemans and E. Esarey, *Laser–driven plasma–wave electron accelerators*, Phys. Today **62** (2009) no. 3, 44–49.

[6] B. Hidding, T. Königstein, J. Osterholz, S. Karsch, O. Willi, and G. Pretzler, *Monoenergetic energy doubling in a hybrid laser–plasma wakefield accelerator*, Physical review letters **104** (2010) no. 19, 195002.

[7] Z. Najmudin, S. Kneip, M. Bloom, S. Mangles, O. Chekhlov, A. Dangor, A. Döpp, K. Ertel, S. Hawkes, J. Holloway, et al., *Compact laser accelerators for X-ray phase-contrast imaging*, Philosophical Transactions of the Royal Society of London A: Mathematical, Physical and Engineering Sciences **372** (2014) no. 2010, 20130032.

[8] T. Tajima and J. Dawson, *Laser electron accelerator*, Physical Review Letters **43** (1979) no. 4, 267.

[9] W. Leemans, B. Nagler, A. Gonsalves, C. Toth, K. Nakamura, C. Geddes, E. Esarey, C. Schroeder, and S. Hooker, *GeV Electron Beams from a Centimetre–Scale Accelerator*, Nature physics **2** (2006) no. 10, 696–699.

[10] I. Blumenfeld, C. E. Clayton, F.-J. Decker, M. J. Hogan, C. Huang, R. Ischebeck, R. Iverson, C. Joshi, T. Katsouleas, N. Kirby, et al., *Energy Doubling of 42 GeV Electrons in a Metre–Scale Plasma Wakefield Accelerator*, Nature **445** (2007) no. 7129, 741–744.

[11] F. Walsh, *Electron Acceleration from the Breaking of Relativistic Plasma Waves*, Nature **377** (1995) 19.

[12] D. Gordon, K. Tzeng, C. Clayton, A. Dangor, V. Malka, K. Marsh, A. Modena, W. Mori, P. Muggli, Z. Najmudin, et al., *Observation of Electron Energies Beyond the Linear Dephasing Limit from a Laser–Excited Relativistic Plasma Wave*, Physical review letters **80** (1998) no. 10, 2133.

[13] S. Mangles, C. Murphy, Z. Najmudin, A. Thomas, J. Collier, A. Dangor, E. Divall, P. Foster, J. Gallacher, C. Hooker, et al., *Monoenergetic Beams of Relativistic Electrons from Intense Laser–Plasma Interactions*, Nature **431** (2004) no. 7008, 535–538.

[14] P. Chen, J. Dawson, R. W. Huff, and T. Katsouleas, *Acceleration of Electrons by the Interaction of a Bunched Electron Beam with a Plasma*, Physical review letters **54** (1985) no. 7, 693.

[15] J. Rosenzweig, B. Breizman, T. Katsouleas, and J. Su, *Acceleration and Focusing of Electrons in Two–Dimensional Nonlinear Plasma Wake–Fields*, Physical Review A **44** (1991) no. 10, R6189.

[16] A. Pukhov and J. Meyer-ter Vehn, *Laser Wake Field Acceleration: The Highly Non-Linear Broken–Wave Regime*, Applied Physics B **74** (2002) no. 4-5, 355–361.

[17] A. Pukhov et al., *Proton–Driven Plasma–Wakefield Acceleration*, Nature Phys. **1** (2009) 363–367.

[18] E. Esarey, C. Schroeder, and W. Leemans, *Physics of Laser–Driven Plasma–Based Electron Accelerators*, Reviews of Modern Physics **81** (2009) no. 3, 1229.

[19] S. P. Mangles, A. G. Thomas, C. Bellei, A. Dangor, C. Kamperidis, S. Kneip, S. R. Nagel, L. Willingale, and Z. Najmudin, *Self–guided Wakefield Experiments Driver by Petawatt–Class Ultrashort Laser Pulses*, Plasma Science, IEEE

Transactions on **36** (2008) no. 4, 1715–1721.

[20] A. Abrami, F. Arfelli, R. Barroso, A. Bergamaschi, F. Bille, P. Bregant, F. Brizzi, K. Casarin, E. Castelli, V. Chenda, et al., *Medical Applications of Synchrotron Radiation at the SYRMEP Beamline of ELETTRA*, Nuclear Instruments and Methods in Physics Research Section A: Accelerators, Spectrometers, Detectors and Associated Equipment **548** (2005) no. 1, 221–227.

[21] J. C. Phillips, A. Wlodawer, M. M. Yevitz, and K. O. Hodgson, *Applications of Synchrotron Radiation to Protein Crystallography*, Proceedings of the National Academy of Sciences **73** (1976) no. 1, 128–132.

[22] C. Dougan et al., *Synchrotron Light*, Institute of Phys. (2011) .

[23] D. Attwood, *Soft X–Rays and Extreme Ultraviolet Radiation: Principles and Applications*. Cambridge university press, 1999.

[24] H. Kinoshita, T. Watanabe, M. Niibe, M. Ito, H. Oizumi, H. Yamanashi, K. Murakami, T. Oshino, Y. Y. Platonov, and N. Grupido, *Three–Aspherical Mirror System for EUV Lithography*, .

[25] *Graphic of an Undulator*, en.wikipedia.org/wiki/Undulator .

[26] A. Zholents and M. Zolotorev, *Femtosecond X–Ray Pulses of Synchrotron Radiation*, Physical review letters **76** (1996) no. 6, 912.

[27] Q. Gang, W. Jia-Fu, Y. Ming-Bao, C. Wei, C. Hong-Ya, and L. Yong-Feng, *Lowering Plasma Frequency by Enhancing the Effective Mass of Electrons: A Route to Deep Sub-Wavelength Metamaterials*, Chinese Physics B **22** (2013) no. 8, 087302.

[28] N. Gaur, *Effective Mass from Plasma Edge Reflection Measurements*, Physica **48** (1970) no. 1, 112–122.

[29] *Diamond Light Source Cryogenic Undulator*, danfysik.com .

[30] M. Hüning, *Status of the European XFEL*, Proc. of IPAC (2013) .

[31] *Diamond: Latest News*, `http://www.diamond.ac.uk` (2007) .

[32] R. Fedele, V. Vaccaro, and G. Miano, *The Plasma Undulator*, Physica Scripta Volume T **30** (1990) 192–197.

[33] S. Kneip, C. McGuffey, J. Martins, S. Martins, C. Bellei, V. Chvykov, F. Dollar, R. Fonseca, C. Huntington, G. Kalintchenko, et al., *Bright Spatially Coherent Synchrotron X–Rays from a Table–Top Source*, Nature Physics **6** (2010) no. 12, 980–983.

[34] A. Rousse, K. T. Phuoc, R. Shah, A. Pukhov, E. Lefebvre, V. Malka, S. Kiselev, F. Burgy, J.-P. Rousseau, D. Umstadter, et al., *Production of a keV X–Ray Beam from Synchrotron Radiation in Relativistic Laser–Plasma Interaction*, Physical review letters **93** (2004) no. 13, 135005.

[35] A. Rousse, K. T. Phuoc, R. Shah, R. Fitour, and F. Albert, *Scaling of Betatron X–ray Radiation*, The European Physical Journal D **45** (2007) no. 2, 391–398.

[36] S. Kneip, S. Nagel, C. Bellei, N. Bourgeois, A. Dangor, A. Gopal, R. Heathcote, S. Mangles, J. Marques, A. Maksimchuk, et al., *Observation of Synchrotron Radiation from Electrons Accelerated in a Petawatt–Laser–Generated Plasma Cavity*, Physical review letters **100** (2008) no. 10, 105006.

[37] A. Thomas and K. Krushelnick, *Betatron X–Ray Generation from Electrons Accelerated in a Plasma Cavity in the Presence of Laser Fields*, Physics of Plasmas (1994-present) **16** (2009) no. 10, 103103.

[38] S. Cipiccia, M. R. Islam, B. Ersfeld, R. P. Shanks, E. Brunetti, G. Vieux, X. Yang, R. C. Issac, S. M. Wiggins, G. H. Welsh, et al., *Gamma–Rays from Harmonically Resonant Betatron Oscillations in a Plasma Wake*, Nature Physics **7** (2011) no. 11, 867–871.

[39] F. F. Chen and M. D. Smith, *Introduction to Plasma Physics and Controlled Fusion*, vol. 1. Wiley Online Library, 1984.

[40] C. B. Schroeder, *Plasma Wake Excitation by Lasers or Particle Beams*, Lawrence Berkeley National Laboratory (2011) .

[41] W. Rittershofer, C. Schroeder, E. Esarey, F. Grüner, and W. Leemans, *Tapered Plasma Channels to Phase–Lock Accelerating and Focusing Forces in Laser–Plasma Accelerators*, Physics of Plasmas (1994-present) **17** (2010) no. 6, 063104.

[42] M. Rosenbluth and C. Liu, *Excitation of Plasma Waves by Two Laser Beams*, Physical Review Letters **29** (1972) no. 11, 701.

[43] W. Leemans, C. Clayton, W. Mori, K. Marsh, P. Kaw, A. Dyson, C. Joshi, and J. Wallace, *Experiment and Simulations of Tunnel–ionised Plasmas*, Physical Review A **46** (1992) no. 2, 1091.

[44] R. Kulyagin and V. Taranukhin, *Tunneling Ionization of Atoms and Ions in a Strong Laser Field and the Effect of Local Ionization Suppression*, Laser Phys **3** (1993) 644–650.

[45] S. Augst, D. D. Meyerhofer, D. Strickland, and S.-L. Chin, *Laser Ionization of Noble Gases by Coulomb–Barrier Suppression*, JOSA B **8** (1991) no. 4, 858–867.

[46] J. Bardsley, A. Szoke, and M. Comella, *Multiphoton Ionisation from a Short–Range Potential by Short–Pulse Lasers*, Journal of Physics B: Atomic, Molecular and Optical Physics **21** (1988) no. 23, 3899.

[47] N. A. Hart, J. Strohaber, G. Kaya, N. Kaya, A. A. Kolomenskii, and H. A. Schuessler, *Intensity–Resolved Above Threshold Ionization of Xenon with Short Laser Pulses*, Physical Review A **89** (2014) no. 5, 053414.

[48] P. Sprangle, E. Esarey, and A. Ting, *Nonlinear Theory of Intense Laser Plasma Interactions*, Physical review letters **64** (1990) no. 17, 2011.

[49] N. Kumar, A. Pukhov, and K. Lotov, *Self–Modulation Instability of a Long Proton Bunch in Plasmas*, Physical review letters **104** (2010) no. 25, 255003.

[50] A. Pukhov, N. Kumar, T. Tückmantel, A. Upadhyay, K. Lotov, P. Muggli, V. Khudik, C. Siemon, and G. Shvets, *Phase Velocity and Particle Injection in a Self–Modulated Proton–Driven Plasma Wakefield Accelerator*, Physical review letters **107** (2011) no. 14, 145003.

[51] C. E. Max, J. Arons, and A. B. Langdon, *Self–Modulation and Self–Focusing of Electromagnetic Waves in Plasmas*, Physical Review Letters **33** (1974) no. 4, 209.

[52] E. Esarey, J. Krall, and P. Sprangle, *Envelope Analysis of Intense Laser Pulse Self–Modulation in Plasmas*, Physical review letters **72** (1994) no. 18, 2887.

[53] S. Le Blanc, M. Downer, R. Wagner, S.-Y. Chen, A. Maksimchuk, G. Mourou, and D. Umstadter, *Temporal Characterization of a Self–Modulated Laser Wakefield*, Physical review letters **77** (1996) no. 27, 5381.

[54] S. Wang, C. Clayton, B. Blue, E. Dodd, K. Marsh, W. Mori, C. Joshi, S. Lee, P. Muggli, T. Katsouleas, et al., *X–Ray Emission from Betatron Motion in a Plasma Wiggler*, Physical review letters **88** (2002) no. 13, 135004.

[55] P. Schmüser, M. Dohlus, J. Rossbach, and C. Behrens, *Free–Electron Lasers in the Ultraviolet and X–Ray Regime*, vol. 1. Springer, 2014.

[56] J. D. Jackson and R. F. Fox, *Classical Electrodynamics*, vol. 67. American Association of Physics Teachers, 1999.

[57] A. G. R. Thomas, *Algorithm for Calculating Spectral Intensity due to Charged Particles in Arbitrary Motion*, Phys. Rev. ST Accel. Beams **13** (2010) 020702.

[58] Q. Shen, *X–ray Flux, Brilliance and Coherence of the Proposed Cornell Energy–Recovery Synchrotron Source*, CHESS Technical Memo **01** (2001) .

[59] C. K. Birdsall and A. B. Langdon, *Plasma Physics Via Computer Simulation.* CRC Press, 2004.

[60] J. Dawson and A. Lin, *Particle Simulation: Handbook of Plasma Physics*, vol. 2. Elsevier Science Publishers, 1984.

[61] H. Ruhl, *Classical Particle Simulations*, Introduction to Computational Methods in Many Body Physics **100** (2006) 19–120.

[62] R. F. Bird, S. J. Pennycook, S. A. Wright, and S. A. Jarvis, *Towards a Portable and Future–proof Particle–in–Cell Plasma Physics Code*, .

[63] R. Courant, K. Friedrichs, and H. Lewy, *Uber die Partiellen Differenzengleichungen der Mathematischen Physik*, Mathematische Annalen **100** (1928) no. 1, 32–74.

[64] A. G. R. Thomas, *RDTX Users Manual*, http://www.rdtx.alecthomas.com/ (2013) .

[65] A. Thomas, *Algorithm for Calculating Spectral Intensity due to Charged Particles in Arbitrary Motion*, Physical Review Special Topics-Accelerators and Beams **13** (2010) no. 2, 020702.

[66] M. Streeter, *Ultrafast Dynamics of Relativistic Laser Plasma Interactions*, .

[67] H. T. Kim, K. H. Pae, H. J. Cha, I. J. Kim, T. J. Yu, J. H. Sung, S. K. Lee,

T. M. Jeong, and J. Lee, *Enhancement of Electron Energy to the Multi–GeV Regime by a Dual–Stage Laser–Wakefield Accelerator Pumped by Petawatt Laser Pulses*, Physical review letters **111** (2013) no. 16, 165002.

[68] A. Collaboration, *AWAKE Design Report: A Proton–Driven Plasma Wakefield Acceleration Experiment at CERN*, Plasma Physics and Controlled Fusion **56** (2014) no. 8, 084013.

[69] G. Xia, L. Silva, W. Mori, P. Muggli, W. Lu, A. Caldwell, N. Lopes, W. An, K. Lotov, J. Vieira, et al., *A Proposed Experimental Test of Proton–Driven Plasma Wakefield Acceleration Based on CERN SPS*, .

[70] *The AVET Ti:S Femtosecond TW System*, `http://www.avesta.ru/` .

[71] E. Esarey, B. Shadwick, P. Catravas, and W. Leemans, *Synchrotron Radiation from Electron Beams in Plasma–Focusing Channels*, Physical Review E **65** (2002) no. 5, 056505.

[72] S. Kneip, C. McGuffey, F. Dollar, M. Bloom, V. Chvykov, G. Kalintchenko, K. Krushelnick, A. Maksimchuk, S. Mangles, T. Matsuoka, et al., *X–ray Phase contrast Imaging of Biological Specimens with Femtosecond Pulses of Betatron Radiation from a Compact Laser Plasma Wakefield Accelerator*, Applied Physics Letters **99** (2011) no. 9, 093701.

[73] R. Dorn, S. Quabis, and G. Leuchs, *Sharper Focus for a Radially Polarized Light Beam*, Physical review letters **91** (2003) no. 23, 233901.

[74] A. Langley, E. Divall, C. Hooker, M. Hutchinson, A. Lecot, D. Marshall, M. Payne, and P. Taday, *The Development of a Multi–Terawatt Femtosecond Laser Facility — Astra*, Rutherford Appleton Laboratory Central Laser Facility Annual Report 1999/2000pp **196** (2000) .

[75] C. B. Schaffer, A. Brodeur, and E. Mazur, *Laser–Induced Breakdown and Damage in Bulk Transparent Materials Induced by Tightly Focused Femtosecond Laser Pulses*, Measurement Science and Technology **12** (2001) no. 11, 1784.

[76] D. Strickland and G. Mourou, *Compression of Amplified Chirped Optical Pulses*, Optics communications **55** (1985) no. 6, 447–449.

[77] T. Z. Esirkepov.

[78] J. Cole, *Simulations of the lengthened Astra beam*, Private Communications (2015) .

[79] K. L. Sala, G. Kenney-Wallace, G. E. Hall, et al., *CW Autocorrelation Measurements of Picosecond Laser Pulses*, Quantum Electronics, IEEE Journal of **16** (1980) no. 9, 990–996.

[80] D. J. Kane and R. Trebino, *Single–Shot Measurement of the Intensity and Phase of an Arbitrary Ultrashort Pulse by Using Frequency–Resolved Optical Gating*, Optics letters **18** (1993) no. 10, 823–825.

[81] P. . M. Paul, E. Toma, P. Breger, G. Mullot, F. Augé, P. Balcou, H. Muller, and P. Agostini, *Observation of a Train of Attosecond Pulses from High Harmonic Generation*, Science **292** (2001) no. 5522, 1689–1692.

[82] R. Jung, J. Osterholz, O. Willi, M. Galimberti, L. Gizzi, M. Borghesi, S. Kar, C. Cecchetti, R. Heathcote, and D. Neely, *Optimization and Characterization of Supersonic Gas Jet Target for Laser–Plasma Interaction Studies*, Central Line Facility Annual Report (2004) 23–24.

[83] S. Kneip, S. Nagel, S. Martins, S. Mangles, C. Bellei, O. Chekhlov, R. Clarke, N. Delerue, E. Divall, G. Doucas, et al., *Near–GeV Acceleration of Electrons by a Nonlinear Plasma Wave Driven by a Self–Guided Laser Pulse*, Physical review letters **103** (2009) no. 3, 035002.

[84] *Series 9 solenoid fast pulse Parker valve*, `http://www.sensortechnics.com` .

[85] J. Faure, Y. Glinec, A. Pukhov, S. Kiselev, S. Gordienko, E. Lefebvre, J.-P. Rousseau, F. Burgy, and V. Malka, *A Laser–Plasma Accelerator Producing Monoenergetic Electron Beams*, Nature **431** (2004) no. 7008, 541–544.

[86] A. G. Glendinning, S. G. Hunt, and D. E. Bonnett, *Recording Accelerator Monitor Units During Electronic Portal Imaging: Application to Collimator Position Verification During IMRT*, Physics in Medicine and Biology **46** (2001) no. 6, N159. `http://stacks.iop.org/0031-9155/46/i=6/a=404`.

[87] M. Kasim, *Simulations of the lengthened Astra beam*, Private Communications (2015) .